STUDIES OF MECHANICAL BEHAVIOR OF HFPE-II-52 POLYIMIDE IN EXTREME ENVIRONMENTS

A Dissertation

Presented to the Faculty of the Graduate School

of Cornell University

in Partial Fulfillment of the Requirements for the Degree of

Doctor of Philosophy

by

Yi Xu

August 2017

STUDIES OF MECHANICAL BEHAVIOR OF HFPE-II-52 POLYIMIDE IN EXTREME ENVIRONMENTS

Yi Xu, Ph. D.

Cornell University 2017

Motivated by demanding applications of polyimides and polyimide matrix composites, this study aims to understand the mechanical behavior of HFPE-II-52 polyimide at high temperature. First, a temperature dependent constitutive model combining linear viscoelasticity with viscoplasticity was developed. The viscoplastic part of the model uses a power law flow potential with state variable evolution. The full model was fit to a set of tension tests including constant strain rate, multistep stress relaxation, and creep and recovery tests in a range of temperature 285-315ºC. Second, the effects of moisture on the mechanical properties of polyimide were investigated. Separate experiments were designed to study the effects of both hydrolytic degradation and plasticization. The experiments consist of exposing the material sample to high temperature, moisture saturated conditions over a range of times and temperatures. Following moisture exposure, compression tests were performed to measure the reductions of stiffness and yield stress. A temperature and moisture dependent kinetic model was then developed and was integrated with the previous viscoelastic and viscoplastic model. Third, under certain hygrothermal conditions such as rapid heating with moisture saturated polyimide, the material may fail by high pressure water vapor induced blistering. Built on prior modeling efforts, a finite element approach is used to simulate the material unstable void growth. The simulation approach provides a means for the prediction of the critical temperature of blistering under different heating rates and moisture levels

and allows for an investigation of the importance of the effects of pressure, thermal softening, hydrolytic degradation and plasticization on the blistering failure of polyimide.

BIOGRAPHICAL SKETCH

Yi Xu was born on November 13, 1989 in Beijing, China. In 2008, he was admitted to Tsinghua University to pursue the major of Engineering Mechanics and Aerospace Engineering in Beijing. After receiving the Bachelor degree in 2012, he moved to U.S. and began his Ph.D. study in the Department of Mechanical and Aerospace Engineering at Cornell University. His major field is Theoretical and Applied Mechanics, with a minor of Computational Science and Engineering.

To my parents.

ACKNOWLEDGMENTS

This work would not have been possible without the help of many people.

First and foremost, I would like to thank Professor Alan Zehnder. I consider myself very lucky to have him as my PhD advisor over the last five years. It has been a great learning experience for me with his insights into solid mechanics, mathematical modeling, and general methodology for experimental design. I appreciate that he gave me freedom on exploring new possibilities on my research, but was always available to provide me insightful guidance and suggestions on those ideas. With the help of him, I started to learn how to study new things and how to conduct research.

I would also like to thank Professor Meredith Silberstein and Professor Derek Warner for serving as my special committee members, and for providing some valuable suggestions to this work. Thanks also go to Professor Claude Cohen and Professor Herbert Hui for some inspiring discussions.

Finally, I want to thank my family for standing behind me all the time. Thank you to my parents for their continuous encouragement and support. Thanks also to my wife Ailu for being with me through all the up's and down's during my PhD journey.

TABLE OF CONTENTS

LIST OF TABLES

LIST OF FIGURES

CHAPTER 1

INTRODUCTION

Polyimides are a special class of polymers that have versatile applications ranging from membrane films used in gas separation to matrices for fiber-reinforced laminates used in aerospace engineering [1]–[4]. They extend the use of polymers to high temperature applications due to their high T_g (above 300ºC). With respect to their microstructures, polyimides can be divided into thermoplastic and thermoset polyimides. DuPont Kapton film, for instance, is a widely used thermoplastic polyimide that has applications in electronic packaging, wire insulation, membrane separation and flex circuits [5]. Thermoset polyimides, however, because of their addition-curing process to form additional cross-linked bonds, have higher stiffness and strength and enhanced heat and chemical resistance. They are particularly attractive for use in severe environments, such as reusable launching vehicles, components of aero-engines, and gas turbine blades, usually in the form of matrix for fiber-reinforced composites [2], [6], [7]. PMR-15, PMR-II and AFR700B are a few examples of thermoset polyimides that are widely studied [8]–[13]. In this dissertation, I focus on polyimides HFPE-II-52 that were developed in NASA Glenn Research Center in early 2000s [14], but the methodologies and most of the qualitative conclusions are applicable for other thermoset polyimides.

Given their wide range of applications, polyimides and polyimide matrix composites (PiMCs) are frequently subject to complex mechanical and thermal loadings. Thus, a constitutive model is required to predict the material deformation and failure under various conditions. Although many studies have been conducted recently on polyimides and their composites [3], [15], [16], the constitutive modeling of their mechanical performance, especially at high temperature, is challenging. One reason is that the mechanical behavior of polyimide is strongly time dependent,

with different mechanical responses under different types of loading, i.e. creep and recovery, stress relaxation, or constant strain rate tests. In addition, polyimides, due to the nature of polymers, experience strong thermal softening, which makes it difficult for the model to work over a wide range of temperatures. Some prior studies on modeling thermosetting polyimides at high temperature are limited to a single type of loading condition and/or focused on their behaviors at low stress levels before significant material strain softening occurs [17]–[20]. Other modeling approaches are temperature independent, which work only at one or some specific temperatures [18], [21], [22]. The current work in *Chapter 2* extends these studies by modeling the mechanical performance of HFPE-II-52 polyimides over a range of temperatures up to 315°C. To capture the mechanical response for different stress levels, the efforts of modeling are separated into linear viscoelasticity and state variable viscoplasticity. The model parameters are identified with a wide type of loading conditions including creep recovery at different stress levels, multistep stress relaxation, and constant strain rate tension until failure. As an example application, the model is used in the context of PiMCs with unit cell modeling approach to determine the shear strength of the fiber reinforced composites. *Chapter 2* is a modeling framework of this dissertation, which will be extended with moisture dependence investigated in *Chapter 3*. The main text of *Chapter 2* is based on the published work "Time and temperature dependent mechanical behavior of HFPE-II-52 polyimide at high temperature" in the journal *Mechanics of Materials* [23].

Besides strong thermal softening, polyimides also exhibit moisture degradation when operated in wet (high relative humidity) environments [24]–[30]. To fully explore the use of polyimides and PiMC in extreme environments, it is essential to quantify the effects of moisture on the mechanical performance of polyimides, which is the topic investigated in *Chapter 3*. Those moisture effects are strongly coupled with temperature. At room temperature, no material property reductions are

observed with polyimide fully saturated with water [31]. At elevated temperature starting from 100ºC, water absorbed by the material can act as a plasticizer to cause instantaneous but reversible reductions of material T_g, stiffness and yield strength. In addition, severe permanent damage could occur with hydrolytic degradation at temperatures above 200ºC. The rate of bond breaking caused by hydrolysis is strongly temperature dependent and significant degradation is observed within minutes of moisture exposure at a temperature of 250ºC. Considering that different mechanisms of moisture degradation exist, separate experiments must be designed. For nonreversible, history dependent hydrolytic degradation, the polyimide samples are first exposed to saturated steam environment in a pressure tube over a range of temperatures and durations. Then the samples are dried and mechanically tested under compression. While for reversible, instantaneous plasticization, the mechanical test is required to be performed while moisture is maintained in the material. Once the mechanical degradation of hydrolysis and plasticization is quantified as a function of temperature and moisture level, a temperature and moisture dependent kinetic model is developed and fit to the experimental data. The main text of *Chapter 3* is based on the published work "Moisture degradation effects on the mechanical properties of HFPE-II-52 polyimide: experiments and modeling" in the journal *Experimental Mechanics* [32].

Under certain hygrothermal conditions such as rapid heating with moisture saturated polyimide, the moisture would create enough vapor pressure to explode the material from within, even without external loadings [33]–[36]. The difficulty of predicting such blistering failure is one of the issues for polyimide and PiMC to be used in extreme (hot-wet) environments. *Chapter 4* first summarizes the time, temperature and moisture dependent constitutive model that combines the studies in *Chapter 2* and *3*. Then a finite element model is built to predict the critical heating rate and moisture level for polyimide to have unstable steam pressure induced void growth. The work is

based on paper “Pressure, hydrolytic degradation and plasticization drive high temperature blistering failure in wet polyimides” that is under review in the journal *Extreme Mechanics Letters* [37].

Overall, this study aims to have a better understanding of the time, temperature and moisture dependent mechanical performance of thermoset polyimides, and to improve the prediction capabilities of the mechanical response of the material under different conditions, thus to make full use of them in extreme environments. Conclusions and the main contributions are presented at the end of each separate chapters. Appendices are included to cover the details of the studies.

CHAPTER 2

HIGH TEMPERATURE CONSTITUTIVE MODELING

2.1 Introduction

Polyimides are used in a broad range of demanding applications due to their exceptional thermal, chemical and mechanical properties. Thermosetting polyimides are of particular interest for high temperature use due to their high glass transition temperatures (T_g), up to or beyond 350ºC [14], [38], [39]. Polyimides have been in mass production since 1955, when DuPont introduced Kapton, a polyimide film that has been used for flex circuits, electronic packaging and wire insulation in many environmentally harsh systems and over a broad range of temperatures [5]. Since then significant research has been directed to the synthesis of high temperature polymers, resulting in the successful development of other addition-curing polyimides such as PMR-15, HFPE-50, AFR-PE-4 and others [13], [40], [41]. These polyimides were developed for use as adhesives and matrices in fiber reinforced composites intended for lightweight, high temperature structures. Current and potential applications include components of aero-engines [2], reusable launch vehicles [6] and advanced steam turbine blades [7]. To design such systems and to be able to predict their mechanical performance under severe loadings and environmental conditions, an approach to developing high temperature constitutive models that can be implemented in a finite element (FE) code is needed. We focus here on the polyimide HFPE-II-52 [14], however our approaches to testing and modeling can be directly applied to similar polyimides and other polymers used at high temperatures.

A number of approaches to constitutive modeling of polyimides at high temperature could be used. The simplest model would be linear viscoelasticity which will capture the time and

temperature dependent mechanical response at low stresses [31]. As the stress and/or strain levels increase, nonlinear effects such as stress or strain dependent creep rates, and permanent (plastic) deformations will become important and cannot be ignored. To model such effects nonlinear viscoelasticity and/or viscoplasticity must be considered. One of the best known approaches to nonlinear viscoelasticity is Schapery's model [42]. It has the same integral representation as linear viscoelasticity, with additional parameters allowing the modulus to depend on stress/strain and the loading rate. The material parameters can be determined from standard creep or relaxation tests and an empirical approach of time-temperature and time-stress superposition can be used to reduce the parameter sets [43]. The model has enjoyed a great success and has been applied to model polyimides at elevated temperatures at stress levels below yield [44]. A number of approaches to nonlinear viscoelastic models in the context of finite deformation are reviewed by Wineman [45] and Drapaca et al. [46]. Karra and Rajagopal [20] use a finite deformation nonlinear viscoelastic approach to model high temperature creep of HFPE-II-52 and PMR-15 polyimides at stress levels for which the deformation remains reversible. However, nonlinear viscoelasticity is not able to represent the material's permanent deformation or mechanical behavior near the failure point, thus other approaches are needed to model behavior at high stresses.

Viscoplasticity has been suggested as a means for modeling the mechanical behavior of polymers over a broad stress and temperature range [47]. Many viscoplastic constitutive equations have been developed over the years [47]–[53]. Some were developed for metals then adapted to polymers including polyimides. For example, McClung and Ruggles-Wrenn [54] modeled the rate dependent behavior of PMR-15 using an over-stress viscoplasticity model initially developed for metals. Other models were developed specifically for polymers. Bhargava [22], for example, investigated the viscoplastic behavior of HFPE-II-52 polyimide at high temperature using

Schapery's nonlinear viscoelasticity model plus a state variable viscoplasticity based on a model by Boyce et al. [47]. This constitutive model has a single state variable that indicates the deformation resistance, and that evolves with plastic strain. While this model can capture the material behavior of polyimide at high temperatures it requires a large set of material parameters. Furthermore, the parameter sets are different for each temperature and are not monotonic with temperature, thus no means other than interpolation was available to mathematically represent the temperature dependence of the model in non-isothermal applications.

Prior experimental/modeling studies of the high temperature deformation of polyimides [20], [44], [54] consider a single type of loading, for example creep/recovery or monotonic tension loading. The current work extends these approaches by exploring the material response under stress controlled (creep/recovery), strain controlled (step relaxation) and constant strain rate conditions, all over a wide range of stresses up to the ultimate tensile strength (UTS) of the material and over a temperature range of 285ºC to 315ºC at which the material starts to exhibit significant thermal softening. Time dependent response is observed at low and high stress levels. At low stresses the deformation is observed to be reversible while permanent deformation is observed at stress levels above about 30% of the UTS.

These above observations led us to combining viscoelasticity and state variable viscoplasticity in the constitutive model. To keep the model as simple as possible the viscoelastic model is taken to be linear, although a nonlinear model also can be used, at the expense of additional complexity in parameter identification and implementation. Strain is decomposed into viscoelastic and viscoplastic parts to capture both the reversible and permanent deformation behavior from low stresses up to failure. The linear viscoelastic model uses a Prony series representation of relaxation modulus, with time temperature superposition (TTS) following the Williams-Landel-Ferry (WLF)

equation. The nonlinear effects are modeled by a small strain, power law viscoplastic model with two evolving state variables to capture both strain softening and hardening. Material parameters for the HFPE-II-52 polyimide resin are identified based on the full spectrum of experimental results. The model was then numerically incorporated as a user material into the commercial finite element (FE) code ABAQUS. Finally, as a demonstration of the model's practical applications, two FE simulations were performed. One simulation is a plane stress model of a high temperature, constant displacement rate monotonic tension test. The other is a 3D unit cell model of a polyimide matrix unidirectional carbon fiber reinforced composite under high temperature shear loading.

2.2 Experimental Observations

A common approach to high temperature material characterization is to focus on a specific type of loading, i.e. creep, or relaxation for calibration of constitutive models. However, to develop a model that will apply across a range of loading types, the material should be tested under both stress and strain controlled conditions. In this chapter, we summarize the experimental methods and observations of mechanical testing of HFPE-II-52 polyimide resin under three conditions: monotonic tension at a fixed strain rate, creep-recovery at a range of stress levels and multi-step relaxation in which strain is increased in steps, but held for a fixed period between steps. The experiments were performed by Bhargava [22] and the results are used in this chapter to develop a high temperature constitutive model of HFPE-II-52 polyimide.

2.2.1 Sample preparation and experimental setup

Tension test samples were prepared from 4 mm thick, 100 × 100 mm plates fabricated by compression molding at 172 atm pressure and 377°C for 2 hours followed by post-curing at 371°

C for 16 hours. For details on the sample fabrication see references [14], [22]. The HFPE-II-52 polyimide we used for testing has a T_g of 350°C, determined through a thermomechanical analyzer. The storage and loss modulus of the material at room temperature are 3.9 GPa and 0.14 GPa, respectively [31]. The density of the material is 0.00142 g/mm^3 [34]. The tension samples were cut to the dimensions shown in Figure 2.1 and polished using 600 grit paper to remove any rough edges and scratches from the surface. Prior to testing all samples were dried in a vacuum oven for 3 days at 70°C.

All tension tests were performed using an MTS 45 kN servo-hydraulic testing system with water cooled, hydraulically actuated wedge grips. The system can be operated under either strain or load control. The experimental setup consists of a clamshell furnace, high temperature extensometer and thermocouples for feedback control of the sample temperature. A small, clamshell furnace, ATS 3210, is used to heat the sample. The furnace mounts to the MTS and can be opened for specimen loading then closed to completely surround the sample. A small slot in the clamshell opening allows the ceramic arms of the high temperature extensometer, MTS 632.54, to reach into the furnace and rest against the sample. The chisel edged ceramic arms are held against the sample with a spring force of approximately 1 N. Ceramic fiber insulation packed around the openings at the top and bottom of the furnace help greatly to maintain a uniform temperature. To provide accurate temperature control, a 36 gauge, K-type thermocouple is embedded into a dummy sample of HFPE-II-52 that is placed in the furnace alongside the test article. This thermocouple was used as feedback for the furnace controller allowing the temperature to be held constant within ±1.5°C. Each test was started at room temperature under force control with the load set at zero. The furnace was ramped to the test temperature and held for 1 hour prior to testing to ensure thermal equilibrium.

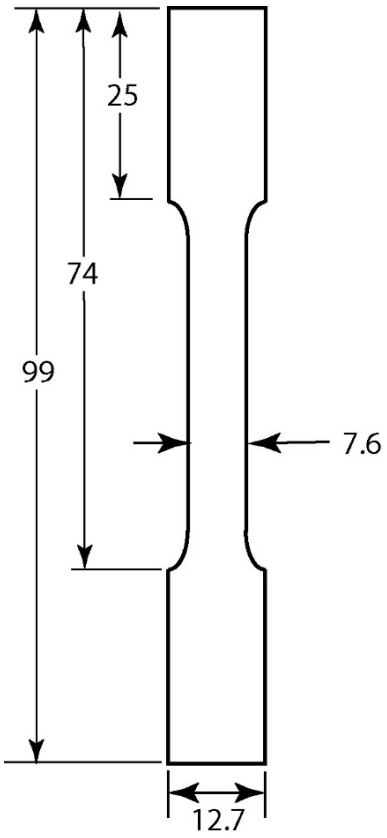

Figure 2.1: Tension test dogbone sample geometry. All dimensions in mm. Sample is 3 mm thick.

2.2.2 Tension test procedures

To provide baseline data on the strength of HFPE-II-52 under tension at a range of temperatures, the first tests were performed under monotonic, constant displacement rate loading. Prior to loading a 50 to 100 N cyclic load was applied to the sample and the relation between measured cross head displacement and strain measured by the extensometer was recorded. To prevent damage of the extensometer during the tension loading, the extensometer was then removed and the test conducted under displacement control. The applied displacement was converted to strain using the measured calibration of displacement to strain. All samples were loaded at a strain rate of approximately 10^{-3}/s.

The creep-recovery tests were performed at stress levels from 0.1 to 0.6 of the ultimate tensile stress (UTS) observed in the fixed strain rate tension test at a particular temperature. In these tests the load was ramped over 10 seconds from zero to the target level. Using the measured strain and accounting for thermal strain and assuming plastic incompressibility, the load was adjusted in a feedback loop during the creep test to maintain an approximately constant true stress. Note that as the strain levels are very small, around 5%, the difference between the nominal and true stress is small. Once the target load was reached, each sample was held at this stress for 4 hours and then allowed to recover for 4 hours at zero load. In some of the tests performed at higher stress levels the strain became unstable and the test was either stopped manually or the samples failed rapidly, typically breaking the ceramic extensometer arms in the process.

Multi-step relaxation tests were performed to provide additional data for model development. These tests were performed under displacement control. Between each step the displacement was ramped at a strain rate of approximately 10^{-3}/s. The strain levels for each step varied, but were generally in the range of 0.5% per step up to a strain of 5 to 10%, depending on the temperature. Once the target strain was reached, the displacement was held constant for 2 hours at each step during which load relaxation was recorded.

2.2.3 Experimental results

The nominal mechanical strains (computed through a temperature specific calibration of strain to cross head displacement) and the nominal stresses (force/initial area) are plotted in Figure 2.2 for temperatures 285, 300 and 315^{o}C. It is observed that the loads drop after reaching the UTS at all temperatures. Both the material initial stiffness and the UTS decrease as the temperature increases, while the strain to failure increases with temperature.

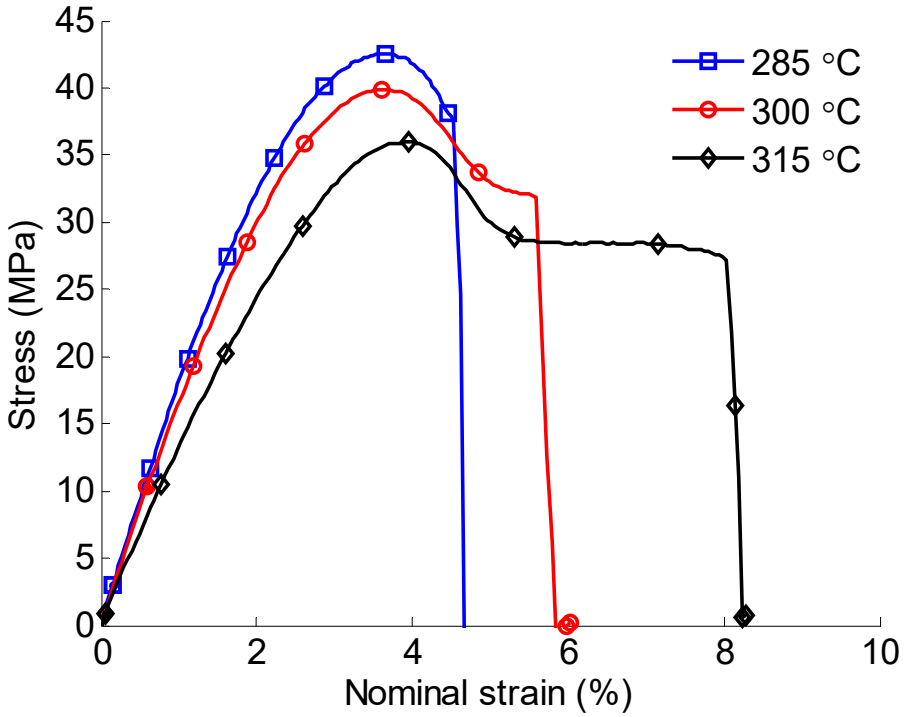

Figure 2.2: Experimental results for fixed strain rate (10^{-3}/s) tension tests at different temperatures. The markers in the plots identify the curves; they do not signify individual data points. Note that (for this data only) strains are inferred from the strain-displacement calibration and hence should be considered as nominal values.

An example result at 315°C is shown in Figure 2.3. It can be observed that at the lowest stress level the creep strain almost fully recovers after the load is removed. As the stress level increases, the material has permanent deformation after unloading indicating that plastic deformation is starting to occur. At a stress of 0.55 UTS, the creep strain grows unstably until the sample fails. It is clear that the polyimide samples have both viscoelastic and viscoplastic deformations, depending on the stress levels. Data for the 285 and 300°C tests are shown in Figures 2.6 - 2.7. Note that creep data from the test at the lowest stress level for each temperature were used to

determine the parameters of the linear viscoelastic part of the constitutive model.

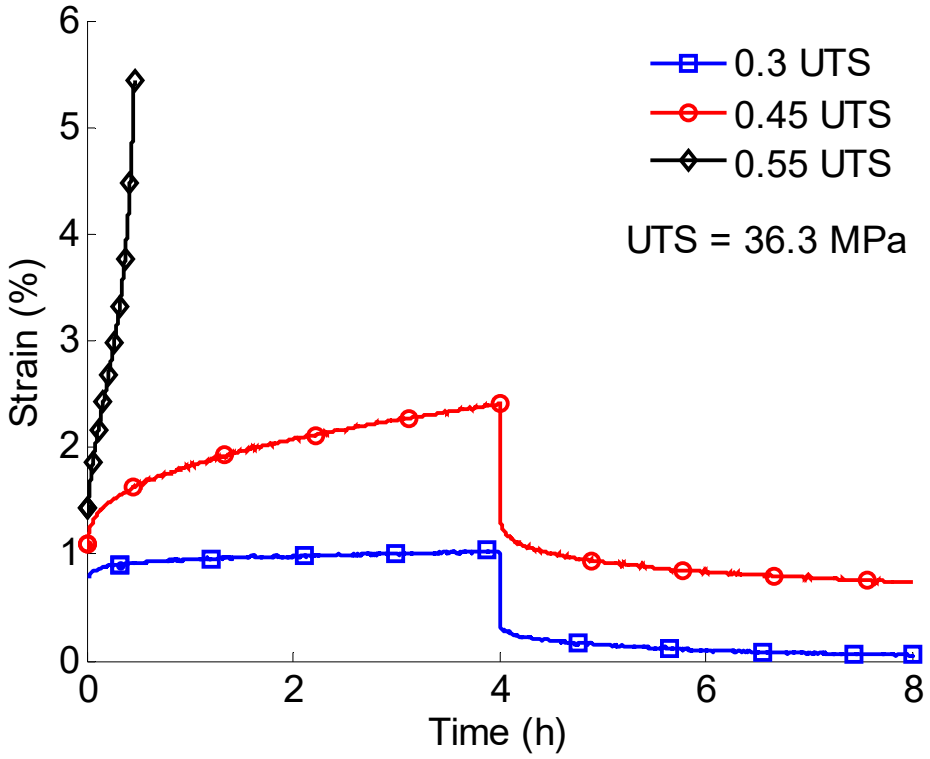

Figure 2.3: Sample experimental data: creep recovery at 315ºC at three stress levels. Stress levels are relative to the UTS measured in fixed strain rate tests.

An example result at 315ºC is shown in Figure 2.4. Data for the 285 and 300ºC tests are shown in Figures 2.9 - 2.10. Under the test conditions, the material shows pronounced softening at strains above about 3%. Note that the test is performed in displacement, not strain control. The strain is seen to increase slightly during the test indicating that some localization of strain occurs in the gauge section of the extensometer even while overall extension is held constant.

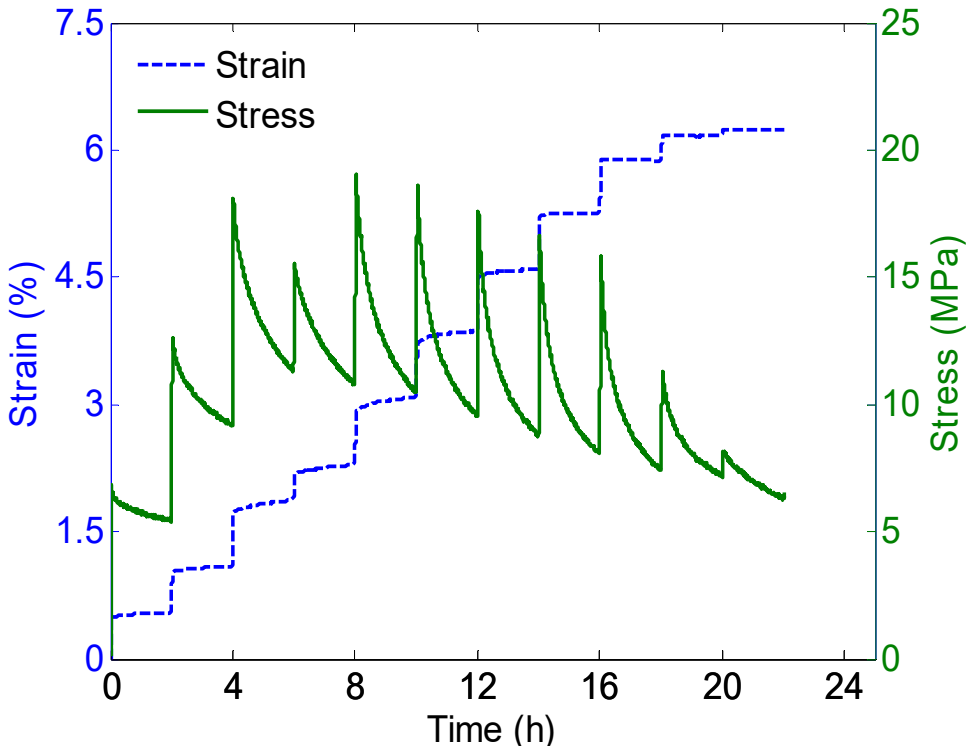

Figure 2.4: Sample experimental data: multi-step relaxation at 315°C

2.3 Constitutive Model Development

2.3.1 Modeling approach overview

The constitutive equations developed here model the time and temperature dependent mechanical response of polyimide at high temperature. The model may not be valid above 315°C, where the material behavior begins to change significantly as the T_g of 350°C is approached. We characterize the viscoelastic and viscoplastic behaviors separately, first using data from low stresses for viscoelastic model parameter identification and then performing the fitting for the viscoplastic model. The model is applicable for different types of loading conditions since the experimental data used to fit the model parameters incorporates monotonic constant strain rate tension tests, creep recovery tests and multistep stress relaxation tests. Non-isothermal loading can easily be

modeled without parameter interpolation, since the model depends on temperature explicitly and all material parameters are temperature independent. The model is designed to capture the short term and long term time and temperature dependent stiffness, temperature dependent ultimate stress and material strain hardening and softening at the permanent deformation. The model does not consider pressure dependence, effects of cyclic loading or effects of moisture [24], [36].

We begin with the strain decomposition

$$\varepsilon = \varepsilon^e + \varepsilon^p, \tag{2.1}$$

where ε is the total strain, and ε^e and ε^p are the viscoelastic and viscoplastic strains, respectively. Small strain assumption is used throughout the model, as the failure strain is 5%-8%. The viscoelastic and viscoplastic models are developed and presented in 1D for simplicity. The 3D generalization of the constitutive model, combined with moisture degradation studied in *Chapter 3*, is summarized in *Section 4.2*.

2.3.2 Viscoelasticity

The 1D linear viscoelasticity model relates the uniaxial viscoelastic strain ε^e and the stress σ by the following hereditary integrals [55]:

$$\varepsilon^e(t) = \int_0^t D(\psi - \psi')\dot{\sigma}(t')dt', \tag{2.2}$$

and

$$\sigma(t) = \int_0^t E(\psi - \psi')\dot{\varepsilon}^e(t')dt', \tag{2.3}$$

where D and E are the material creep compliance and relaxation moduli, respectively. They are interchangeable and related by

$$\int_0^t E(t - t')\frac{dD(t')}{dt'}dt' = 1. \tag{2.4}$$

In equations (2.2) - (2.3), ψ and t represent the reduced time and the actual time, respectively.

According to the principle of TTS, the time dependent material parameters at temperature θ can be related to those at a single reference temperature θ_{ref} by changing the time scale. The reduced time ψ is related to the actual time t through the integral equation

$$\psi = \int_0^t \frac{dt'}{A_\theta(\theta(t'))} \ , \tag{2.5}$$

where A_θ is the shift function. A common expression for A_θ as a function of θ is the WLF equation,

$$log_{10}\big(A_\theta(\theta)\big) = -\frac{C_1(\theta-\theta_{ref})}{C_2+(\theta-\theta_{ref})}, \tag{2.6}$$

where C_1 and C_2 are material constants. With the principle of TTS, the relaxation moduli can be represented as a function of time at the reference temperature θ_{ref} by the generalized n^{th} order Maxwell model, known as the Prony series,

$$E(\psi(\theta,t)) = E_0 + \sum_{i=1}^{n_G} E_i \exp(-\psi(\theta,t)/\tau_i), \tag{2.7}$$

where E_0, E_i and τ_i are the material model parameters.

2.3.3 Viscoplasticity

We use a temperature dependent, power law viscoplastic flow potential in conjunction with two state variables that can capture both strain hardening and softening. The model here is an adaption of the one in reference [56] in which strain rate is related to stress via a power law of the form

$$\dot{\varepsilon}^p = A_v \exp(-Q_v/k_B\theta)\left(\frac{\sigma}{s}\right)^m, \tag{2.8}$$

where A_v, Q_v and m are material constants. Temperature dependence of the viscoplastic strain rate is in the Arrhenius form $\exp(-Q_v/k_B\theta)$, where Q_v represents the activation energy, $k_B = 1.3806\times10^{-23}\ (J\cdot K^{-1})$ is the Boltzmann constant and θ is the temperature. The state variable s represents the material deformation resistance which evolves with deformation.

The hardening (softening) rule specifies how the state variable evolves. It is observed that the strain rate first decreases then increases at high stress level in the creep test, which indicates the material deformation resistance would evolve non-monotonically. To capture this phenomenon, we adopt the state variable evolution equations of Anand and Gurtin [56]:

$$\dot{s} = h_0\left(1 - \frac{s}{\tilde{s}(\eta)}\right)\dot{\varepsilon}^p, \tag{2.9}$$

$$\dot{\eta} = g_0\left(\frac{s}{s_{cv}} - 1\right)\dot{\varepsilon}^p, \tag{2.10}$$

$$\tilde{s}(\eta) = s_{cv}(1 + \omega(\eta_{cv} - \eta)), \tag{2.11}$$

where η is the second state variable coupled with s, and h_0, g_0, ω and η_{cv} are additional material properties. Initial conditions for s and η are $s(0) = s_0$, $(s_0 \leq s_{cv}(1 + \omega\eta_{cv}))$ and $\eta(0) = 0$. We can show that η would monotonically approach η_{cv} and that s would first increase to some peak value when $s < \tilde{s}(\eta)$ and decrease to a saturation value of s_{cv} as $s > \tilde{s}(\eta)$, which simulates both material strain hardening and strain softening.

Finally, we take the saturated and initial state variables as temperature dependent following a linear model:

$$s_0 = s_0'(1 - \beta(\theta - \theta_{ref})), \tag{2.12}$$

$$s_{cv} = s_{cv}'(1 - \beta(\theta - \theta_{ref})), \tag{2.13}$$

where s_0', s_{cv}' and β are material parameters and θ_{ref} is the reference temperature. As mentioned, this model is a small-strain adaptation of the Anand and Gurtin model [56] with the addition of the Arrhenius relation and of equations (2.12) - (2.13) to model temperature dependence. Back stress and pressure are not included here as the available data do not allow us to evaluate the pressure dependence.

In summary, the model uses linear viscoelasticity with time-temperature superposition and a seven terms Prony series, equations (2.5) - (2.7), combined with the state variable, power law

viscoplasticity model given by equation (2.8) with dual state variables evolving as defined by equations (2.9) - (2.13). The 3D generalization of the above 1D model is based on standard J_2 plasticity and is outlined in *Section 4.2* combined with moisture degradation studied in *Chapter 3*.

2.4 Model Fitting

In this section, we obtain the material parameters of the time and temperature dependent model of HFPE-II-52 polyimide at temperatures from 285ºC to 315ºC. Parameters of viscoelasticity and viscoplasticity are identified separately. First, the viscoelastic parameters are identified using the lowest stress level creep recovery data at all temperatures. Viscoplastic parameters are then fit using all the test data, including the creep recovery tests, multistep relaxation tests and monotonic tension tests.

2.4.1 Parameter identification for viscoelasticity

As shown in Figure 2.3, at the lowest stress levels the creep strain fully recovers after the stress is removed, indicating that the deformation is purely viscoelastic at those stresses. The total measured strain is hence taken as viscoelastic, and for a constant applied stress σ_0, from equation (2.2), we get creep compliance, D, as a function of time for each testing temperature by

$$D(t) = \frac{\varepsilon^e(t)}{\sigma_0} \ . \tag{2.14}$$

The relaxation modulus $E(t)$ is related to the creep compliance $D(t)$ by the integral equation (2.4). We solved equation (2.4) iteratively for $E(t)$ at each temperature, then plotted the results in log_{10} time as shown in Figure 2.5. To apply TTS we selected a reference temperature of $\theta_{ref} = 285$℃. The relaxation moduli curves at the other temperatures are manually shifted horizontally in log_{10} time until the moduli at all three temperatures align onto a single curve. The shift values $h(\theta)$ are

related to the shift function $A_\theta(\theta)$ by

$$h(\theta) = -log_{10}(A_\theta(\theta)). \tag{2.15}$$

The resulting values of the shift functions $A_\theta(\theta)$ at 300ºC and 315ºC are then fit to the WLF equation (2.6) resulting in $C_1 = -25.3$ and $C_2 = -360℃$. Note that the values of C_1 and C_2 are generally negative when the tests are performed at temperatures below T_g. The master curve combining the shifted moduli, shown in Figure 2.5 at the reference temperature of $\theta_{ref} = 285℃$ is fit with the Prony series defined in equation (2.7). The Trust Region Algorithm [57] is used to obtain the material parameters E_i and τ_i as presented in Table 2.1. While the fitting algorithm is well suited to the nonlinear least squares problem, the result can be highly dependent on the initial guesses. The characteristic times, τ_i, are initially established by evenly distributing them in log_{10} time. The technique to initialize E_i can be found in reference [58]. We found that a 7 term Prony series provided an adequate fit. Adding more terms did not improve the fit but did complicate the remaining parameter identification steps.

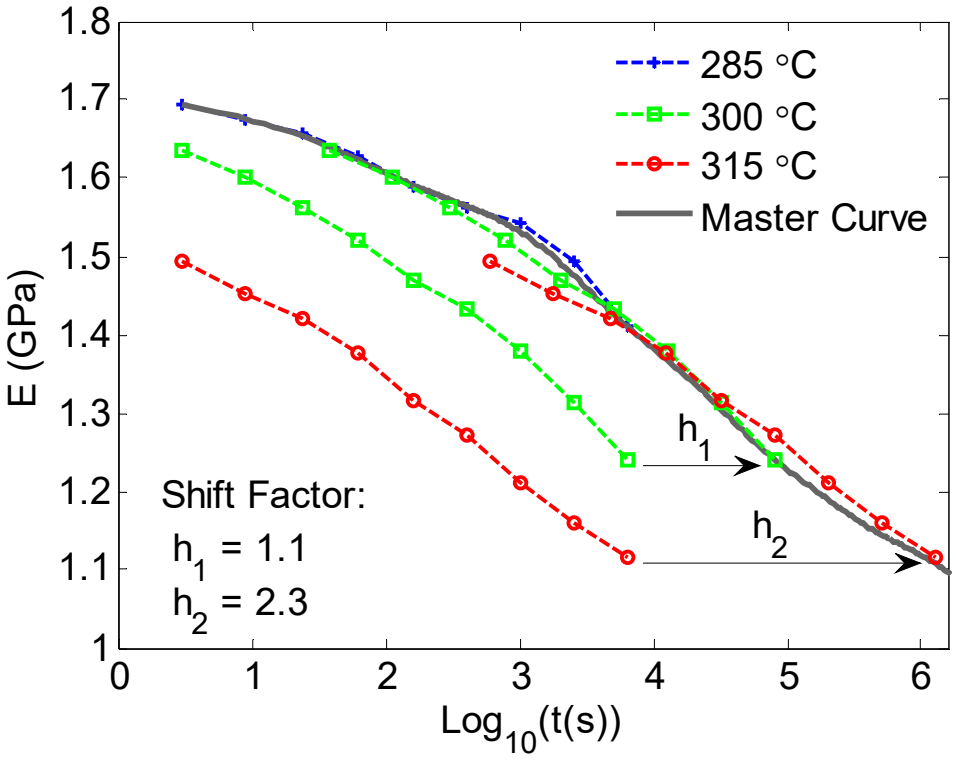

Figure 2.5: Relaxation moduli at different temperatures. Each data set was shifted to the reference temperature of 285°C with the shift factors. Master curve was fit with 7 term Prony series.

Table 2.1: Parameters of 7-term relaxation modulus Prony series

Term	E_i (MPa)	τ_i (s)
0	971.4	
1	25.70	3.853×10^{0}
2	44.73	3.460×10^{1}
3	56.02	1.116×10^{2}
4	152.7	2.580×10^{3}
5	150.6	2.565×10^{4}
6	120.5	1.665×10^{5}
7	192.3	3.712×10^{6}

2.4.2 Parameter identification for viscoplasticity

The experimental data used to determine the viscoplastic parameters include the creep recovery tests, multistep relaxation tests and monotonic tension tests at all temperatures. The constitutive model is described in equations (2.8) - (2.13). With the knowledge of viscoelastic parameters and the strain decomposition, the model parameters are identified by fitting the experimental data sets. The Nelder-Mead simplex algorithm [59], [60] is used. While the algorithm is derivative free and suitable for iterating the parameters in differential equations, the process is highly sensitive to the initial guess of the parameters and only local optimization can be guaranteed. In the following, we discuss how the material constants were initialized and identified.

It is observed that the creep strain is highly sensitive to the stress level, as shown in Figure 2.3, and the strain suddenly becomes unstable at a threshold value of the constant stress loading. In equation (2.8), the strain rate exponent m was thus initially set to a large value (≥ 10). The activation energy Q_v and the pre-exponential parameter A_v were initialized manually to find the right order of magnitude for A_v, considering the overall temperature dependence in all three types of the experiment.

Equations (2.9) - (2.13) determine how the state variables evolve with plastic deformation. Parameter s_0', the material's initial resistance at reference temperature $\theta_{ref} = 285℃$, was initially set to be the stress level where the viscoplasticity is first observed to occur. Similarly, s_{cv}', the saturation value of the deformation resistance at $\theta_{ref} = 285℃$, was initialized to match the failure stress. The temperature parameter β in equations (2.12) - (2.13) was determined from the temperature dependent ultimate stresses at 285, 300 and 315°C. Parameters h_0 and g_0 were initialized to adjust the overall speed of the evolution, while η_{cv} and ω were initially set to match the peak stresses in the fixed strain rate tension tests.

Once initialized, the material parameters were optimized via the Nelder-Mead algorithm to fit the data sets. The resulting parameter set is presented in Table 2.2.

Table 2.2: Parameters of the viscoplastic model

A_v (s^{-1})	5.90×10^{6}	ω	730
Q_v (J)	1.60×10^{-19}	η_{cv}	4.97×10^{-4}
m	11.7	s_0' (MPa)	39.6
h_0 (GPa)	9.07	s_{cv}' (MPa)	41.8
g_0	0.116	β	0.0043

2.4.3 Discussion and comparison of model to experimental results

The experimental and model results are plotted together and compared in Figures 2.6 – 2.12. Recall that the strain is the sum of the viscoelastic and viscoplastic contributions. Over the set of test types and range of time, load, strain and temperature the model captures the overall creep/recovery, stress relaxation and monotonic loading behaviors. The linear viscoelastic model fits the experimental data well at low stress levels in the creep recovery tests and the relaxation tests at different temperatures. The model predicts the initial stiffness in the monotonic tension tests less accurately. Noticing the different time scales in those data sets (less than 1 minute in the monotonic tension tests and several hours in the creep or relaxation tests), the conclusion can be made that the model does a better job of representing the long term (more than several minutes) viscoelastic deformation than the short time behaviors. It is recommended to use the results of Antonakakis et al. [31] if the short time viscoelastic behavior of HFPE-II-52 polyimide is needed. Note that the viscoplastic effect is approximately zero at stress levels below about 0.3 UTS. Comparing the experimental creep and recovery data to the model, it is observed that in some cases strains are overestimated during unloading. This reflects our choice to maintain a relatively simple model that

does not incorporate nonlinear viscoelasticity which would increase the recovery from high stress levels. In the creep tests, the strains become unstable at threshold stresses that differ for each temperature. The onsets of the unstable strains are very sensitive to the stress level. The sensitivity, even though a large m value is used, is somewhat underestimated in the model, i.e. the predicted creep instability stress is about 0.05 UTS lower than measured, and the relaxation at high strain values is faster in the experiments than the model. Thus this model does not accurately capture the final stages where strain accumulates and the material starts to fail. While parameters could be adjusted to fit the creep data the resulting model would then suffer with respect to prediction of monotonic loading.

Prior studies on polyimides [20], [44], [54] focused on a single type of loading, i.e. creep, in a stress range well below failure. The models discussed in these papers provide good fits to the limited data considered, but their applicability to other loading types and stress ranges is unclear. Developing a model applicable across the full range of loading types and stress levels is a challenge that, to a certain extent, involves a balance in terms of capturing all behaviors.

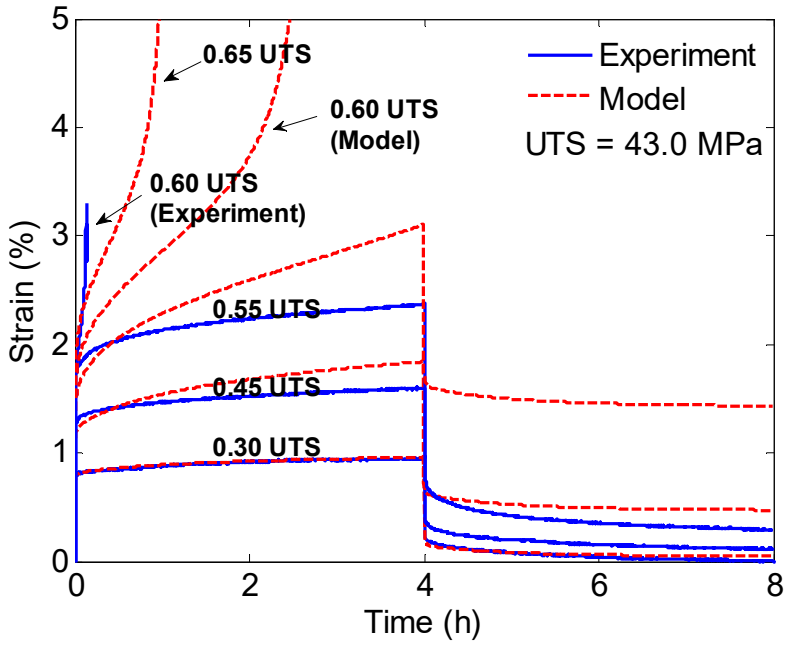

Figure 2.6: Experimental data and model comparison for the creep recovery test at 285°C

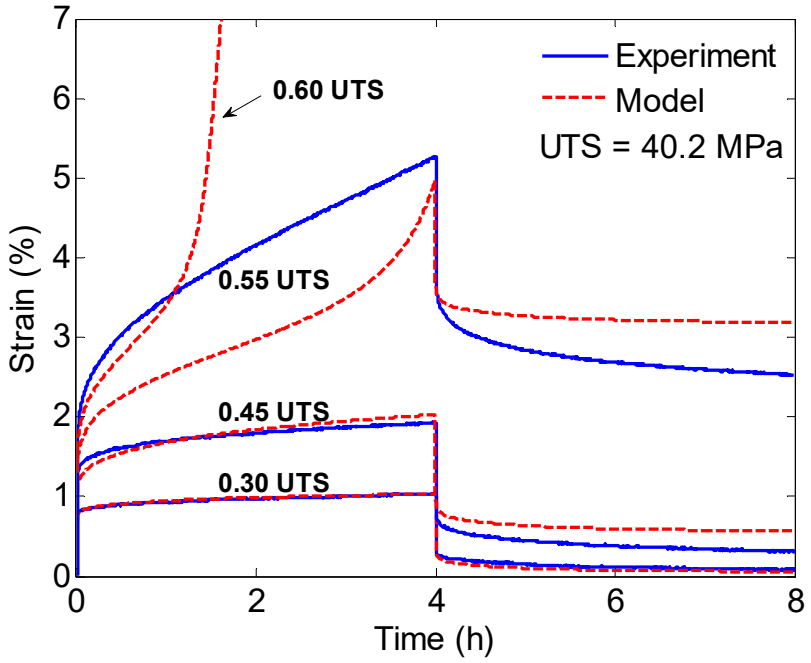

Figure 2.7: Experimental data and model comparison for the creep recovery test at 300°C

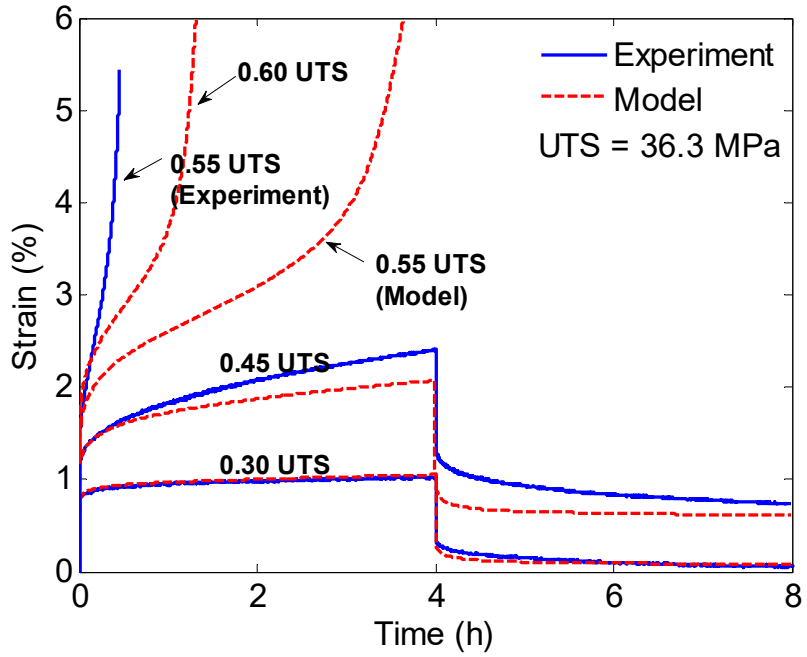

Figure 2.8: Experimental data and model comparison for the creep recovery test at 315ºC

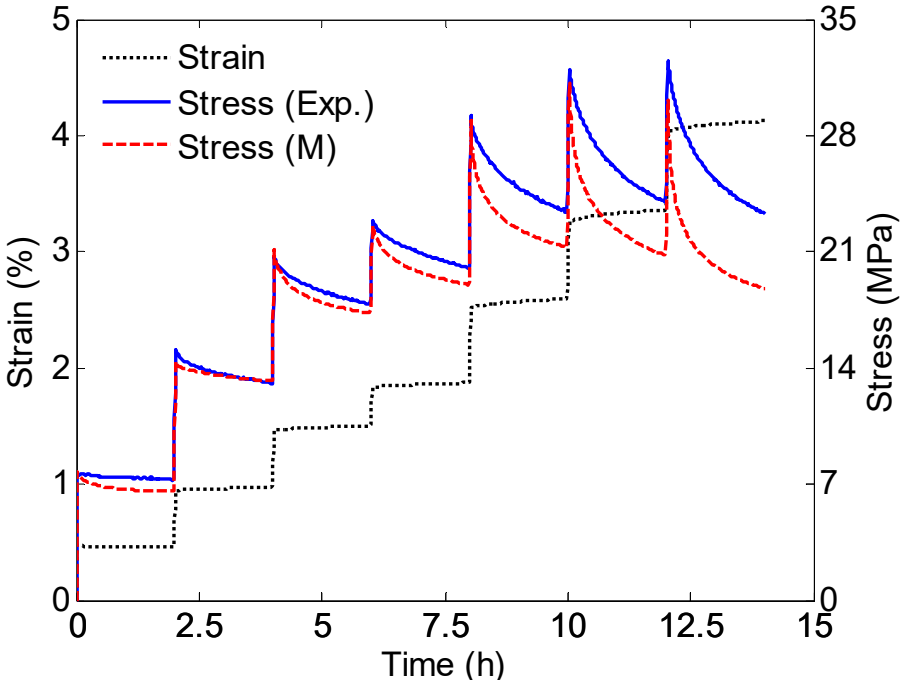

Figure 2.9: Experimental data and model comparison for the multi-step relaxation test at 285ºC

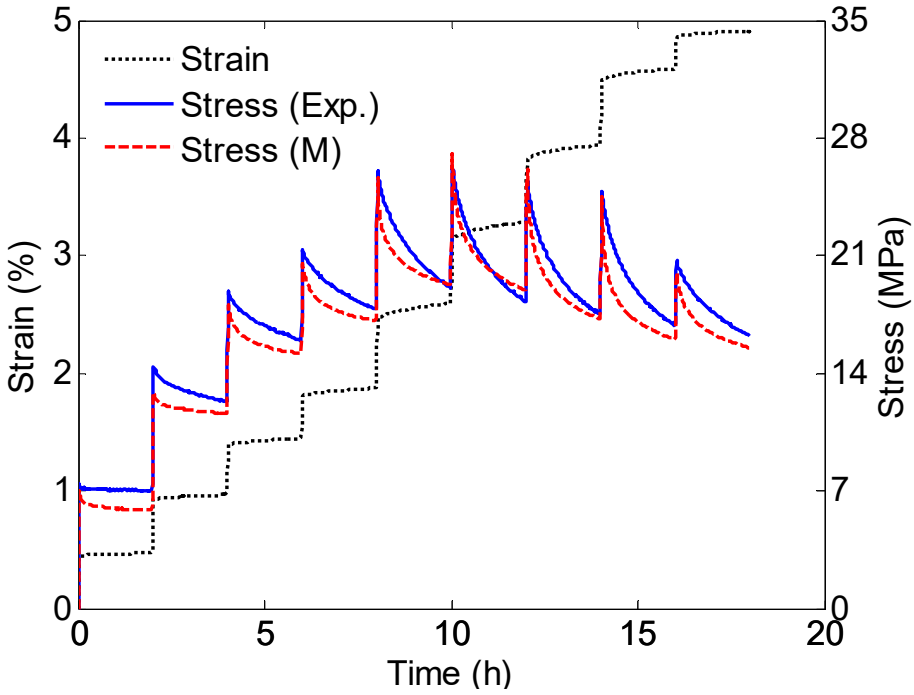

Figure 2.10: Experimental data and model comparison for the multi-step relaxation test at 300ºC

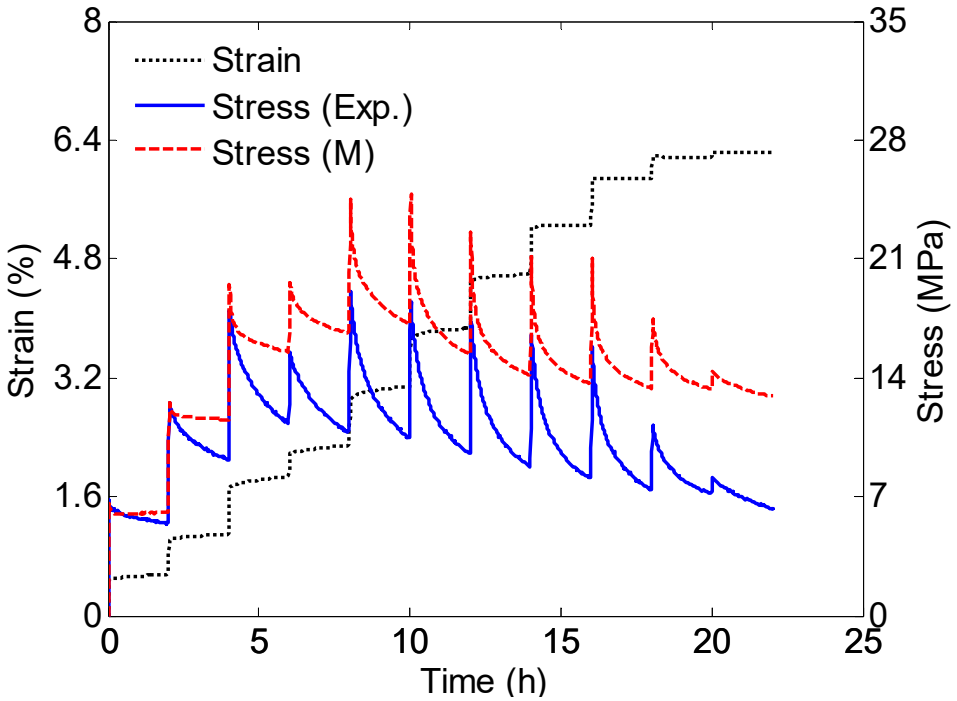

Figure 2.11: Experimental data and model comparison for the multi-step relaxation test at 315ºC

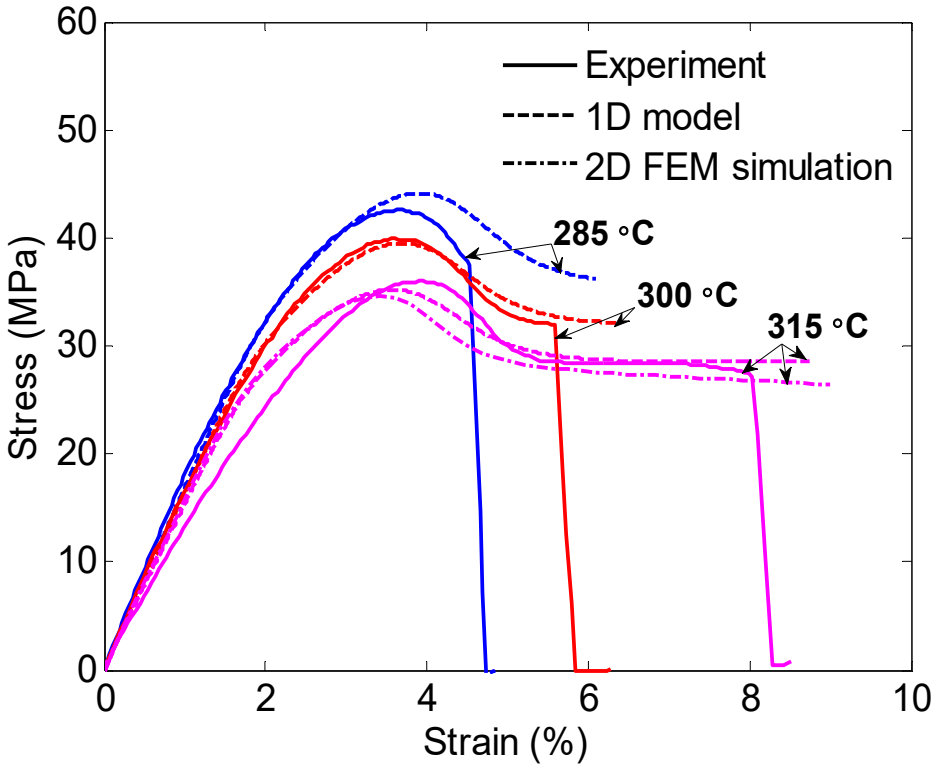

Figure 2.12: Experimental data and model comparison for the fixed strain rate tension tests at different temperatures

2.5 Example Applications of Model

The viscoelastic and viscoplastic constitutive equations have been generalized to 3D (outlined in *Section 4.2* combined with moisture degradation), and implemented into the commercial FE code ABAQUS as a user defined material model. To test the user material, the experiments were simulated using a simple one-element model in both 3D and in plane stress. The results of the FEM computation agree perfectly with the model equations presented above. As an example of how to apply the model in 2D/3D in a practical application, FE simulations of a dogbone tension test of the resin and of a unidirectional carbon fiber/polyimide matrix laminate under shear loading were performed.

2.5.1 Simulation of 315°C tension test

Using a 2D, plane-stress model we simulated the monotonic tension test of the dogbone shaped HFPE-II-52 polyimide sample at a temperature of 315°C and strain rate of 10^{-3}/s. In the experiments a slight amount of necking was observed. To seed necking in the FE simulation an imperfection represented by a 1% local reduction in the cross-sectional width is introduced into the model geometry. Results of the simulation at an overall strain level of 8% are shown in Figure 2.13, where the axial (ε_{yy}) strain component is plotted on the deformed geometry. Strain localization in the form of a 45° shear strain concentration emanating from the edge of the sample can be seen near the region seeded with a geometric imperfection. Similar to the experiments, a slight amount of necking is evident from the increased strain level near the shear band. The resulting stress-strain curve from the FEM simulation is superimposed with the data and 1D model in Figure 2.12. Note that the strain plotted from FEM is an average over the gauge length of the extensometer used in the monotonic tension tests. Up to the peak load the FEM result exactly matches the 1D model. Beyond the peak load, the reduction in cross section and onset of necking causes the nominal stress in the FEM calculation to drop below the 1D model prediction.

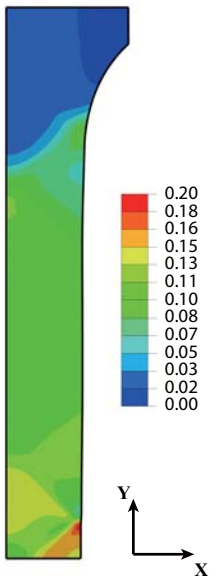

Figure 2.13: Simulation of 315°C tension test. Axial strain, ε_{yy}, over the deformed configuration of 1/4 of the dogbone sample at the experimental failure point of 8% nominal strain.

2.5.2 Simulation of unidirectional composite under axial shear loading

For the second example application, we determined the yield stress of a carbon fiber (T650-35) reinforced HFPE-II-52 polyimide matrix unidirectional composite under axial shear loading at high temperatures. Assuming the fibers form a periodic array in the matrix, a unit cell model can be used [61]. Two packing geometries, square array and diamond array, are considered. Using symmetry, only a quarter of the unit cell is modeled, see Figure 2.14. The shear boundary conditions are applied as follows. The four faces, top ($y = a$), bottom ($y = 0$), left ($x = 0$) and right ($x = a$) are fixed in both x and y directions. The displacement of the left surface is constrained additionally in the z direction. In addition, the stress and strain fields should not depend on z direction. Thus, a multi-point constraint is imposed such that all displacement components on the front surface ($z = l$) are equal to those on the back surface ($z = 0$). A z

direction displacement controlled loading is given on the right surface. A detailed explanation of the model boundary conditions can be found in reference [62].

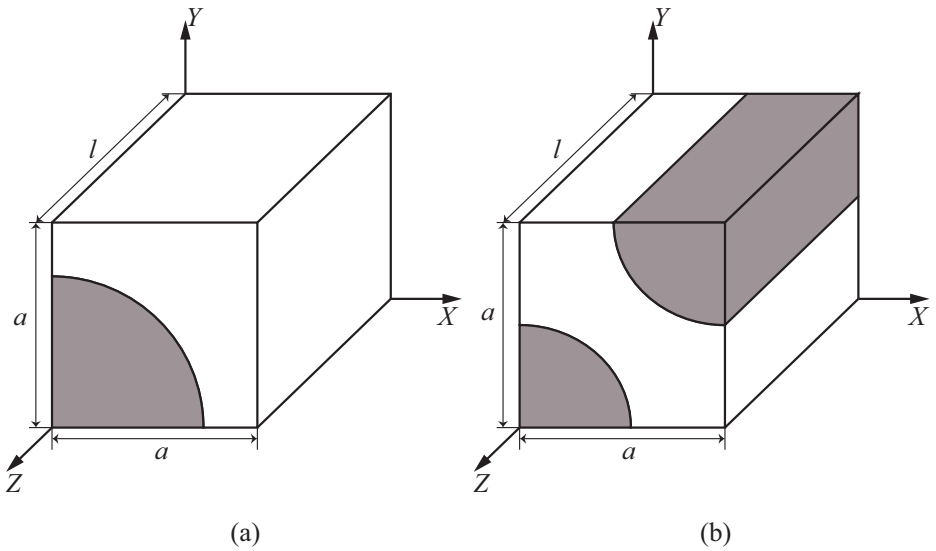

Figure 2.14: 3D unit cell model of unidirectional fiber reinforced composite under axial shear loading. (a) unit cell of square array; (b) unit cell of diamond array.

The fiber is assumed to be time-temperature independent anisotropic elastic. The properties of T650-35 fibers are given in Table 2.3. (Fiber is unidirectional and lies along the z direction.)

Table 2.3: Elastic properties of T650-35 fibers [63]

E_{zz} (GPa)	E_{xx} (GPa)	G_{zx} (GPa)	G_{yx} (GPa)	ν_{zx}
224	15.4	21.1	5.8	0.44

The volume fraction of fibers and polyimide matrix are set to be $V_f = 57.8\%$ and $V_m = 42.2\%$, matching reference [64] for the purpose of comparison to experimental data. The FE simulations were then performed at 315°C on square and diamond packing geometries. The loading rate is $\dot{\varepsilon}_{yz} = 0.0027/s$. Note that once the multi-point constraint is imposed, the stress

and strain fields are independent of the choice of the dimension l. From the simulation results, the yield point is determined using the empirical 0.2% offset method. The results are shown on Table 2.4. For diamond packing at 315ºC a yield stress of 24.8 MPa is predicted, about 10% lower than the 28 MPa yield strength measured by Bhargava and Zehnder [64] using a modified Iosipescu sample at the same loading rate and temperature. Note that the fibers are packed more like a diamond than a square array.

Table 2.4: Results of unit cell model at 315ºC for different packing geometries

	Yield stress (MPa)	Max stress (MPa)	Initial stiffness (GPa)
Square	19.8	22.2	2.16
Diamond	24.8	25.1	2.15

To demonstrate the temperature and rate dependent nature of the model, a parametric study was conducted on the square array packing by varying the temperature by up to 30ºC and loading rate by ±10×. Results are shown on Table 2.5. Over a 100× increase in strain rate the laminate's shear yield stress is predicted to increase by 40%. Similarly a 30ºC decrease in temperature increases yield stress by about 25%. These results are given as examples of design calculations for polyimide laminates at high temperatures.

Table 2.5: Results of the square array unit cell model for different temperatures and loading rates. Baseline loading rate is $\dot{\varepsilon}_{yz} = 0.0027/s$.

Temperature (°C)	Loading rate	Yield stress (MPa)	Max stress (MPa)	Initial stiffness (GPa)
315	$0.1\,\dot{\varepsilon}$	16.9	18.3	2.04
315	$\dot{\varepsilon}$	19.8	22.2	2.16
315	$10\,\dot{\varepsilon}$	23.8	26.8	2.23
300	$\dot{\varepsilon}$	22.6	25.0	2.24
285	$\dot{\varepsilon}$	24.8	28.0	2.29

2.6 Conclusions and Future Work

Based on the extensive mechanical tension tests at high temperature, a time and temperature dependent constitutive model for polyimide was developed. This model is applicable to low and high stress levels. The model includes linear viscoelasticity with the Prony series representation of the relaxation modulus and TTS using the WLF equation. The nonreversible deformation was modeled by the power law flow potential viscoplasticity with dual state variable evolution. The constitutive model was implemented as an ABAQUS user material for FE applications.

The model incorporates results from three distinct types of loading histories and captures the key features of the material behavior. The model is able to accurately predict the time temperature dependent deformation at low stress level in the time span from about 1 minute to several hours. The model is also able to capture the creep strain at moderate stress level. The model does not include nonlinear viscoelasticity and does not deal with cyclic loading behaviors. The flow potentials for polymers are usually pressure dependent [52], [53], which is not investigated in this study. With pressure dependence, equation (2.8) becomes

$$\dot{\varepsilon}^p = A_v \exp(-Q_v/k_B\theta)\left(\frac{\sigma}{s+\xi p}\right)^m, \tag{2.16}$$

where p is the pressure ($p = -\frac{1}{3}\sigma_{kk}$) and ξ is the parameter that can be determined with additional shear and/or compression tests.

Finally, at high temperature, the mechanical response of polyimides is known to be moisture dependent [6], [24], [65]. The time and temperature constitutive modeling presented in this chapter is combined with moisture effects (presented in *Chapter 3*) to form a full time, temperature and moisture dependent model for use of thermosetting polyimides in hot-wet environments. Finite element applications of polyimides under hygrothermal loadings are then investigated in *Chapter 4*.

CHAPTER 3

MOISTURE DEGRADATION

3.1 Introduction

Thermosetting polyimides are an important class of high temperature polymers with a broad range of applications due to their high glass transition temperature (T_g up to or beyond 350°C), toughness and specific stiffness and strength [14], [38], [39]. They are mainly used as a matrix for fiber reinforced composites and have extended the role of traditional polymer matrix composites (PMCs) to applications in high temperature and other harsh environments. However, polyimides or polyimide matrix composites (PiMCs), when operated or stored in hot, high humidity environments can suffer significant degradation leading to structural failure. For example, studies have shown that blistering [33], [34], [36] and delamination [34], [35] can occur when samples that have been held in a moist environment are rapidly heated. The role of moisture in these failures can be divided into two parts. One part is that the moisture absorbed in the polyimide can induce internal vapor pressure at temperatures above 100°C. The other part is that the material properties themselves are weakened by the hot wet environment.

This chapter focuses on understanding the second part: material moisture degradation and how it affects the mechanical performance of a polyimide resin. The goals of the study are to develop an overall understanding of the effects of the hot-wet environment on mechanical properties and to quantify these effects as functions of moisture, temperature and time. These results will be used to develop a kinetic model that will, in *Chapter 4*, be integrated with prior work presented in *Chapter 2* to build a temperature and moisture dependent constitutive model of polyimides. Such a model will allow designers to account for both moisture and temperature of polyimides or PiMCs

as used in hygrothermal environments and to predict failure and/or safe operating conditions. All experimental data are obtained with a specific polyimide, HFPE-II-52 [14], [22]. However, the approach described here can be readily applied to other thermosetting polyimides or high temperature polymers.

One of the underlying mechanisms of moisture degradation of polyimide is hydrolysis, or breaking of bonds due to reaction with water. The rate of bond breaking is sharply temperature dependent and will have a permanent, adverse effect on the polyimide's mechanical performance. In an early study of hydrolytic degradation, thermoplastic polyimide (DuPont Kapton) samples were immersed in water at temperatures from 20 to 100°C for time intervals ranging from one hour to one month [24]. Significant hydrolytic degradation was observed as reflected through reductions in tensile strength and elongation to failure. In subsequent studies the conditioning temperature was extended beyond 100°C by using a sealed pressure tube filled with water [30], [66]. Using this method, Rice [66] investigated hydrolytic degradation of the polyimide AFR700B. The result shows, for instance, a 49% deterioration of the tensile strength after moisture exposure at 150°C for 2 days. In a series of studies, Shin and Morgan [29], [30], [67] investigated several thermosetting polyimides and composites, finding that the onset of hydrolysis and of measurable changes in the mechanical performance depend on the exposure time and temperature. For example, K3B polyimide lost 18% strength after moisture exposure at 160°C for 42 days, but lost about 95% of strength after exposure at 200°C for 1 day.

Another underlying mechanism of moisture degradation is that water can act as a plasticizer, causing instantaneous reductions of stiffness and flow strength. The effect of plasticization is reversible and can only be revealed while enough water is present in the material. Harper [26] studied the effect of plasticization on the relaxation modulus of polyimide at temperatures below

100°C. Little data exist for temperatures above 100°C since samples rapidly dry out at these temperatures. Shimokawa [68] observed a reduction of compressive strength of PiMC at high temperature 260°C when moisture is partially maintained in the material. Burcham [69] found the presence of a reversible moisture effect on a PiMC by measuring the T_g in both saturated and re-dried conditions.

In this study, experiments have been designed and conducted to address both hydrolysis and plasticization of the polyimide HFPE-II-52 with a focus on the reduction of mechanical properties due to material moisture degradation. To study hydrolytic degradation, samples are exposed to hot wet conditions in a moisture filled, sealed tube at temperatures from 200°C to 250°C and durations from 15 minutes to 9 weeks. Samples are then compression tested at room and high temperatures to quantify the reduction of elastic stiffness and yield stress. A related but separate set of plasticization experiments were performed to quantify the reduction of stiffness and strength as a function of testing temperature and moisture level. Incorporating hydrolysis and plasticization, a kinetic model is developed to relate the stiffness and yield strength to the history and current level of moisture and temperature. The model is fit to the experimental data. These experiments and models aim to provide a means for predicting the onset and degree of moisture degradation and its effect on mechanical performance of the polyimide. The small number of reports discussed above and the present work constitute, to the author's knowledge, the entire body of research in the open literature on moisture degradation of polyimides. Thus the data presented here represent a significant addition to the body of knowledge of hydrolytic degradation and plasticization in polyimides.

3.2 Experimental Method

Related, but separate experiments were conducted for the hydrolytic degradation and plasticization studies. For hydrolytic degradation, samples are exposed to high temperature, moisture and pressure in a sealed tube for a range of time and temperature. They are then dried and tested in compression. Sample weight gain during hydrolytic degradation is recorded. For plasticization, samples are first fully moisture saturated then tested at different temperatures. The testing time is kept short so that moisture is maintained in the samples during the plasticization tests. The detailed experimental set-up and procedures are presented in following sub-sections.

3.2.1 Sample preparation and experimental setup common to both studies

3.2.1.1 Sample preparation

The samples used for all tests were fabricated by compression molding of HFPE-II-52 polyimide powder at 172 atm pressure and a maximum temperature of 377ºC for 2 hours. The polyimide plates were post cured at 371ºC for 16 hours. The material's glass transition temperature, T_g is 351ºC [31]. Details on the HFPE-II-52 synthesis, molding procedure and cure cycle can be found in reference [14]. The plates were then cut into 5 × 5 × 4 mm specimens with a diamond wire saw. Before moisture exposure and testing all samples were dried for 3 days at 70ºC in a vacuum chamber.

3.2.1.2 Pressure tube for moisture conditioning

In this study, we adapt the pressure tube method of reference [30] to hold steam pressure at high temperatures. A capped, threaded (1/2'' NPT), heavy duty stainless steel tube rated to 45MPa is used as shown in Figure 3.1. High temperature (rated to 285ºC) TaegaSeal thread sealant tape is used to maintain the seal and minimize seizing of the cap to the tube. Leak tests were performed

by adding enough water to the tube (approximately 7 grams) to maintain saturated conditions, weighing the tube, then heating to 250°C for 1 day, then reweighing the tube. To within a resolution of 0.1 g no weight is lost, confirming that the seal is maintained during high temperature exposure. Inside the tube, the polyimide specimen rests on a piece of stainless steel mesh underneath which is placed a pack of fiberglass soaked in distilled water. This setup prevents the sample from directly interacting with liquid water, since it is suspected that the hydrolysis may be different with exposure to liquid water rather than water vapor [30].

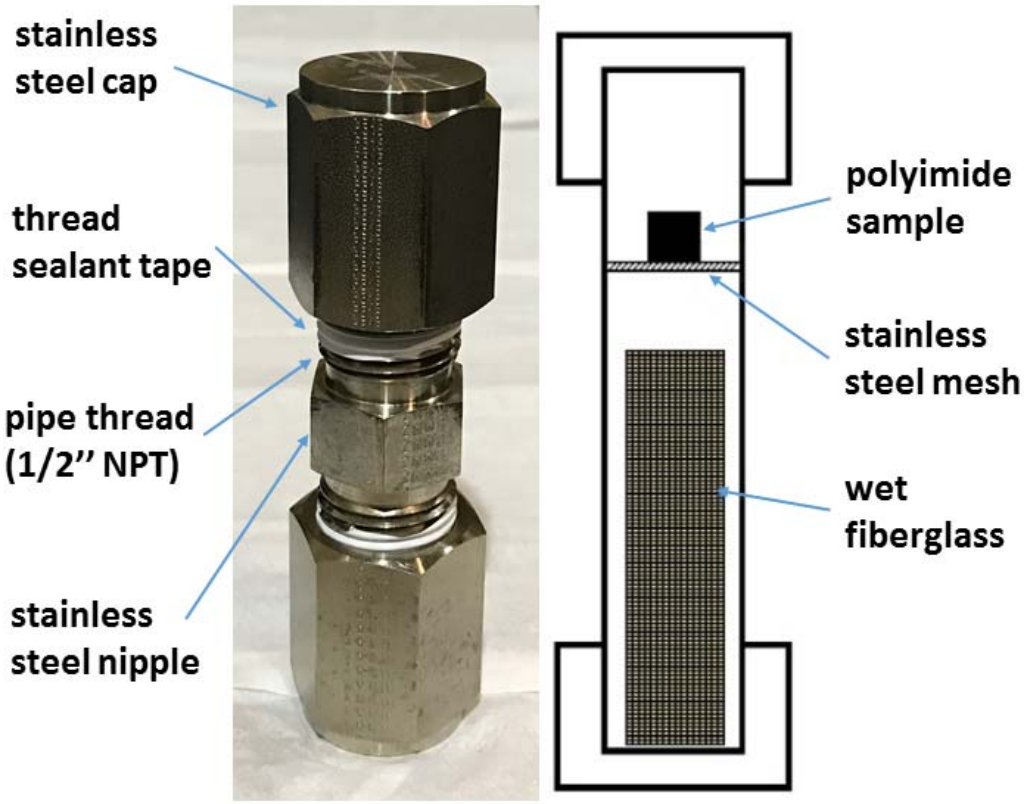

Figure 3.1: Sealed stainless steel tube set-up. NPT: national standard taper pipe thread.

3.2.1.3 Compression testing setup

For both the hydrolytic degradation and plasticization studies, compression tests are performed to

measure the reduction of mechanical properties of polyimide. The tests are performed using an MTS 45 kN servo-hydraulic testing system. Two 25 mm diameter stainless-steel rods are used to compress the sample. For compression tests at elevated temperature, a clam shell furnace (ATS 3210) is used to heat the sample and the loading rods to desired temperature. Two K-type thermocouples are mounted at two sides of the upper rod. One is used for temperature control and the other is used to verify temperature uniformity. The tips of the thermocouples are placed just touching the underneath surface of the upper rod. To check that the temperature at the center of test sample is close to the set point temperature, a dummy specimen was created by gluing two half sized samples together with a thermocouple embedded between them. The difference between the temperature at the center of dummy specimen and the control temperature is less than 2^{o}C. For both room and elevated temperature tests, the polyimide samples are loaded in displacement control at a nominal strain rate of 10^{-3}/s. The compressive stress-strain curve is recorded and analyzed to determine the initial (elastic) stiffness and yield stress. The yield stress is defined using a 1% strain offset. The experiments quantify the reductions in these properties relative to undegraded (virgin) samples.

3.2.2 Procedures for hydrolytic degradation study

3.2.2.1 Fully moisture saturated conditions

The experimental procedures in this section aim to characterize the history dependent moisture degradation and its permanent effect on the mechanical properties of polyimide. A range of conditioning temperatures and exposure times are chosen as shown in Table 3.1. No significant degradation was observed for saturation temperatures below 200^{o}C. For temperatures above 250^{o}C, the rate of degradation is so high that samples come apart in a time shorter than the sample

can be heated, cooled and removed from the pressure tube.

Table 3.1: Matrix of temperature and time exposure for hydrolytic degradation study under fully saturated conditions

Temperature (°C)	Durations
200	1 day, 3 days, 1 week, 2 weeks, 3 weeks, 6 weeks, 9 weeks
205	1 week, 2 weeks, 4 weeks
210	1 day, 3 days, 7 days
215	3 hours, 6 hours, 12 hours, 1 day, 3 days, 7 days
225	1 hour, 3 hours, 6 hours, 12 hours, 1 day, 3 days
235	45 mins, 1.5 hours, 3 hours, 6 hours, 12 hours, 1 day
250	15 mins, 30 mins, 1 hour, 2 hours, 4 hours

The step by step experimental procedure for the hydrolytic degradation study is as follows:

(1) Weigh the dry sample, then place it inside the pressure tube with enough water absorbed by the fiberglass to maintain full saturation. Tighten the end caps to seal the tube.

(2) Place the pressure tube into a preheated lab oven.

(3) Once the desired time has elapsed, remove the tube from the oven, let it cool and take the sample out of the tube. Weigh the sample to record its weight, w_{wet}, after hot wet conditioning.

(4) Dry the sample again in a vacuum chamber and weigh it to record w_{dry}.

(5) Smooth all surfaces of the sample flat and parallel using 100 grit paper.

(6) Conduct the compression test at room or high temperature until the material fails.

(7) Analyze the compressive stress-strain curve to measure the initial stiffness and yield stress.

The samples are weighed with a microbalance (Mettler-Toledo A280) with a resolution of 10^{-4}

gram. The weights are recorded for monitoring the weight gain $\frac{w_{wet}-w_{dry}}{w_{dry}}\times 100\%$ during hydrolytic degradation. For degradation temperatures of 215, 225 and 235°C, samples were tested at both room (20°C) and high (285°C) temperatures. For the other degradation temperatures, samples were tested only under room temperature compression.

For short term exposures to the hot wet conditions (≤ 3 hours), the samples are pre-moisture saturated at low temperature (125°C) for 1 day before being placed in the pressure tube for exposure at the desired temperature for hydrolytic degradation. By pre-saturating the sample the uniformity of the moisture concentration is improved for these shorter time exposures. Note that for a 1 day exposure no degradation will occur at a temperature 125°C.

3.2.2.2 Partially moisture saturated conditions

The rate of degradation is expected to depend on the amount of water the sample absorbs, with faster rates of degradation occurring for fully moisture saturated conditions than for partially saturated conditions. To quantify the dependence of the hydrolytic degradation rate on saturation level, samples are exposed to high temperatures but at less than fully saturated conditions. To develop such conditions, the approximate amount of water, w_1, needed to fill the tube at 100% relative humidity (RH) at the desired temperature is calculated. Then the amount of water, w_2, the sample would absorb under fully saturated conditions is calculated. Varying the initial amount of water in the tube from zero to $w_1 + w_2$ a series of hydrolytic degradation exposures are performed. The amount of water absorbed by the sample is measured, allowing the percentage weight gain to be calculated. Fiberglass is not used in the partially saturated conditions tests since there should be no additional liquid water in the tube at the desired temperature and the fiberglass may disturb the humidity spatial distribution in the tube. Note that since the RH varies during sample saturation,

the results represent the integrated effect of degradation under less than fully saturated conditions.

3.2.3 Procedure for plasticization study

In the previous section, permanent moisture degradation is investigated. In this section, experiments to explore the reversible moisture effect, plasticization, are described. Specifically, the instantaneous moisture degradation as a function of temperature and material moisture level is studied by conducting compression tests at different temperatures with samples that have different moisture levels. The temperatures are chosen to be 100, 125, 150, 175, 200 and 225°C. At temperatures below 100°C, no instantaneous, reversible moisture effects were found [31]. At temperatures above 225°C, the moisture diffusivity is so high that no significant moisture can be maintained inside the sample while conducting the compression tests. In addition, at higher temperatures, the rate of hydrolytic degradation is fast enough to cause permanent degradation before the samples are dried out. In such a case the resulting reductions of mechanical properties due to plasticization would be confounded by hydrolytic degradation.

All samples start from full saturation (3.2% water absorption by weight, independent of temperature if below 200°C [70]) before the compression test. The sample's moisture level during testing is controlled by holding the sample at temperature for different times before starting the compression test. At minimum, the sample is held for 2 minutes to allow it to equilibrate with the set point temperature. The steps of the experiments are:

(1) Place the dry sample (weighed as w_0) inside a pressure tube with enough water to maintain fully saturated conditions.

(2) Place the pressure tube into an oven and fully saturate the sample at 125°C for 1 day. At this temperature no hydrolytic degradation will occur.

(3) Preheat the clamshell furnace for the compression test at the desired testing temperature, θ.

(4) Remove the tube from the oven, take the sample out of the tube and weigh it to record its fully saturated weight, w_{max}, right after saturation.

(5) With no delay, place the sample into the preheated clamshell furnace for compression testing and hold for a time t_1. At this point the sample has an unknown weight of w_1. The longer the holding time, the lower the moisture level and hence w_1 will be.

(6) Run the compression test until the sample has reached its yield point. Record the test duration, t_2, which is needed as part of the moisture level computation.

(7) Weigh the sample right after the test and record its weight, w_2.

(8) Analyze the compressive stress-strain curve to measure the initial stiffness and yield stress.

Note that the moisture concentration ϕ is nonuniform inside the sample during the compression test. However, a normalized, average moisture level based on the total weight can be defined as $G(t) \equiv \frac{w(t)-w_0}{w_{max}-w_0}$, where $w(t)$ is the sample weight at any time t. w_0 and w_{max} are the sample dry weight and fully saturated weight, respectively. $G = 1$ for fully saturated sample and $G = 0$ for sample that is completely dried out. The moisture level of the sample during the compression test is bounded by $G_1 = \frac{w_1-w_0}{w_{max}-w_0}$ and $G_2 = \frac{w_2-w_0}{w_{max}-w_0}$, where w_1 is the unknown weight of the sample at the beginning of the compression and w_2 is the sample weight right after compression. G_2 is directly obtained from w_2, and G_1 can be estimated from G_2, the testing temperature θ and testing time t_2 using Fick's diffusion law as outlined in the Appendix 3A. The normalized moisture level during the test is then approximated as the mean of G_1 and G_2 ($\frac{G_1+G_2}{2}$).

3.3 Experimental Results and Discussion

Compression tests were used for measuring the mechanical reductions due to the moisture effects. The baseline mechanical properties are listed in Table 3.2 (6 samples tested at 20ºC, 9 samples for 285ºC). Sample compressive stress-strain curves are shown in Figure 3.3. The yield stress is determined with the 1% offset method. True stress and true strain are used throughout the stiffness and yield stress measurements in this paper. True stress is determined as $\sigma_T = \frac{F}{A} = \frac{F}{A_0(1-\nu\frac{\Delta l}{l_0})^2}$, where F is the measured force, l_0 is the sample's initial dimension in the loading direction, Δl is the applied displacement, A_0 and A are the sample's initial and current cross sectional area, respectively, and ν is the Poisson ratio which is approximated as 0.5. True strain is defined as $\varepsilon_T = \ln(1 + \frac{\Delta l}{l_0})$. The knee region (where the stress curves upward at the start) in the stress-strain plot is due to initial soft contact between the sample and loading platen and is typical of compression testing.

Table 3.2: Mechanical properties of untreated polyimide under compression (mean ± standard deviation)

Temperature (ºC)	Initial stiffness (GPa)	Yield stress (MPa)
20	2.49 ± 0.18	134.2 ± 2.7
285	1.03 ± 0.10	49.4 ± 2.5

3.3.1 Hydrolytic degradation

3.3.1.1 Sample visible changes

Figure 3.2 shows the visible changes of the polyimide cube shaped samples after hydrolytic

degradation for different times at temperatures of 215, 225 and 235ºC. Starting from the third column in Figure 3.2, the surfaces of the samples wrinkle and start to peel off. At the same time, significant swelling is observed. For the last two columns, the samples' corners start to become rounded and the specimens undergo significant deformation. For higher temperature, 250ºC, significant deformation occurs in less than 4 hours. For even higher temperature 280ºC, the samples are essentially melted after a 15-minute exposure. The visible changes to the samples show qualitatively that the permanent moisture degradation is time and temperature dependent.

Figure 3.2: Image of samples after hydrolytic degradation exposed to saturated moisture at different temperatures and durations

3.3.1.2 Reduction of mechanical properties: stiffness and yield strength measured at room temperature

After the samples are treated in 100% RH environment in the pressure tube for different times and temperatures (see Table 3.1), compression tests are conducted at room temperature. Example compressive stress-strain curves are shown in Figure 3.3. Two to three samples were used for each specific time and temperature. The results show that both the material stiffness and strength reduce after hydrolytic degradation.

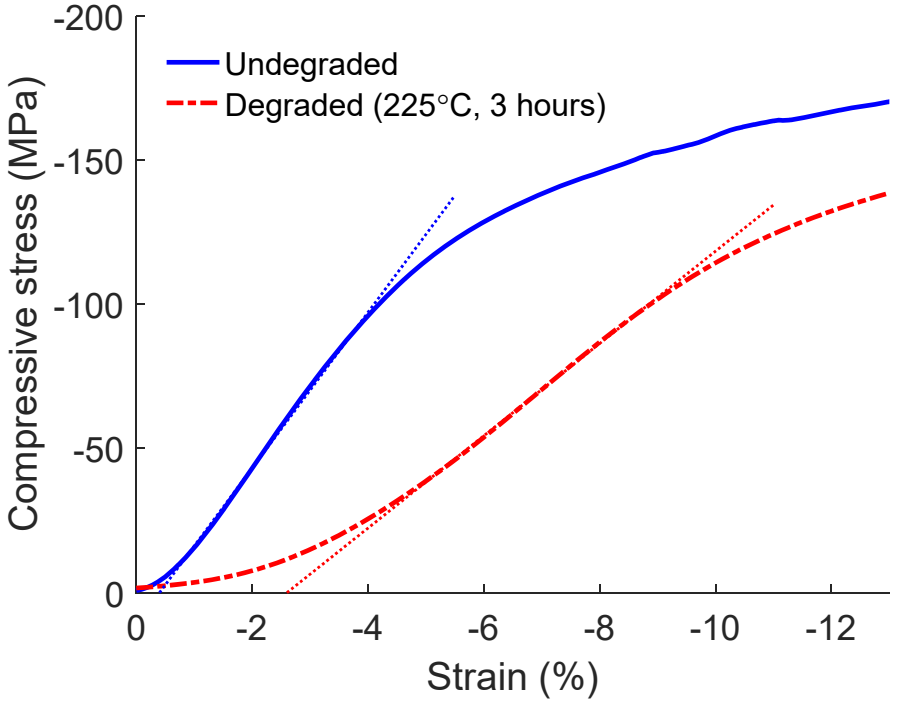

Figure 3.3: Example compressive stress-strain curves for undegraded and degraded specimens tested at room temperature. The dotted lines show the linear fits used to determine initial stiffness.

To quantify the time and temperature dependence of hydrolytic degradation, the initial stiffness and yield stress are measured from the compressive stress-strain curves and compared with the values obtained from unexposed samples. The results are shown in Figures 3.4 – 3.5 in terms of the stiffness and yield stress normalized by the virgin material values. The rate of degradation is seen to be strongly temperature dependent. At 200°C, noticeable stiffness reductions

are observed only after 9 weeks' saturation. For temperatures between 215 to 235ºC, the stiffness retention drops below 20% within a week. For even higher temperatures, 250ºC, significant reductions occur within 15 minutes. Similar trends are observed for yield stress retention, however the minimum yield stress retention we measured is about 40% of the virgin yield stress. We also observed the surprising result that for the lower temperatures and shorter exposures, the material yield strength increased up by 20% relative to the virgin material. One possible reason is that absorbed water can increase the mobility of the polyimide chains and thus promote the formation of additional cross links beyond the links formed during curing and post-curing. However, as the temperature and/or conditioning time increases further, cross links and imide backbone breakage begin to occur, causing reductions of the mechanical performance.

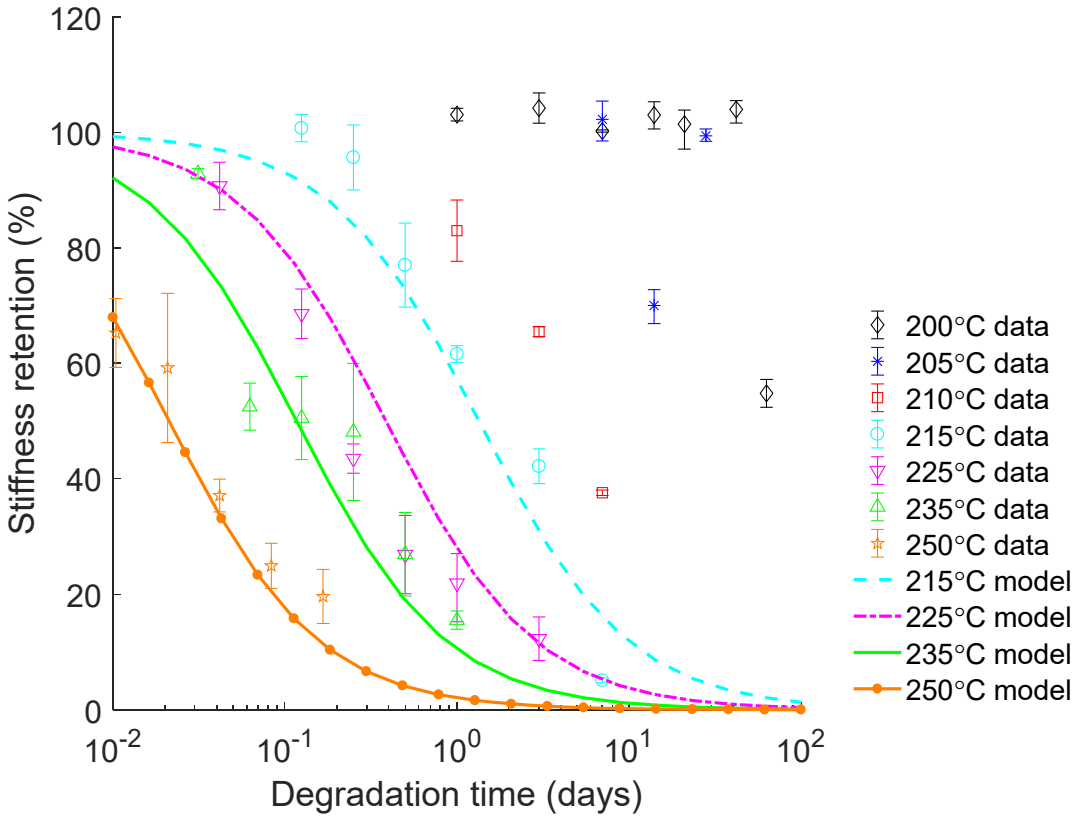

Figure 3.4: Room temperature stiffness retention vs. exposure time (in log scale) for different degradation temperatures. 2 samples were used for each datum point, except for the 200ºC and 205ºC data where 3 samples were used. Error bars indicate the minimum and maximum retention for each condition. Model predictions are included for selected temperatures.

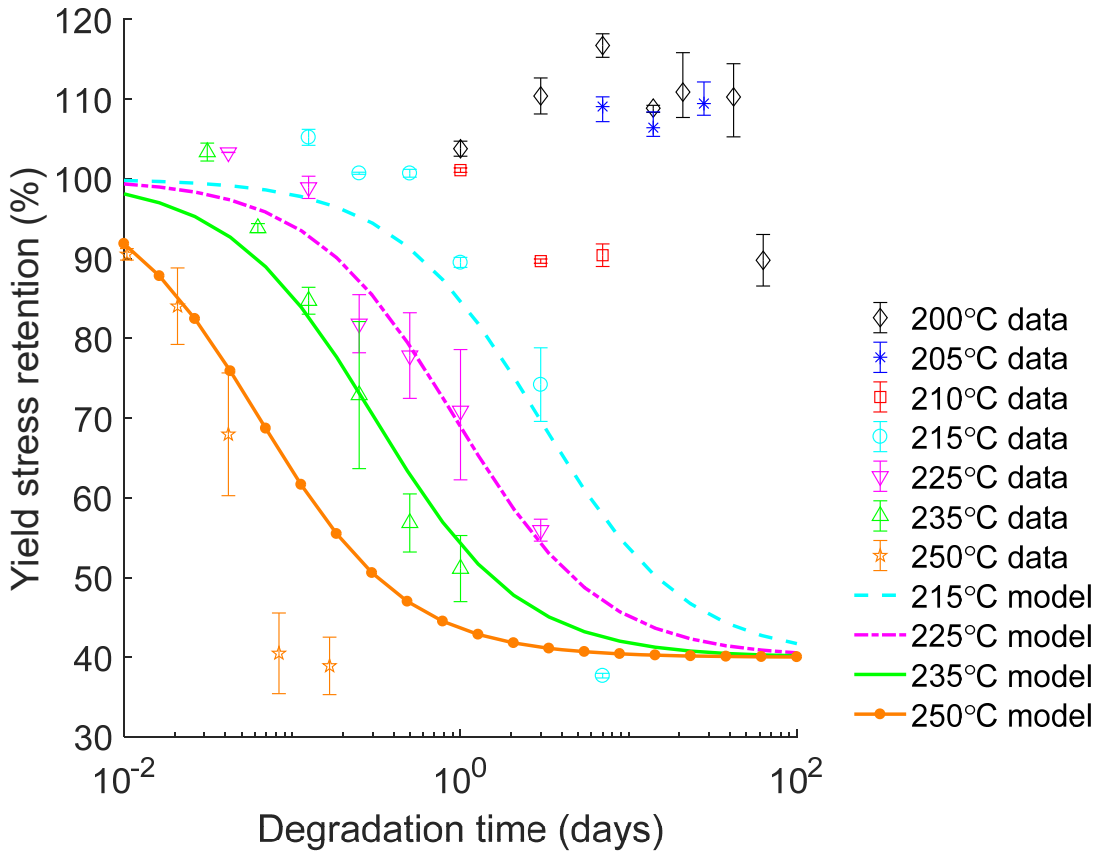

Figure 3.5: Room temperature yield stress retention vs. exposure time (in log scale) for different degradation temperatures. Model predictions are included for selected temperatures.

3.3.1.3 Reduction of mechanical properties: stiffness and yield strength measured at 285°C

Compression tests of the degraded samples were also performed at 285°C to investigate whether the measured normalized reductions of mechanical properties depend on testing temperature. Results for three degradation temperatures, 215, 225 and 235°C are plotted in Figures 3.6 - 3.7. The results are similar qualitatively and quantitatively to the room temperature compression data suggesting that the normalized reductions of mechanical properties after hydrolytic degradation are relatively independent of the testing temperature.

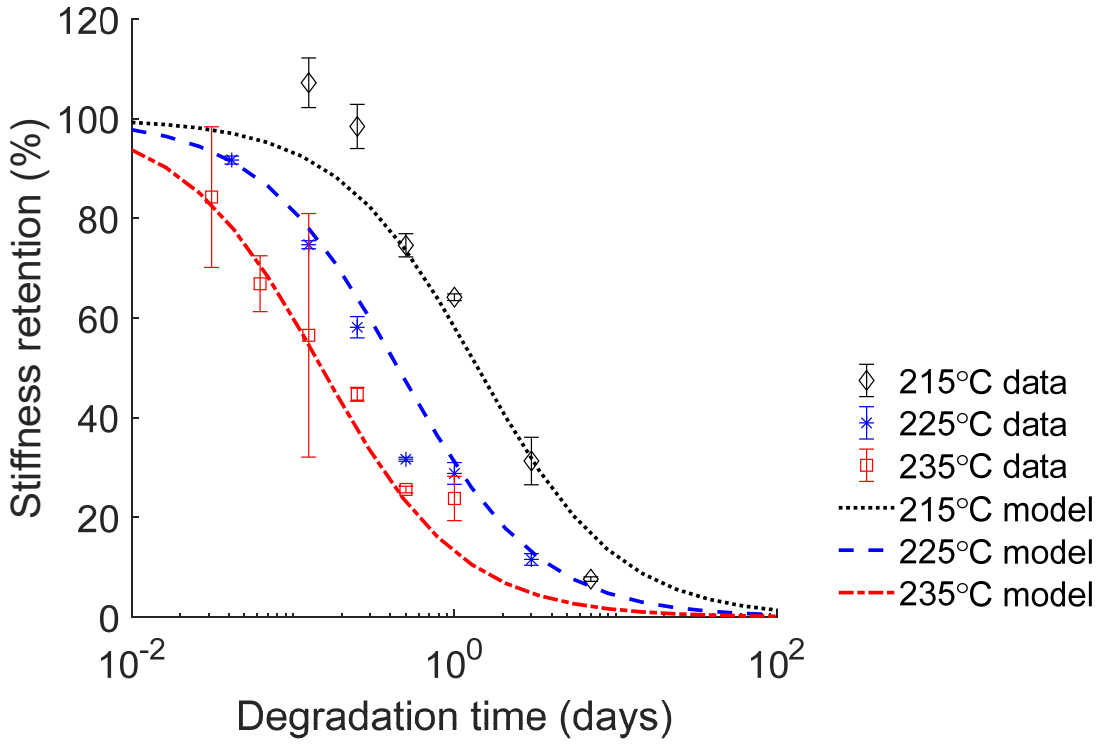

Figure 3.6: Experimental data and model for stiffness retention vs. degradation time (in log scale) for different degradation temperatures. Compression tests conducted at high temperature 285°C. 2 samples were used for each datum point. All error bars indicate the minimum and maximum retention for each condition.

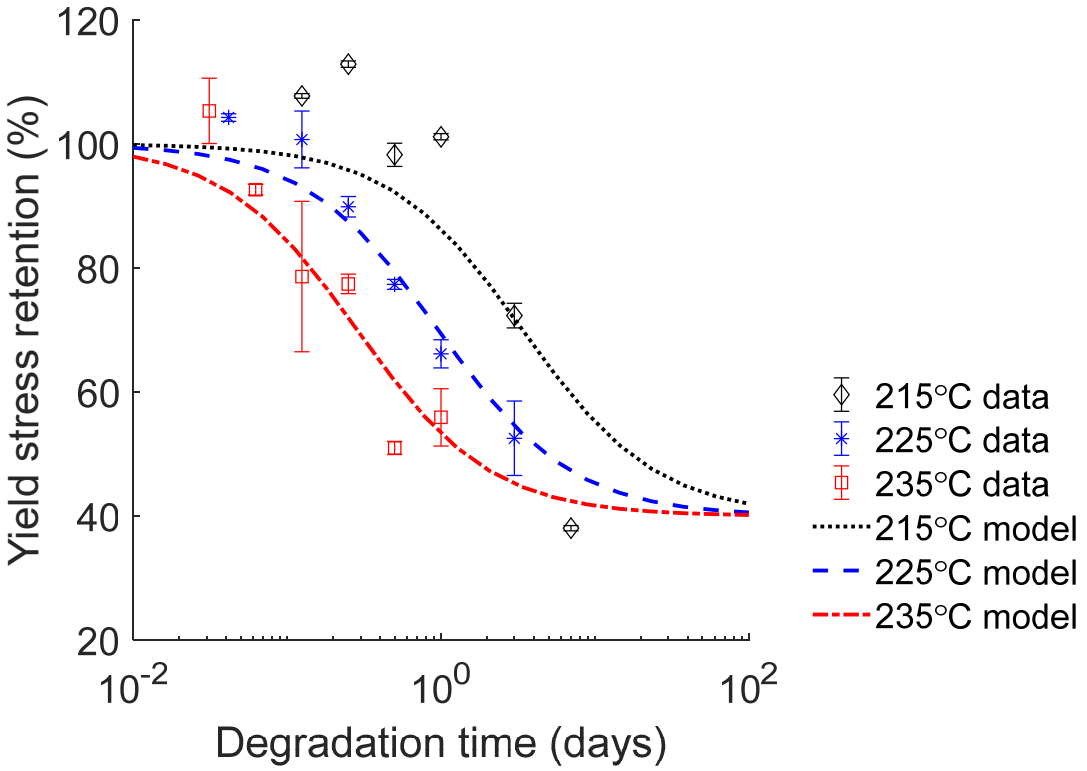

Figure 3.7: Experimental data and model for yield stress retention vs. degradation time (in log scale) for different degradation temperatures. Compression tests conducted at high temperature 285ºC.

3.3.1.4 Mechanical property reductions for partially saturated conditions

In previous sections, all polyimide specimens are treated in the pressure tube with enough water inside to provide an environment of 100% RH. For exposures under less than 100% RH, at 225ºC for 1 day, Figure 3.8 shows the stiffness and strength retentions vs. the samples' moisture weight gain. The solid symbols represent the 100% RH situations and are included in Figure 3.8 for comparison. The retentions are measured at room temperature. It is observed that the retentions of stiffness and strength depend linearly on the weight gain in between dry and fully saturated conditions. It is noticed that there is a small increase of yield stress for low moisture level

saturation, similar to the data in Figure 3.5.

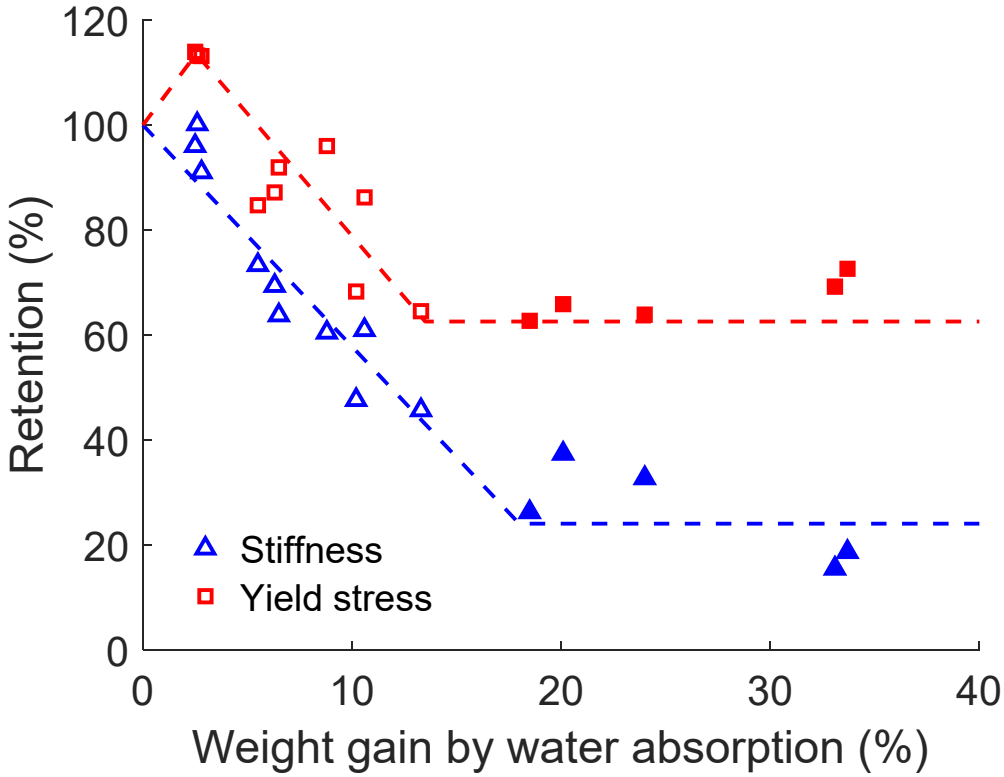

Figure 3.8: Stiffness and yield stress retentions vs. weight gain for 225°C 1 day degradation, tested under room temperature compression. Weight gain is defined as $\frac{w_{wet}-w_{dry}}{w_{dry}}\times 100\%$, where w_{dry} and w_{wet} are the sample's dry and wet weights. The solid symbols represent the fully saturated situations. The dashed lines simply indicate the trends; they are not fits to the data.

3.3.1.5 Sample weight and dimension changes

The samples' weight gain $\frac{w_{wet}-w_{dry}}{w_{dry}}$ was recorded following the moisture degradation. Below 100°C, the maximum amount of water that HFPE-II-52 polyimide can absorb is 3.2% [70]. However, a higher amount of weight gain is found for polyimide under saturated steam pressure at higher temperatures. Results are shown in Figure 3.9 as weight gain vs. degradation time at

temperatures ranging from 200 to 250ºC. Generally, more water is absorbed by the samples at higher temperatures and for longer exposure times. At temperatures ≤ 205ºC, 3-5% of water saturation is recorded, with one exception (200ºC, 9 weeks). Starting from 215ºC, the polyimide samples take up as much as 30-60% water by weight. It is noted that the weight gains at relatively high temperatures and/or long durations have large variations. Some of the variation in weight gain may arise from the test method. At the higher temperatures, the samples were highly damaged due to hydrolytic degradation, see Figure 3.2. The surfaces of some samples adhered to the stainless-steel mesh in the pressure tube, and in some cases samples adhered to each other transferring mass from one sample to another, both of which may cause errors in mass measurement.

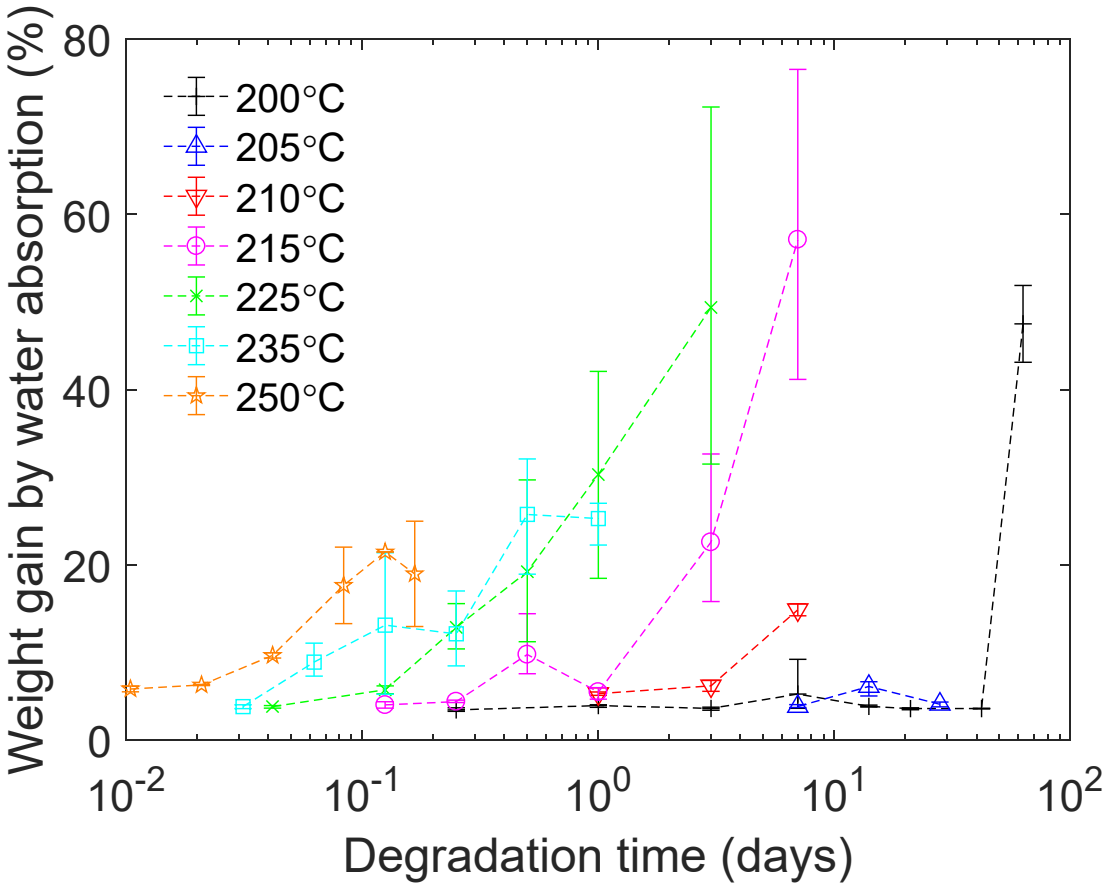

Figure 3.9: Sample weight gain as a function of degradation time (in log scale) and temperature. The error bars indicate the maximum and minimum of weight gains for each specific data point.

Along with the large weight gain, swelling strains as large as 20% are observed. (Measured with a caliper and estimated by taking the average of the swelling strains at different positions). The swelling strains do not recover after the samples are dried indicating a permanent deformation of the polyimide. Define a volume ratio r, as ($r = \frac{\Delta V_p}{\Delta V_w} = \frac{\Delta V_p}{\Delta m/\rho}$) where ΔV_p is the change of polymer volume, ΔV_w is the volume of absorbed water, Δm is the mass of absorbed water, and ρ is the density of the water at each specific temperature. When $r < 1$ the polymer expands by less than the volume of the absorbed water. When $r > 1$ the polymer expands by more than the volume of

the absorbed water. To put the swelling strains in context, Figure 3.10 plots the volume ratio as a function of degradation time for three different temperatures. The volume ratio starts below 1 then increases with time to greater than 1. These results suggest that the water starts by occupying the pre-existing polymer free volume, but then helps create space as the inner structure of the polyimide is damaged by hydrolytic degradation.

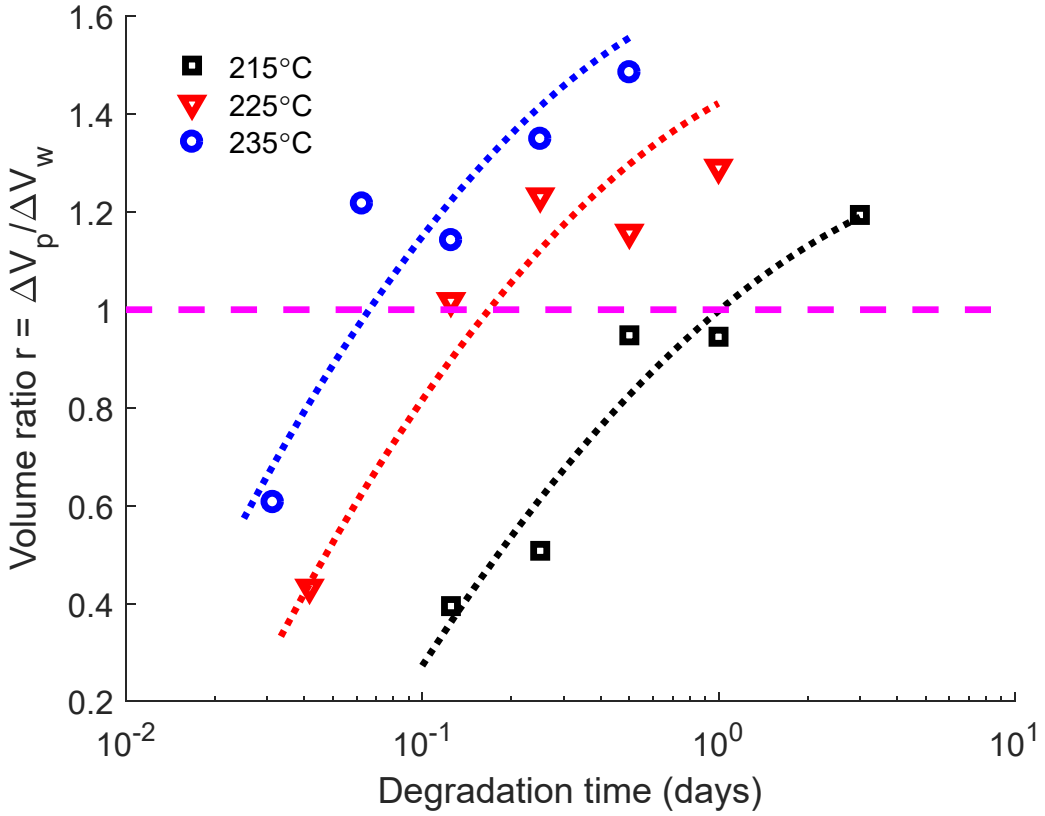

Figure 3.10: Volume ratio ($r = \frac{\Delta V_p}{\Delta V_w}$, where ΔV_p is the change of polymer volume, ΔV_w is the volume of absorbed water) vs. degradation time (in log scale) for selected temperatures. The dashed lines are for visualization only and do not represent fits to the data.

3.3.2 Plasticization

Figures 3.11 - 3.12 show the mechanical reductions due to plasticization as a function of moisture

level for temperatures of 100 to 225ºC. The baseline for the mechanical property reductions at a given temperature are the corresponding properties of a dry sample tested at that temperature. In the plots, the moisture level is approximated as $\frac{G_1+G_2}{2}$, as discussed in *Section 3.2.3*. Despite the great deal of scatter, the stiffness retention data show clear reductions (up to 25%) for wet samples at temperatures ≥175ºC. The yield stress, on the other hand, starts to drop for the wet samples across the whole range of testing temperatures. Generally, the larger the moisture amount and the higher the temperature, the greater the reductions of mechanical properties. The experimental results indicate that besides the chemical degradation that is history dependent, moisture also has an instantaneous plasticization effect that can reduce both the stiffness and strength of HFPE-II-52 polyimide. Considering that all samples start fully saturated and that the samples that have dried out for longer time (thus have less moisture levels) are stiffer and stronger than the wet samples, the plasticization effect is proved to be reversible.

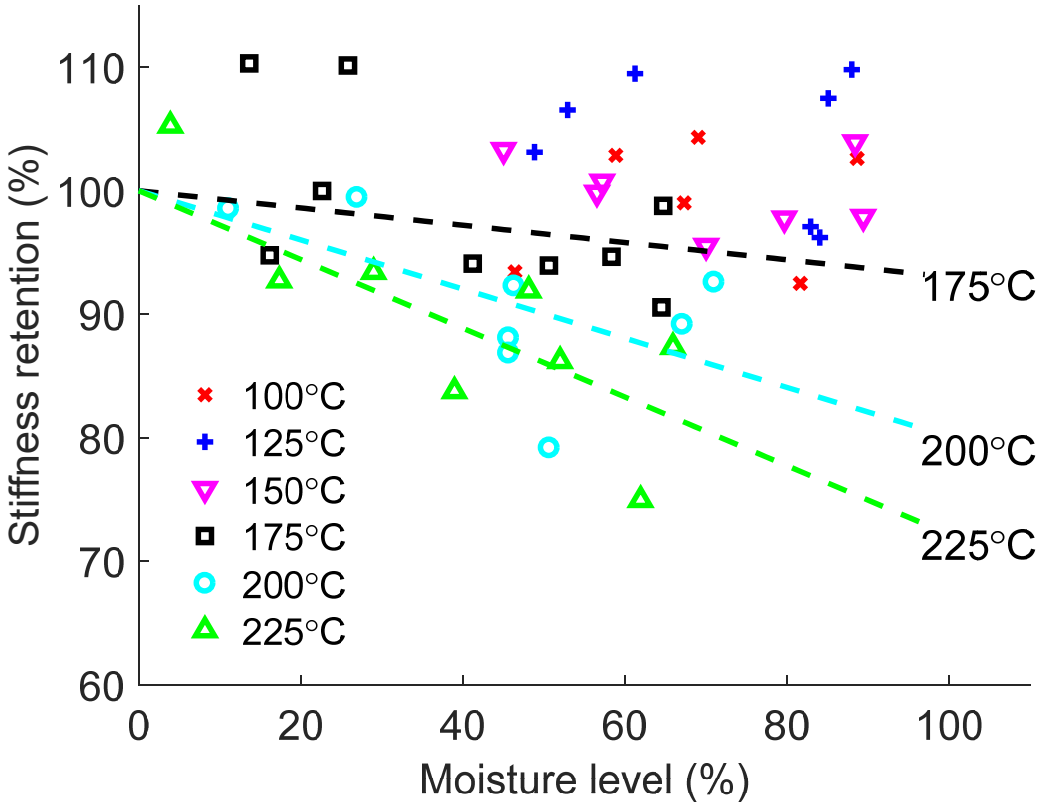

Figure 3.11: Plasticization -- stiffness retention vs. moisture level $G(t) \equiv \frac{w(t)-w_0}{w_{max}-w_0}$ for different temperatures. Dashed lines are the linear model fits for selected temperatures.

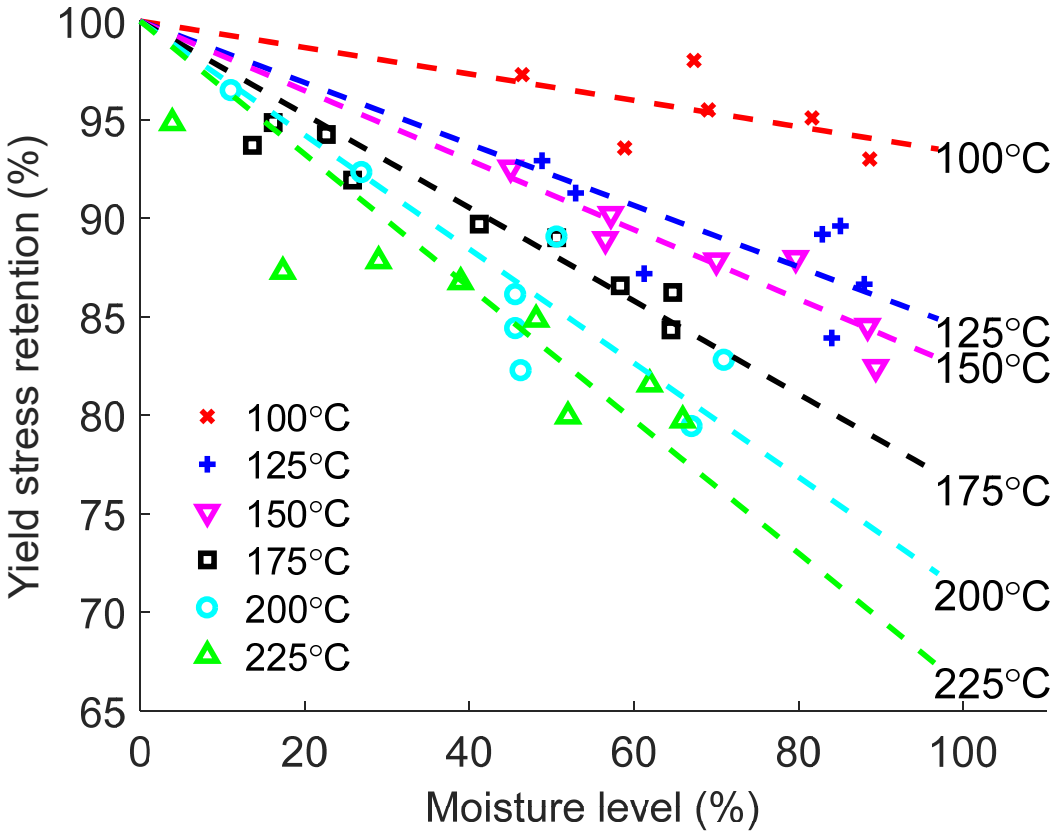

Figure 3.12: Plasticization – yield stress retention vs. moisture level $G(t) \equiv \frac{w(t)-w_0}{w_{max}-w_0}$ for different temperatures. Dashed lines are the linear model fits.

3.4 Modeling and Parameter Identification

3.4.1 Modeling of hydrolytic degradation and plasticization

From the above experimental results, the moisture will have both a permanent, history dependent effect (hydrolytic degradation) and a reversible, instantaneous effect (plasticization) on the mechanical properties of HFPE-II-52 polyimide. Those two effects will be modeled separately in this section.

For hydrolytic degradation, we start with the n^{th} order kinetics of the chemical reaction,

adapted from Deiasi [24] as

$$-\frac{dx_h}{dt} = K(\theta, \phi)x_h^n, \tag{3.1}$$

where x_h is the retention of the hydrolysable bonds ($0 \leq x_h \leq 1$), t is time, and $K(\theta, \phi)$ is a rate constant that depends on the temperature, $\theta(x, y, z, t)$, and the moisture concentration, $\phi(x, y, z, t)$, ($0 \leq \phi \leq 1$). Define λ to be the ratio of a property (stiffness or strength) to its value for an undamaged, or virgin, sample. We assume linear mapping from the retention of hydrolysable bonds x_h to the retention of the mechanical properties λ, and obtain

$$-\frac{d\lambda}{dt} = K(\theta, \phi)(\lambda - \lambda_\infty)^n. \tag{3.2}$$

When $x_h = 1$, $\lambda = 1$, and when $x_h = 0$, $\lambda = \lambda_\infty$. The effects of temperature θ and moisture concentration ϕ in the rate constant $K(\theta, \phi)$ are assumed to be separable. Assuming linear moisture dependence, we obtain

$$K(\theta, \phi) = \phi k(\theta). \tag{3.3}$$

$k(\theta)$ is modeled in the Arrhenius form as

$$k(\theta) = A_h \exp(-Q_h/k_B\theta), \tag{3.4}$$

where A_h is the pre-exponential factor, Q_h is the activation energy and $k_B = 1.3806\times10^{-23}$ $(J \cdot K^{-1})$ is the Boltzmann constant.

For plasticization, a simple linear modeling approach is used, thus the mechanical property retention due to plasticization $\alpha(\theta, \phi)$ is taken to be

$$\alpha(\theta, \phi) = \max\{1 - H(\theta)\phi, 0\}, \tag{3.5}$$

where $H(\theta) \geq 0$ is a function of temperature, which is also modeled linearly as

$$H(\theta) = \max\{a\theta + b, 0\}, \tag{3.6}$$

where a and b are parameters to be determined. Note that in the plasticization experiments, the average (over the sample) mechanical reductions are measured as a function of the normalized

moisture level $G(t) \equiv \frac{w(t)-w_0}{w_{max}-w_0} = \frac{\int_V \phi(x,y,z,t)dV}{V}$, where V is the sample volume. The moisture concentration ϕ is nonuniform and hence the retention factor $\alpha(\theta, \phi)$ is obtained in an average sense. Appendix 3B provides an analysis of the effect of the nonuniformity of the moisture concentration on the retention factor, and estimates the level of error incurred by the averaging assumptions.

For applications involving both permanent and instantaneous moisture degradation, the retention of mechanical properties is assumed to be the product of the two retention factors $\lambda(\theta, \phi) \cdot \alpha(\theta, \phi)$.

3.4.2 Parameter identification for hydrolytic degradation

Equations (3.2) - (3.4) describe the mechanical reductions due to the hydrolytic degradation. The parameters to be determined are λ_∞, n, A_h and Q_h. Four sets of $\{\lambda_\infty, n, A_h, Q_h\}$, one for each of the room temperature and high temperature stiffness and strength retentions are fit to the data shown in Figures 3.4 – 3.7. Note that in theory, only one set of n, A_h and Q_h exists going from equation (3.1), because the fraction of remaining hydrolysable bonds is determined once the samples are taken out from the pressure tube before the compression tests. However, the mapping from the retention of hydrolysable bonds x_h to the retentions of mechanical properties λ can be more complicated than linear. Thus, to obtain a more accurate model, the parameter set $\{\lambda_\infty, n, A_h, Q_h\}$ is fit separately for room/high temperature compressions and for stiffness/strength retentions. In an application of these models the analyst can choose which set to use based on the temperatures to be considered. For both room and high temperature compression tests, only three temperatures 215, 225 and 235°C were used for parameter identification. For lower temperatures, the rate of degradation is much slower and the model does not apply. For higher temperature,

250°C, the results are considered as less accurate, because the data were obtained within a short time frame, comparable to the time required to achieve thermal equilibrium.

To obtain the parameters, note that in Figures 3.4 and 3.6, the stiffness retentions drop to zero while the strength retentions shown in Figures 3.5 and 3.7 do not drop below 0.4. Therefore, λ_∞ is taken to be $\lambda_\infty = 0$ for stiffness retentions and $\lambda_\infty = 0.4$ for yield stress retentions, for both room temperature and high temperature compressions. Next, to determine the reaction order n, we first fit n as a separate variable together with the rate constant $k(\theta)$ for each temperature in equations (3.2) - (3.3). The values of n in different cases ranged from 1 to 3 and were close to 2 on average. To keep n as an integer and for simplicity, $n = 2$ is used for all cases, consistent with the results of Deiasi [24]. What is left to determine are A_h and Q_h in equation (3.4). We first solve for the rate constant $k(\theta)$ in equations (3.2) - (3.3). With $n = 2$ and for the case $\phi = 1$, we get

$$k(\theta) = \frac{1}{t}\left[\frac{1}{\lambda - \lambda_\infty} - \frac{1}{1 - \lambda_\infty}\right]. \tag{3.7}$$

With the data presented in Figures 3.4 - 3.7, we obtain three $k(\theta)$ for temperatures 215, 225 and 235°C (different for 4 different cases). We then rewrite equation (3.4) as

$$\ln\big(k(\theta)\big) = \ln(A_h) - \frac{Q_h}{k_B \theta}, \tag{3.8}$$

and fit $\ln(A_h)$ and Q_h with linear least squares. The resulting parameters for the hydrolytic degradation model are summarized in Table 3.3.

Table 3.3: Parameters for hydrolytic degradation (RT: room temperature 20°C; HT: high temperature 285°C)

Data source	$A_h\ (s^{-1})$	$Q_h\ (J)$	λ_∞	n
RT stiffness	7.29×10^{21}	4.18×10^{-19}	0	2
RT yield stress	4.78×10^{19}	3.85×10^{-19}	0.4	2
HT stiffness	3.09×10^{19}	3.82×10^{-19}	0	2
HT yield stress	1.14×10^{22}	4.23×10^{-19}	0.4	2

Figures 3.4 – 3.7 show the model fits along with the experimental data. Although only the 215-235°C data are used for the fits, the model aligns well with the 250°C data, suggesting that the model works well for higher temperatures. However, the rate of hydrolytic degradation at 200°C and 205°C is much slower for the experimental results than for the model predictions, indicating that the model is no longer valid at low temperatures. Thus the model is valid in a range of temperatures from 210°C to 250°C, and can be potentially extrapolated to higher temperatures. Effectively (at least for the 9-week degradation durations studied) there is a threshold temperature below which hydrolytic degradation is not observed. Above this temperature the degradation proceeds with rapidly increasing speed as the temperature increases.

As a sample application of the model, consider calculating an allowable safe time-temperature bound, outside which significant hydrolytic degradation would occur and would have a negative influence on the mechanical performance of HFPE-II-52 polyimide. As an example, if less than $20\%\times(1-\lambda_\infty)$ reduction is defined to be the safe criterion, that is 80% stiffness retention or 88% strength retention, using the above models, Figure 3.13 plots the temperature and time envelope that separates the safe and unsafe regions. Regions below the curve are by this criterion considered "safe". Note that at high temperatures significant degradation can occur in minutes.

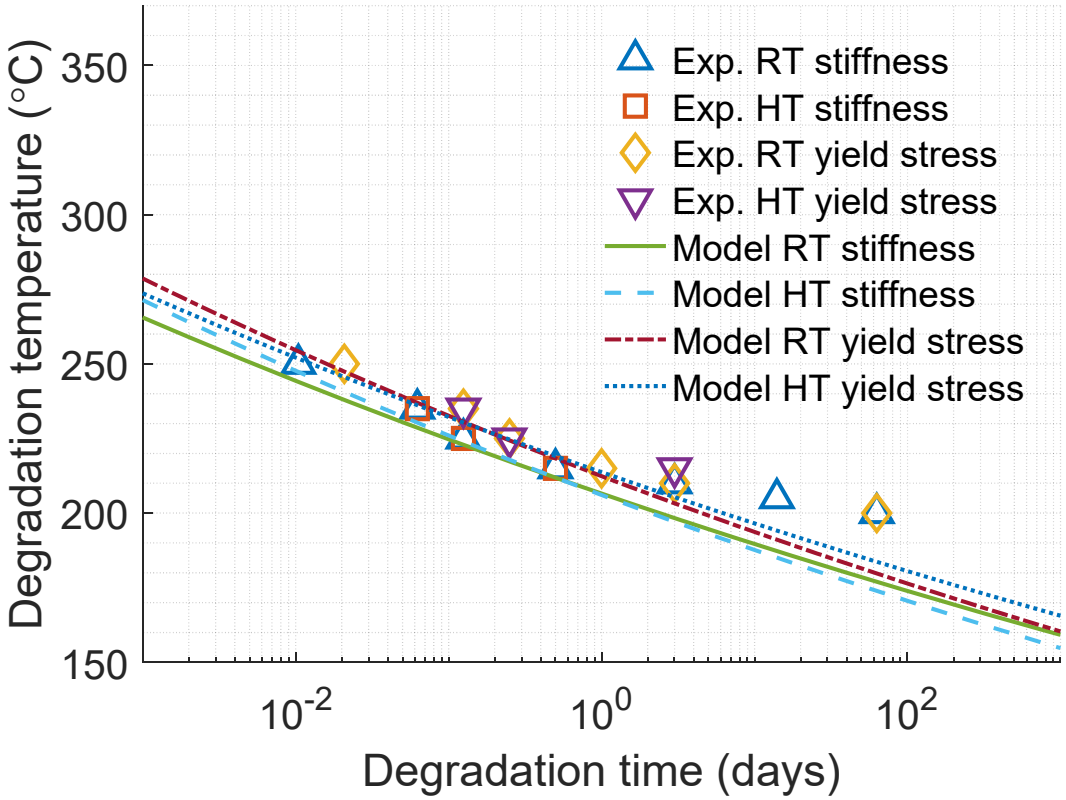

Figure 3.13: Time – temperature envelope for significant hydrolytic degradation (defined as $20\%\times(1-\lambda_\infty)$ reduction). RT: under room temperature compression; HT: under high temperature compression; Exp.: Experiments.

In equation (3.3), the rate of hydrolytic degradation is linear in the moisture level. However, Figure 3.8 suggests that the retention factor λ is approximately linear with the moisture level. Applying the linear rate model in equation (3.3) will yield a lower λ than the experimental observation shown in Figure 3.8, thus overestimating degradation. Given the limited data, additional experiments are needed to understand the moisture dependence of hydrolytic degradation in polyimides.

3.4.3 Parameter identification for plasticization

The data in Figures 3.11 - 3.12 are used to fit the linear equation (3.5) to obtain $H(\theta)$ for different temperatures ranging from 100 to 225ºC for both stiffness and yield stress retentions. Results of the fits are included in Figures 3.11 - 3.12. Next, $H(\theta)$ are plotted as a function of temperature as shown in Figure 3.14 ($H_E(\theta)$ for stiffness and $H_p(\theta)$ for yield stress). Parameters a and b are then obtained with a linear fit and are listed in Table 3.4. The highest temperature tested in the plasticization experiments was 225ºC due to the difficulty of holding enough moisture inside the sample for the time it takes to perform the compression test. The good linear fit of $H(\theta)$ for both stiffness and yield stress suggests that the linear model may possibly be extrapolated to higher temperatures.

Table 3.4: Parameters for plasticization

	a (1/°C)	b
Stiffness	3.81×10^{-3}	-0.576
Yield stress	2.07×10^{-3}	-0.126

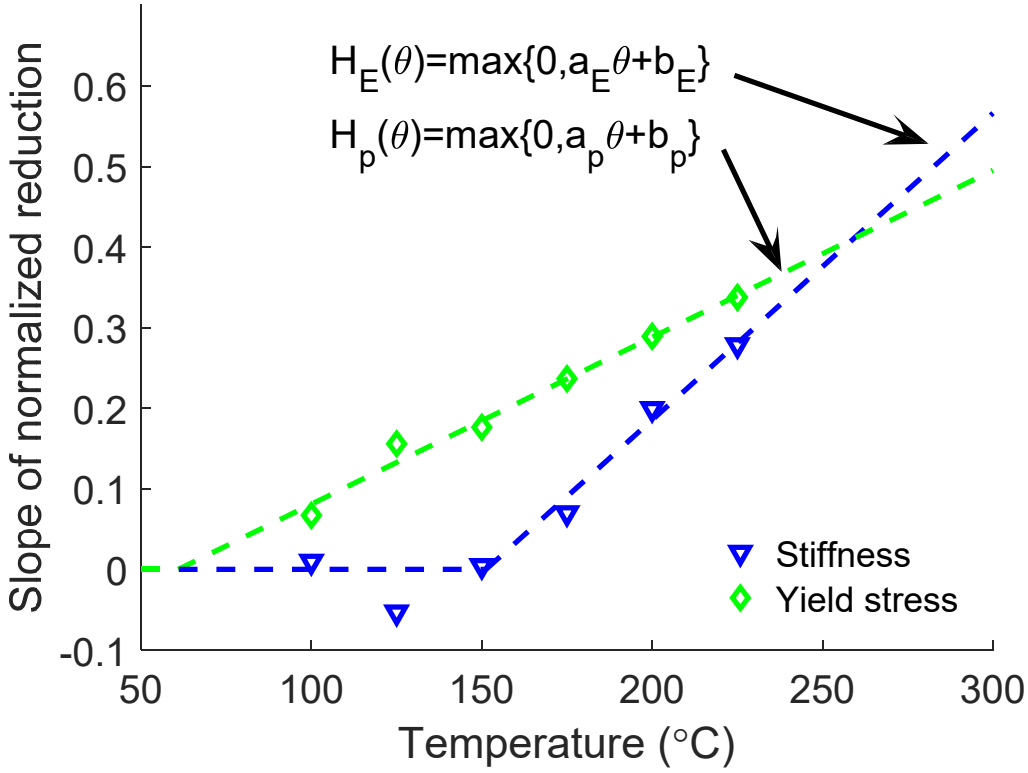

Figure 3.14: Slope $H(\theta)$ vs. temperature for stiffness and yield stress. Dashed lines are the model fittings.

3.5 Other Experiments on Moisture Degradation

3.5.1 3-point bending at elevated temperature for plasticization

In previous sections (*Section 3.2.3, 3.3.2 and 3.4.3*), plasticization effect on the mechanical properties of HFPE-II-52 polyimide is quantified by conducting compression tests on the moisture saturated samples at elevated temperatures. In this section, additional results on the effect of plasticization are presented. 3-point bending tests are conducted at 185°C and the material initial stiffness and yield stress for both wet and dry samples are measured and compared. The results are not used for model fitting, but used solely as an alternative experimental observation under a

different loading type for the instantaneous and reversible moisture effects of HFPE-II-52 polyimide at elevated temperature.

3.5.1.1 Experimental procedure

The samples used for 3-point bending were prepared in the same way as described in *Section 3.2.1.1*, except that the sample dimensions are $62\times4\times2$ mm. Wet samples were conditioned using a laboratory humidity chamber (Associated Environmental System, Model LH-1.5) at 70°C for 3 days. As with the experiments for plasticization with compression tests, no permanent damage (hydrolytic degradation) will occur during the moisture saturation at low temperature (70°C for 3 days).

The 3-point bending tests were performed using TA Q800, a Dynamic Mechanical Analysis (DMA) testing system. Unlike the MTS with the clamshell furnace used for the compression tests, the furnace of the TA Q800 may only be opened at room temperature, so the pre-heating procedure (S*ection 3.2.3*) used for the compression tests are not possible for the 3-point bending testing. Therefore, the furnace heating rate was set to its maximum (actual heating rate around 150°C/min) to minimize the moisture loss of the wet samples before testing. After ramping up the temperature to 185°C, the temperature in the furnace was set to hold constant for another 2 minutes to reach thermal equilibrium. Since the TA Q800 can only guarantee uniform temperature in the furnace with a heating rate no larger than 20°C/min, careful temperature measurements and heat transfer analysis were conducted and described in Appendix 3C to estimate the sample temperatures during the 3-point bending tests.

The samples were loaded under force control until 12N, with a loading rate of 18N/min. 8 samples were tested (4 dry and 4 wet) with the same thermal and loading history. The samples

were weighed before and after the tests for moisture level estimations during the 3-point bend loading. In the end, material initial stiffness and yield stress for the dry and wet samples were calculated and compared to probe the mechanical property reductions of HFPE-II-52 polyimide due to plasticization under 3-point bending tests.

3.5.1.2 Results

The sample mid-plane deflection vs. force curves are obtained for 4 dry samples and 4 wet samples. The maximum bending stress can be derived from the applied force P_0. Before reaching to the yield point, and assuming linear elasticity, the bending stress in the mid-plane is linearly distributed, with the maximum bending stress σ_0 calculated as

$$\sigma_0 = \frac{M(h/2)}{I} = \frac{3P_0L}{2wh^2}, \tag{3.9}$$

where M is the bending moment, $I = \frac{1}{12}wh^3$ is the cross-sectional moment of inertia, h and w are the height and width of the sample, respectively, and L is the length of the support span, which is 50mm for all tests. The normal maximum strain ε_0 in the sample mid-plane is obtained through the measured mid-plane deflection, Δ_0 ($\Delta_0 = \frac{P_0L^3}{48EI}$) as

$$\varepsilon_0 = \frac{\sigma_0}{E} = \frac{6\Delta_0 h}{L^2}, \tag{3.10}$$

where E is the material stiffness. With equations (3.9) - (3.10), the maximum bending stress vs. bending strain is plotted for both the wet and dry samples, as shown in Figure 3.15. Note that out of the linear zone, the values of stress and strain are not real; they are plotted solely to empirically determine the yield stress.

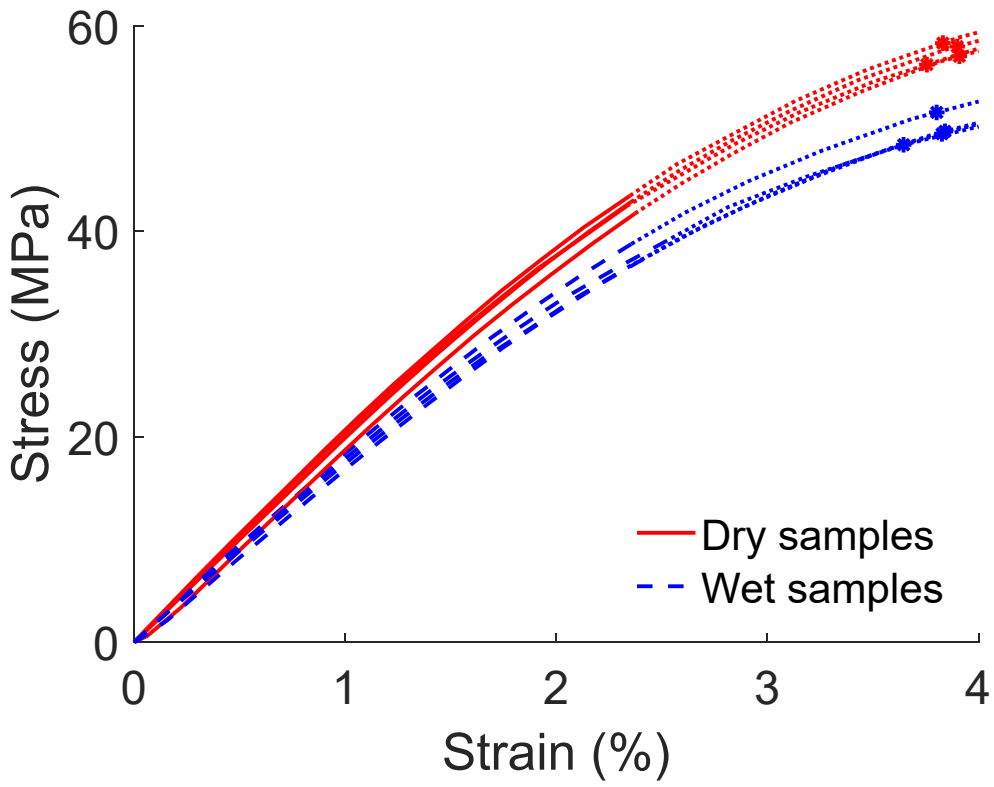

Figure 3.15: Bending maximum stress vs. strain for 4 dry samples and 4 wet samples. Dotted lines indicate that the stress and strain values are not real outside the material linear zone. Asterisks indicate the yield stresses determined by the empirical 1% strain offset. Testing temperature is 185ºC. Wet samples' moisture level right before loading is estimated to be $G \equiv \frac{w-w_0}{w_{max}-w_0} = \frac{\int_V \phi(x,y,z)dV}{V} = 59\%$.

It is observed that both the material initial stiffness and yield strength are reduced for the wet samples. Quantitatively, the initial stiffness has an average reduction of 11.0%, and the yield stress, determined by the empirical 1% offset method, reduces 13.2% compared to the dry ones.

Although the heating process for all 8 samples are controlled to be as close as possible, the temperatures inside the DMA during loading could have a variation due to the high heating rate.

The average air temperatures while loading the samples are 185ºC on average, with a standard deviation of 6ºC. The sample temperature can be assumed uniformly distributed, and is close to the air temperature (see analysis in Appendix 3C).

To estimate the moisture level, the wet samples were weighed before and after the bending tests. The normalized moisture level $G \equiv \frac{w-w_0}{w_{max}-w_0}$ for the 4 wet samples after the tests are $(52 \pm 2)\%$. The wet samples' moisture level right before the test should be larger than 52%, because of the additional moisture loss during the tests and the cooling process. To perform a finer estimation of the moisture level, a finite difference program is used to solve the moisture diffusion equation:

$$\frac{\partial \phi}{\partial t} = \nabla \cdot (D \nabla \phi), \tag{3.11}$$

where $\phi(x, y, z, t)$ is the moisture concentration, and the moisture diffusivity D for HFPE-II-52 polyimide is temperature dependent, and is estimated as [70]:

$$D = D_0 \exp(-E_a / k_B \theta), \tag{3.12}$$

where θ is the temperature, and D_0 and E_a are known material parameters with $D_0 = 9.0\ mm^2/s$ and $E_a = 37.0\ kJ/mol$ [70]. With the known thermal history during heating (see Appendix 3C), $\phi(x, y, z)$ at the time right before applying the force can be calculated with the finite difference code. The result of the normalized moisture level $G \equiv \frac{w-w_0}{w_{max}-w_0} = \frac{\int_V \phi(x,y,z) dV}{V}$ is determined to be 59%. Note that the moisture concentration is not uniformly distributed within the sample, the results are obtained only in an average sense.

Note that in *Section 3.4.3*, model parameters are identified based on the compression test data. Based on the model, at 185ºC and with an average moisture level 59%, the stiffness and yield stress reductions are 7.6% and 15.2%, respectively, which is reasonably close to what have been observed in the 3-point bending tests (11.0% and 13.2% reductions on initial stiffness and yield

stress, respectively).

3.5.2 FTIR for hydrolytic degradation

The rate and temperature dependent, permanent moisture degradation was observed with the moisture conditioning -- compression testing experiments described in *Sections 3.2.2* and *Section 3.3.1*. A model was developed in *Section 3.4.1* to quantify the mechanical property reductions of HFPE-II-52 polyimide after moisture treatment. The hypothesis of the mechanism is hydrolytic degradation, where imide bond breaks due to water reaction. Here the Fourier transform infrared spectroscopy (FTIR) characterization was conducted to see whether an evidence of the microstructure change can be observed after the sample was degraded in the humid environment. We compared the spectra of a moisture treated sample (under 225ºC for 7 days) with an undegraded sample. The surface of the degraded sample was made flat and parallel with 100 grit paper before the FTIR characterization. The Attenuated Total Reflectance (ATR) mode was used and the relative absorbance vs. wavenumber was plotted.

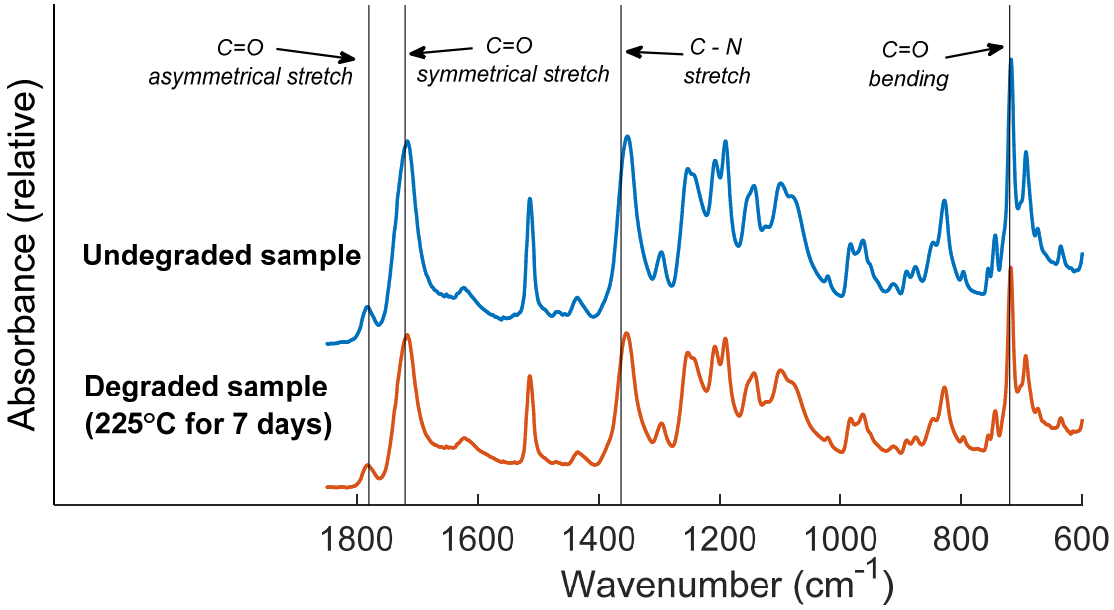

Figure 3.16: FTIR measurements for undegraded and degraded samples

As shown in Figure 3.16, all the characteristic absorption peaks that represent aromatic imide groups [30] remain to exist after moisture treatment, and no significant reductions of the peak relative intensities are observed, either. Deiasi mentioned that the ratio of the hydrolysable groups to the imide groups is only about 0.6% for the Kapton polyimide [24], so that may be why no spectra difference can be observed for the sample after hydrolytic degradation. Considering that the material mechanical properties greatly reduce for sample that is treated under 225ºC for 7 days (initial stiffness reduces to below 10% compared to the normal sample), it remains a question on what happens microstructurally during the moisture degradation. Future work may include measuring the molecular weight of the samples before and after the moisture degradation.

3.6 Summary and Conclusions

Experiments were designed and performed to investigate moisture degradation and its effects on

the mechanical properties of HFPE-II-52 polyimide. Two different mechanisms – hydrolytic degradation and plasticization are considered. For hydrolytic degradation, the experimental data are used to develop a time, temperature and moisture dependent kinetic model of degradation of stiffness and yield strength. The model is valid over a temperature range of 210 - 250ºC and potentially can be extended to higher temperatures. The results show that above 210ºC hydrolytic degradation occurs with increasing speed as the temperature is increased. Extrapolating the model to temperatures above 250ºC significant degradation is calculated to occur in a time scale of just minutes. In addition, a large amount of water absorption and swelling occur during hydrolytic degradation. This surprising result, combined with the large scatter in the data point to a need for additional experimentation to better quantify the behavior. Another interesting result is that moisture combined with moderate heating of approximately 200ºC appears to facilitate additional cross linking thus strengthening the polyimide. For plasticization, stiffness and yield strength reductions are measured as functions of temperature and moisture concentration up to 225ºC. A temperature and moisture dependent linear model is developed and fit to the experimental data. The results show that the mechanical effects of plasticization can be significant starting as low as 100ºC, well below the temperature for onset of hydrolytic degradation. Overall, the data and models provide a means to predict both the permanent, history dependent and the reversible, instantaneous moisture effects on the mechanical performance of thermosetting polyimides and other high temperature polymers. In *Chapter 4,* the moisture degradation model will be combined into the viscoelastic and viscoplastic constitutive equations that are developed in *Chapter 2*. The combined model will be applied in a finite element context to study the hygrothermal failures of polyimides and/or polyimide laminates.

Appendix 3A Estimation of Moisture Level During Plasticization Experiments

The moisture level during the plasticization experiments varies during the tests. The final normalized moisture level G_2 is directly measured, however the moisture level, G_1 at the start of loading must be estimated. To do so we begin with Fick's law:

$$\frac{\partial \phi}{\partial t} = D\left(\frac{\partial^2 \phi}{\partial x^2} + \frac{\partial^2 \phi}{\partial y^2} + \frac{\partial^2 \phi}{\partial z^2}\right), \tag{3.13}$$

where $\phi(x, y, z, t)$ is the moisture concentration of the polyimide sample, x, y and z are the spatial coordinates, t is time, and D is diffusivity. The diffusivity depends on temperature as

$$D(\theta) = D_0 \exp(-E_a/k_B\theta), \tag{3.14}$$

where θ is the temperature. Parameters D_0 and E_a are $D_0 = 9.0\ mm^2/s$ and $E_a = 37.0\ kJ/mol$ [70]. Samples start with full saturation. The ambient RH can be approximated as 0. Therefore, for a cube shaped sample with dimensions (a, b, c), we have initial conditions

$$\phi = 1 \text{ at } t = 0 \text{ for } 0 < x < a; 0 < y < b; 0 < z < c. \tag{3.15}$$

and boundary conditions

$$\phi = 0 \text{ at } t > 0 \text{ for } x = 0, a; y = 0, b; z = 0, c. \tag{3.16}$$

For a constant temperature θ, and hence constant D, the analytical solution can be obtained in a series form [70] as

$$\begin{aligned}\phi(x, y, z, t) = &\left[\frac{4}{\pi}\sum_{n=1,3\ldots}^{\infty}\frac{1}{n} sin\left(\frac{n\pi x}{a}\right) exp\left(\frac{-Dn^2\pi^2 t}{a^2}\right)\right] \\ &\left[\frac{4}{\pi}\sum_{n=1,3\ldots}^{\infty}\frac{1}{n} sin\left(\frac{n\pi y}{b}\right) exp\left(\frac{-Dn^2\pi^2 t}{b^2}\right)\right] \\ &\left[\frac{4}{\pi}\sum_{n=1,3\ldots}^{\infty}\frac{1}{n} sin\left(\frac{n\pi z}{c}\right) exp\left(\frac{-Dn^2\pi^2 t}{c^2}\right)\right].\end{aligned} \tag{3.17}$$

Integration of equation (3.17) over the sample volume and dividing the result by the total volume gives the normalized moisture level

$$G(t) = \frac{w(t)-w_0}{w_{max}-w_0} =$$

$$\left[\frac{8}{\pi^2}\sum_{n=1,3\ldots}^{\infty}\frac{1}{n^2}exp\left(\frac{-Dn^2\pi^2t}{a^2}\right)\right]\left[\frac{8}{\pi^2}\sum_{n=1,3\ldots}^{\infty}\frac{1}{n^2}exp\left(\frac{-Dn^2\pi^2t}{b^2}\right)\right]\left[\frac{8}{\pi^2}\sum_{n=1,3\ldots}^{\infty}\frac{1}{n^2}exp\left(\frac{-Dn^2\pi^2t}{c^2}\right)\right]. \quad (3.18)$$

The goal is to estimate $G_1 = \frac{w_1-w_0}{w_{max}-w_0}$ based on the measured $G_2 = \frac{w_2-w_0}{w_{max}-w_0}$. Recall that the sample starts fully saturated, or $G_0 = 1$. Then the sample is tested starting at a time t_1 which includes the time to heat up the sample and to hold it at temperature for varying lengths of time. The test lasts for a duration t_2 at a constant temperature θ, right after which the sample is weighed to obtain G_2. The additional weight loss after t_2 can be ignored since the cooling time is short and the diffusivity is low at room temperature. G_1 cannot be directly calculated from equation (3.18) using t_1 since it takes time to reach thermal equilibrium and the temperature dependent diffusivity D is not constant during this stage. To estimate G_1 we introduce a fictitious time, t_1^*, such that $G(t_1^*) = G_1 = \frac{w_1-w_0}{w_{max}-w_0}$ calculated for a constant temperature θ equal to the test temperature. G_2 then equals $G(t_1^* + t_2) = \frac{w_2-w_0}{w_{max}-w_0}$. We first solve for $t_1^* + t_2$ numerically using the measured value of G_2 and inverting equation (3.18). Since t_2 is known, t_1^* can be determined. Then $G_1 = G(t_1^*)$ can be determined by the forward application of equation (3.18). The moisture level of the sample during the compression test is bounded by G_1 and G_2, and is approximated as their mean.

Appendix 3B Effect of Nonuniform Moisture on Plasticization Results

During the plasticization tests, moisture diffusion results in a nonuniform moisture concentration $\phi(x, y, z)$ in the sample and thus in a nonuniform retention factor $\alpha(x, y, z)$. However, the data are analyzed based on the average moisture concentration and treating the retention factors as uniform. In the analysis below the error in retention factor that is induced by ignoring the non-

uniformity in $\alpha(x, y, z)$ is estimated.

A cube shaped sample with dimensions (a, b, c), sitting in coordinates (x, y, z), is loaded in compression in z direction. Initially in the elastic zone, the stiffness retention $\alpha(x, y, z)$ together with the virgin stiffness E relates the normal stress σ and the normal strain ε as

$$\sigma(x, y, z) = \alpha(x, y, z)E\varepsilon(z). \tag{3.19}$$

Note that assumption can be made that the normal strain is uniform in every $x - y$ plane ($\varepsilon(x, y, z) = \varepsilon(z)$). From stress equilibrium,

$$\frac{\iint \sigma(x,y,z)dxdy}{ab} = \sigma_0\,, \tag{3.20}$$

where σ_0 , the average stress in every $x - y$ plane is a constant. The factor $\alpha(x, y, z)$ cannot be measured directly from equation (3.18), but can be measured in an average sense from:

$$\sigma_0 = \bar{\alpha}E\frac{\int \varepsilon(z)dz}{c}, \tag{3.21}$$

where $\frac{\int \varepsilon(z)dz}{c}$ is the average strain measured in the compression tests. Integrating equation (3.19) through the $x - y$ plane, we get

$$\frac{\iint \sigma(x,y,z)dxdy}{ab} = \frac{\iint \alpha(x,y,z)dxdy}{ab}E\varepsilon(z). \tag{3.22}$$

With equations (3.20) - (3.22), we obtain the relationship between $\bar{\alpha}$ and $\alpha(x, y, z)$ as

$$\bar{\alpha} = \frac{c}{ab\int \frac{dz}{\iint \alpha(x,y,z)dxdy}}. \tag{3.23}$$

The average retention factor $\bar{\alpha}$ is the quantity directly measured in the experiments.

In the interpretation of the experimental data the sample moisture level is the volume average $G = \frac{\iiint \phi(x,y,z)dxdydz}{abc}$. Thus, to compare the error incurred in α due to treating the moisture distribution as if it was a constant, equal to the average compare $\bar{\alpha}$ calculated from equation (3.23) to α based on the average moisture level,

$$\bar{\alpha}^* = \max[1 - H(\theta)\frac{\iiint \phi(x,y,z)dxdydz}{abc}, 0]. \quad (3.24)$$

The moisture distribution $\phi(x,y,z)$ can be estimated from the diffusion equations (3.9) - (3.10), and $\alpha(x,y,z)$ is obtained by applying equations (3.5) - (3.6) but with spatially varying ϕ. Numerically integrating equations (3.23) - (3.24), $\bar{\alpha}$ and $\bar{\alpha}^*$ are compared to each other for all plasticization experiments. The maximum difference of the two methods is less than 0.5%, which occurs in the case of 225°C with the most moisture left in the sample. This analysis shows that the error incurred by attributing the reductions to the average moisture concentration is not significant.

Appendix 3C Temperature Estimations of the 3-Point-Bending Samples

To minimize the sample moisture loss during the 3-point bending test, the heating rate of the DMA furnace was set above its maximum rate 20°C/min which would guarantee a thermal equilibrium. Thus, the sample temperature may not fully reach to the controlled air temperature. Heat transfer analysis is then conducted here to analyze the actual temperature field of the bending sample during heating.

The governing heat transfer equation is given by

$$\frac{\partial \theta}{\partial t} = \nabla \cdot (C\nabla\theta), \quad (3.25)$$

with the convective boundary condition:

$$-\kappa\nabla\theta = h_c[\theta - \theta_{air}], \quad (3.26)$$

where $\theta = \theta(x,y,z,t)$ is the sample temperature, θ_{air} is the DMA furnace temperature, h_c is the convection coefficient, C is the thermal diffusivity, and κ is the thermal conductivity. The thermal diffusivity and thermal conductivity of HFPE-II-52 polyimide are known as $C = 0.16\ mm^2/s$ and $\kappa = 0.248\ W/(m \cdot {}^oC)$, respectively [34].

The goal is to obtain the relationship between the air temperature $\theta_{air}(t)$ and the sample

temperature $\theta(x, y, z, t)$. To do that, the convection coefficient h_c must first be estimated. As shown in Figure 3.17, a calibration was performed to estimate h_c. A K-type thermocouple is glued in between two half sized samples to measure the temperature in the center of the sample, while another thermocouple is placed near the sample to measure the air temperature. Temperatures from the thermocouples were recorded while the furnace was heated with the same heating rate as in the real experiments. Using equations (3.25) - (3.26), a finite difference code is used to iterate on h_c until the calculated temperature matches the measured temperature at the center of the sample. As a result, the convention coefficient h_c is obtained as $h_c = 52\ W/(m^2 \cdot {}^oC)$.

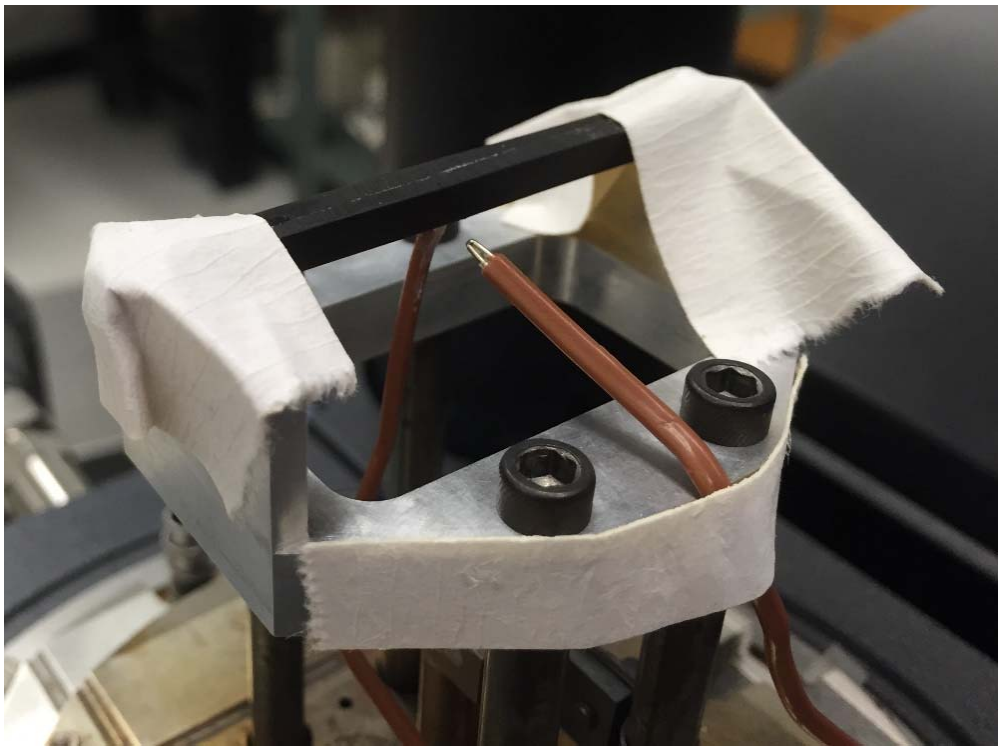

Figure 3.17: Experimental set-up to estimate the convection coefficient in the DMA

Once h_c is obtained, the sample temperature $\theta(x, y, z, t)$ can then be calculated with equations (3.25) - (3.26) with certain thermal history $\theta_{air}(t)$. It is found that with the heating rate 150ºC/min ramping from room temperature to 185ºC, and with a 2-minutes isothermal temperature holding

before loading, the temperature at the center of the sample is close of the air temperature (within 0.5°C), as illustrated in Figure 3.18.

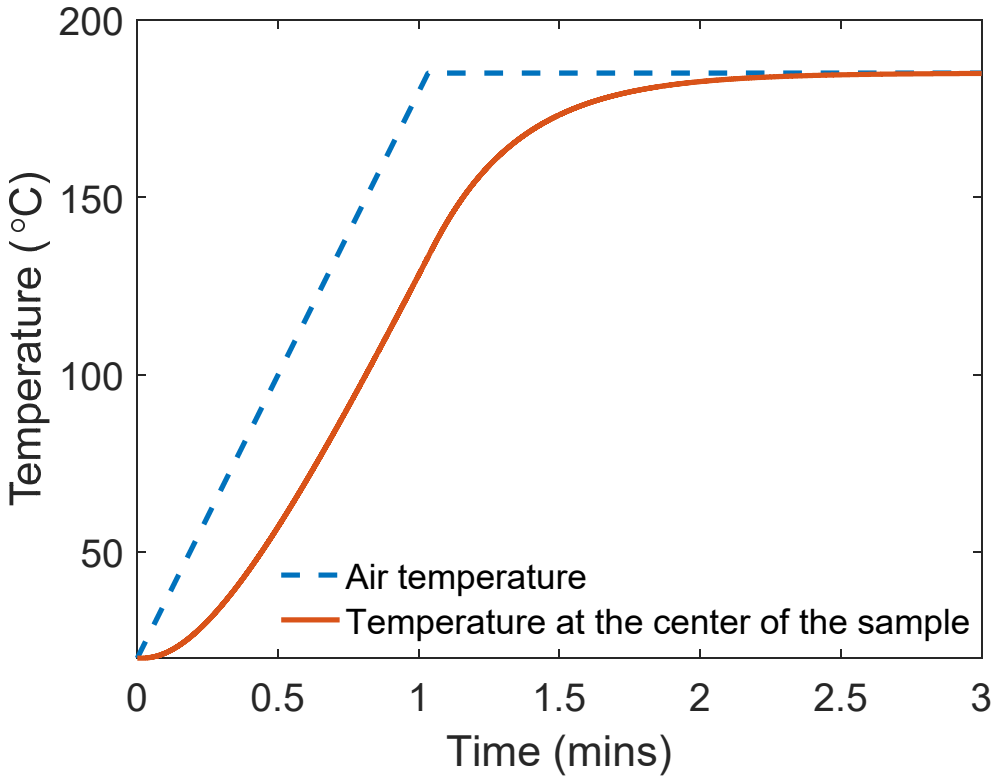

Figure 3.18: Comparison of DMA air temperature and the temperature at the center of the sample calculated from the finite difference code (150°C/min heating rate from 20°C to 185°C and then a 2-minutes holding)

CHAPTER 4

FINITE ELEMENT ANALYSIS OF BLISTERING

4.1 Introduction

Polyimides, a class of high temperature polymers, have found widespread applications ranging from thin films in electronic packaging to matrix materials in composites used for automotive or aerospace structures [1]–[3], [7]. Among those, a number of thermosetting polyimides, such as PMR-15 [13], PMR-II-50 [6] and AFRPE-4 [41] are particularly attractive as matrix materials for fiber reinforced composites to be used in weight critical systems under severe thermal conditions. These materials have high specific stiffness and strength, and exceptional thermal resistance with service temperatures above 300^{o}C.

A limiting factor for polyimide matrix composites (PiMCs) used in extreme temperature and moisture environments is hygrothermal failure by blistering and delamination [6], [36], [66]. When exposed to high humidity levels for extended times polyimides can absorb water from the environment, in an amount of 3-4% by weight for neat resins [34], [70] or 1-2% for the PiMCs [66], [68]. Under conditions of rapid heating relative to the structure's characteristic moisture diffusion time, moisture absorbed in the polyimide will vaporize and develop high internal vapor pressure. In the limit of a fully saturated resin under infinite heating rate this pressure will equal the saturation pressure of steam. For example, at 300^{o}C the saturation pressure is 8 MPa. These high pressures acting from within the polyimide resin or PiMC laminate can cause failure, essentially exploding the material from within, even in the absence of any external loading.

Steam pressure induced failures of polyimides and their composites have been studied by several groups in recent years [33]–[36]. Rice and Lee studied the blistering of AFR-700B

polyimide resins under rapid heating [36]. The samples were initially fully moisture saturated and the onset of the blistering was monitored by measuring the changes of the samples' thickness. Blistering is defined by rapid expansion of the material at less than the glass transition temperature. At the microscale a network of voids are formed in blistered material, transforming the resin into a high density foam. Czabaj et al. extended the work to study hygrothermal blistering and delamination of HFPE-II-52 polyimides and their composites [34], [35]. In their blistering studies this work mapped out the critical temperature-pressure envelope for blistering at different initial moisture levels and heating rates. In their delamination studies pre-existing interlaminar flaws were seen to fail by fracture due to the high vapor pressure developed in the flaws during rapid heating.

While the above experiments map out the conditions for hygrothermal failures, the underlying mechanisms of failure remain in question. One obvious mechanism is that moisture trapped inside any pre-existing defects such as voids or delaminations can vaporize and pressurize the adjacent material. The second is that the stiffness and yield strength of polyimides are greatly reduced at elevated temperatures [20], [22], [23], [31]. Thus the high stresses from vapor pressure combined with reduced stiffness and strength could lead to the unstable growth of voids or cavities.

However, this description of hygrothermal failure is incomplete and is missing a key element, namely both the reversible and permanent degradation of mechanical properties due to the presence of water in the resin at high temperatures. A number of studies show that absorbed moisture at high temperature will result not only in pressure loading, but can also lead to hydrolytic degradation and plasticization that weaken the material properties [6], [36], [66]. Hydrolytic degradation of polyimide is the result of water catalyzed bond breaking among and between polymer chains. Mechanically this results in permanent reductions in stiffness and strength that

depend on the thermal and moisture history. Hydrolytic degradation in polyimides has been studied by several scholars [24], [29], [66]. Plasticization is an instantaneous reduction of the stiffness and strength of a polymer due to absorbed water. The plasticizing effects of water on polyimides, or PiMCs at high temperature, have been observed in several studies [26], [68], [69]. In *Chapter 3* of this dissertation, the effects of hydrolytic degradation and plasticization on the mechanical behavior of the polyimide HFPE-II-52 were measured and modeled over a range of temperatures, time and moisture levels. Results of this study suggest that moisture degradation will be an important mechanism in failure by blistering.

In this chapter, the hypothesis that hydrolytic degradation and plasticization play an important role in blistering failure is tested through the use of finite element simulations that bring in effects of moisture as a source of mechanical loading and material softening. We first present the 3-D generalization of the constitutive model that combines the temperature dependent modeling of viscoelasticity and viscoplasticity (described in *Chapter 2*) with moisture effects due to hydrolysis and plasticization (described in *Chapter 3*). Using the material model, we build an axisymmetric finite element model of a void in an infinite medium to simulate the growth of a single void. Based on the onset of rapid void growth the critical temperatures of blistering for different moisture levels and heating rates are determined and compared to experimental data [34]. These simulations provide a computational alternative to experiments to map the conditions for the onset of blistering. More importantly, the simulations will show that the blistering of polyimides results from a combination of the effects of high temperature, vapor pressure, nonlinear material response, and most critically the hydrolytic degradation and plasticization induced by the absorbed moisture.

4.2 Summary of the Material Constitutive Model in 3D

In this section, we summarize the time, temperature and moisture dependent constitutive model, combining the studies of *Chapter 2* and *3*. The 3-D viscoelasticity and viscoplasticity constitutive equations are generalized from the 1-D version developed in *Chapter 2*. The model is then implemented as an ABAQUS user material, ready to be used in finite element analysis. A sample ABAQUS user material subroutine VUMAT coded in FORTRAN is included in Appendix 4D. To summarize, the model essentially captures four key features relevant to polyimides operated in high temperature and/or high humid environments:

(1) The time and temperature dependent material stiffness is modeled by linear viscoelasticity (equations (4.2) – (4.6));

(2) The nominal yield and the post yield behaviors are modeled by power law viscoplasticity with state variable evolution (equations (4.7) – (4.13));

(3) Moisture and temperature induced permanent damage (hydrolytic degradation) is modeled by temperature and moisture dependent chemical kinetics (equations (4.14) - (4.15));

(4) The effects of plasticization are instantaneous and reversible and depend linearly on temperature and moisture concentration (equations (4.16) - (4.17)).

The constitutive equations are presented with tensor index notation. We begin with the strain decomposition:

$$\varepsilon_{ij} = \varepsilon_{ij}^{e} + \varepsilon_{ij}^{p}, \tag{4.1}$$

where ε_{ij} is the total strain and ε_{ij}^{e} and ε_{ij}^{p} are the viscoelastic and viscoplastic strains, respectively. With standard linear viscoelasticity, the Cauchy stress σ_{ij} is related to the viscoelastic strain ε_{ij}^{e} by

$$\sigma_{ij} = \int_0^t 2G^*(\psi - \psi')\dot{e}_{ij}^{e}(t')dt' + \delta_{ij}K^* \int_0^t \dot{\varepsilon}_{kk}^{e}(t')dt', \tag{4.2}$$

where $e_{ij}^{e} \equiv \varepsilon_{ij}^{e} - \frac{1}{3}\varepsilon_{kk}^{e}\delta_{ij}$ is the deviatoric viscoelastic strain, ψ is the reduced time, and G^* and K^* are the material shear and bulk modulus, respectively. Using the principle of time temperature superposition, the reduced time ψ relates to the actual time t by

$$\psi = \int_0^t \frac{dt'}{A_\theta(\theta(t'))} \ , \tag{4.3}$$

where A_θ is the shift function, and θ is temperature. A common model for $A_\theta(\theta)$ is the WLF equation

$$log_{10}\big(A_\theta(\theta)\big) = -\frac{C_1(\theta-\theta_{ref})}{C_2+(\theta-\theta_{ref})}, \tag{4.4}$$

where θ_{ref} is the reference temperature, and C_1 and C_2 are parameters. The moduli G^* and K^* are defined as

$$G^*(\psi) = \lambda^{(1)}\alpha^{(1)}G(\psi) \ , \quad K^* = \lambda^{(1)}\alpha^{(1)}K, \tag{4.5}$$

where $\lambda^{(1)}$ and $\alpha^{(1)}$ are moisture degradation factors due to hydrolytic degradation and plasticization, respectively, and the moduli G and K are the dry values. Bulk moduli K is assumed to be time and temperature independent, and shear moduli G is generally fit with a Prony series

$$G(\psi(\theta,t)) = G_0 + \sum_{i=1}^{n_G} G_i \exp(-\psi/\tau_i), \tag{4.6}$$

where G_0, G_i and τ_i are model parameters.

For viscoplasticity, we use the power law flow potential

$$\dot{\varepsilon}_{eq}^{p} = A_v \exp(-Q_v/k_B\theta)\left(\frac{\sigma_{eq}}{s^*}\right)^m, \tag{4.7}$$

$$s^* = \lambda^{(2)}\alpha^{(2)}s, \tag{4.8}$$

with J_2 flow direction

$$\dot{\varepsilon}_{ij}^{p} = \frac{3}{2}\dot{\varepsilon}_{eq}^{p}\frac{s_{ij}}{\sigma_{eq}}, \tag{4.9}$$

where the equivalent viscoplastic strain ε_{eq}^{p} is defined as $\varepsilon_{eq}^{p} \equiv \int_0^t \sqrt{\frac{2}{3}\dot{\varepsilon}_{ij}^{p}\dot{\varepsilon}_{ij}^{p}}\, dt'$, the equivalent

stress is defined as $\sigma_{eq} \equiv \sqrt{\frac{3}{2} s_{ij} s_{ij}}$, s_{ij} is the deviatoric stress ($s_{ij} \equiv \sigma_{ij} - \frac{1}{3}\sigma_{kk}\delta_{ij}$), $k_B = 1.3806\times10^{-23}\ (J \cdot K^{-1})$ is the Boltzmann constant, $\lambda^{(2)}$ and $\alpha^{(2)}$ are the moisture degradation factors, s^* is the state variable that indicates the material deformation resistance, and A_v, Q_v and m are material model parameters. Evolutions of the internal state variables s and η are governed by

$$\dot{s} = h_0\left(1 - \frac{s}{\tilde{s}(\eta)}\right)\dot{\varepsilon}^p_{eq}, \tag{4.10}$$

$$\dot{\eta} = g_0\left(\frac{s}{s_{cv}} - 1\right)\dot{\varepsilon}^p_{eq}, \tag{4.11}$$

$$\tilde{s}(\eta) = s_{cv}(1 + \omega(\eta_{cv} - \eta)), \tag{4.12}$$

with initial conditions $s(0) = s_0$ and $\eta(0) = 0$. In equations (4.10) - (4.12), h_0, g_0, ω and η_{cv} are parameters. A linear temperature dependence is included for the initial and saturation values of the state variable s, as

$$s_0 = s_0'(1 - \beta(\theta - \theta_{ref})), \qquad s_{cv} = s_{cv}'(1 - \beta(\theta - \theta_{ref})), \tag{4.13}$$

where s_0', s_{cv}' and β are material parameters.

The effects of moisture degradation are included in the model with the retention factors $\lambda^{(i)}$ and $\alpha^{(i)}$ ($i = 1,2$) in equations (4.5) and (4.8), where $i = 1$ corresponds to the stiffness retentions and $i = 2$ to the strength retentions. Hydrolytic degradation factors $\lambda^{(i)}$ depend on the moisture and temperature history, and are modeled using a kinetic equation with Arrhenius form:

$$-\frac{d\lambda^{(i)}}{dt} = \phi k^{(i)}(\theta)(\lambda^{(i)} - \lambda_\infty^{(i)})^n, \tag{4.14}$$

$$k^{(i)}(\theta) = A_h^{(i)} \exp(-Q_h^{(i)}/k_B\theta), \tag{4.15}$$

where ϕ is the normalized moisture concentration ($0 \le \phi \le 1$), and $\lambda_\infty^{(i)}$, $A_h^{(i)}$, $Q_h^{(i)}$ and n are parameters to be fit. The plasticization factors $\alpha^{(i)}$depend on the moisture level and temperature.

We use a simple linear model

$$\alpha^{(i)}(\theta,\phi) = \max\{1 - H^{(i)}(\theta)\phi, 0\}, \tag{4.16}$$

$$H^{(i)}(\theta) = \max\{a^{(i)}\theta + b^{(i)}, 0\}, \tag{4.17}$$

where $a^{(i)}$ and $b^{(i)}$ are determined experimentally.

The above constitutive equations were implemented as a user material (VUMAT) in the ABAQUS finite element for simulations of thermoset polyimides at elevated temperatures. A sample VUMAT code is provided in Appendix 4D. The material parameters for HFPE-II-52 polyimide resin [14], [22] at high temperature were identified through several tests. Extensive tension test data from monotonic loading, creep and stress relaxation tests at temperatures from 285, 300 and 315°C were used to fit the viscoelastic and viscoplastic model parameters in equations (4.2) – (4.13) (details in *Chapter 2*). The parameters for moisture degradation in equations (4.14) – (4.17) are identified with moisture saturation – compression testing experiments (details in *Chapter 3*). The stiffness retention factors $\lambda^{(1)}$ and $\alpha^{(1)}$ were determined by comparing the initial stiffness of degraded and virgin polyimide samples. It is assumed that the shear and bulk moduli reduce equally and that the relaxation time constants τ_i of the shear modulus do not change with moisture degradation. The yield strength retention factors $\lambda^{(2)}$ and $\alpha^{(2)}$ are determined by comparing the yield stresses of the moisture degraded and virgin samples. All model parameters are listed in Appendix 4C.

4.3 Finite Element Model

The above material constitutive model is used with finite element method to simulate the void growth of moisture saturated polyimide under rapid heating. The model is used to predict the critical blistering temperatures under different heating rates and moisture concentrations. Although

the actual physical processes in the blistering problem are complex and will involve void nucleation, void growth, and coalescence [36], in our finite element model only the growth of an isolated void is simulated. Specifically, as shown in Figure 4.1, an axisymmetric model of a single void is built. Physically this ignores nucleation and deals only with the subsequent growth of voids that have already nucleated. Assumptions implicit to the model are:

(1) The size of the initial void is large enough to allow continuum mechanics modeling.

(2) The shape of the void is spherical or ellipsoidal, and remains so.

(3) No void interactions are considered.

(4) The outer dimensions of the model are large relative to the void size ($a \ll c$; $b \ll c$).

(5) The time constant for heat transfer is small, so that temperature is uniform throughout the geometry.

(6) The structure is under rapid heating. Therefore, the material moisture concentration is constant and equal to the initial moisture concentration.

(7) The relative humidity (RH) in the void is equal to the material's normalized moisture level ϕ, and does not change during the void growth.

The last point assumes that the surrounding material provides moisture to the void at a rate fast enough to keep the void balanced with the material moisture level, and thus the pressure inside the void is

$$p(t) = p_{sat}(\theta(t))\,\chi = p_{sat}(\theta(t))\,\phi, \tag{4.18}$$

where χ is the RH inside the void, ϕ is the material initial normalized moisture level, and p_{sat} is the saturated steam pressure that depends only on temperature. Equation (4.18) is the upper bound to the pressure. See references [71]–[74] for details and a discussion of the more general case.

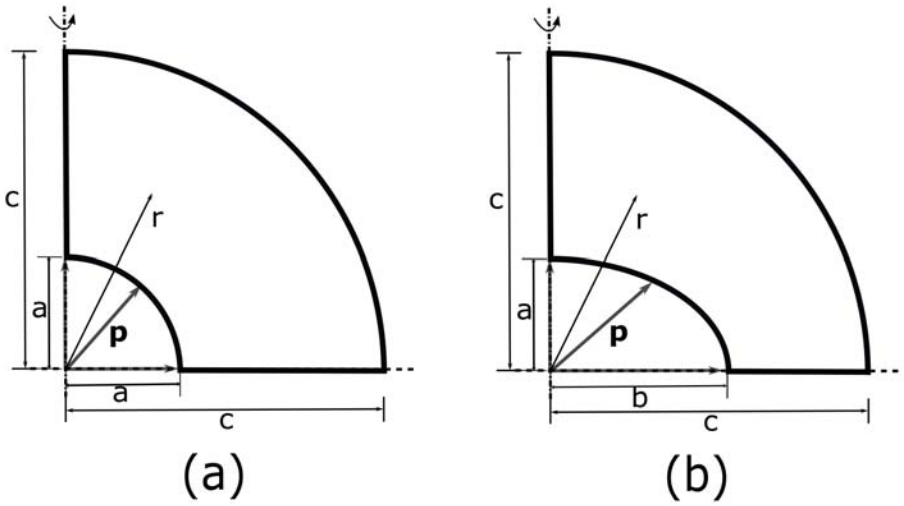

Figure 4.1: Geometries and dimensions (not scaled) of the axisymmetric finite element models of (a) a spherical void ($c/a = 20$); (b) an ellipsoidal void ($c/b = 20$).

The axisymmetric models shown in Figure 4.1 are traction free on the outer surface and subject to steam pressure loading on the inner surface. The dimensional ratios c/a and c/b are chosen to be 20 so that they are large enough to represent isolated voids in an infinite body ($a \ll c$; $b \ll c$). In the model temperature is ramped linearly in time from 0 to 360ºC. Solutions are computed using the commercial finite element code ABAQUS Explicit and the material constitutive model described in *Section 4.2* that was implemented as an ABAQUS user material (VUMAT). A mesh convergence test was conducted to ensure that the solution is converged. In the model the void expands due to the increasing level of steam pressure, and combined thermal and moisture induced softening. The volume expansion ratio $\Delta V/V_0$ where ΔV is the volume expansion and V_0 is the initial volume size of the void is computed and used to assess the onset of blistering under differing conditions.

4.4 Simulation Results

Simulations were run with the finite element model described in the previous section. A 10% volume change will be taken as the threshold for rapid void growth. This value lets us compare the results from different heating rates and moisture concentrations to each other.

Figure 4.2 shows the volume expansion ratio $\Delta V/V_0$ vs. temperature, for a spherical void under the conditions of 1°C/s heating rate and 100% moisture concentration. Also plotted is $\Delta V/V_0$ due to thermal expansion alone. The expansion curves start to deviate from the linear thermal expansion at around 200°C, which indicates the actual void growth. If the full material constitutive model is used, the void grows 10% in volume at 318°C, after which rapid growth is observed. At a temperature of 331°C, the void volume has grown by 100%.

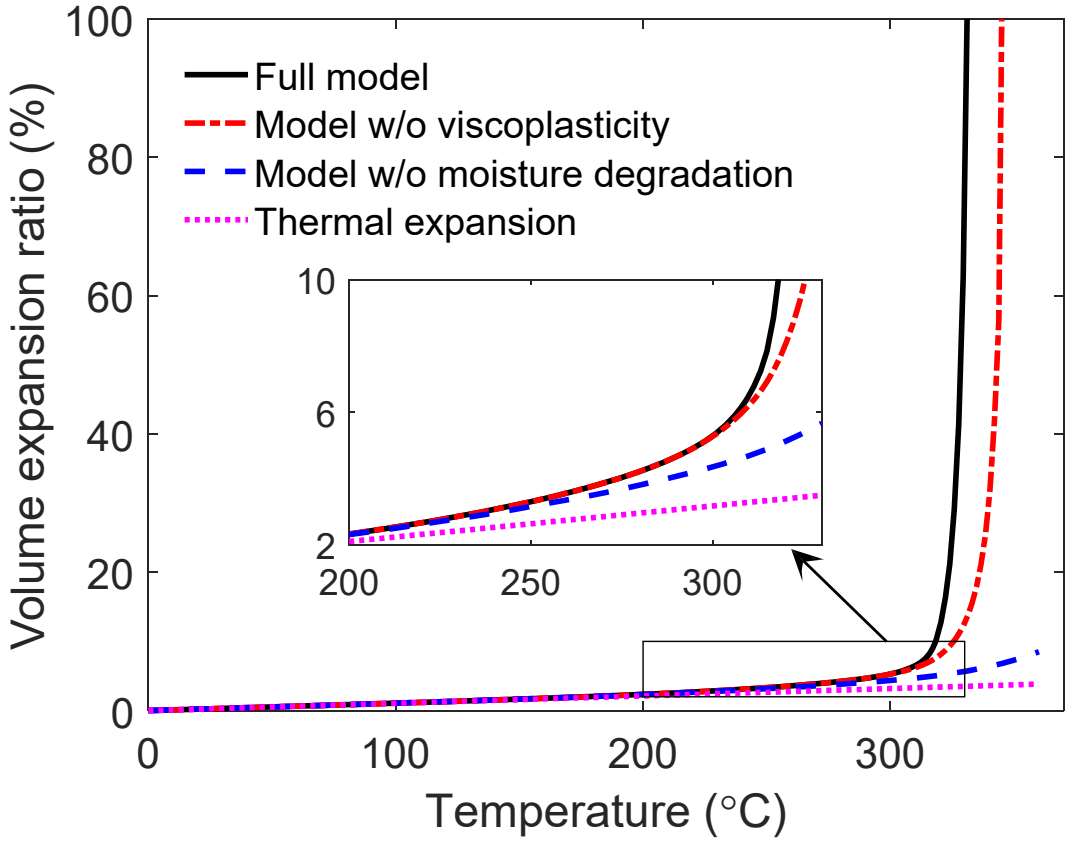

Figure 4.2: Volume expansion ratio vs. temperature under 1°C/s heating rate (from 0 to 360°C) and 100% moisture concentration

To test the contribution of individual parts of the material model to void growth, results with partial material models are also included in Figure 4.2. For a material model without viscoplasticity ($\varepsilon_{ij}^{p} = 0$), the result shows a delay of blistering to 325°C for 10% volume expansion. For a material model without moisture degradation ($\lambda^{(i)} = 1, \alpha^{(i)} = 1$ ($i = 1,2$)) but with viscoplasticity, the volume expansion ratio never reaches 10% before the T_g of 360°C. These results show that the effects of moisture degradation are crucial to the blistering damage of moisture saturated polyimide under rapid heating. Without moisture degradation the voids are stable up to the T_g.

To probe the model more deeply, Figure 4.3 plots the evolution of the state variable s^* (see equations (4.7), (4.8), (4.10) - (4.13)) of a material point on the void inner surface, where the maximum equivalent stress and strain are located. The evolution of s^*, which represents the material deformation resistance, combines effects of thermal softening, plastic strain, and moisture degradation. The state variable s^* generally drops as temperature increases, with a small bump near temperature 310°C, indicating material strain hardening and softening with the steam pressure loading (governed by equations (4.10) – (4.13)). The moisture degradation (hydrolytic degradation and plasticization) results in significant additional reductions of s^*.

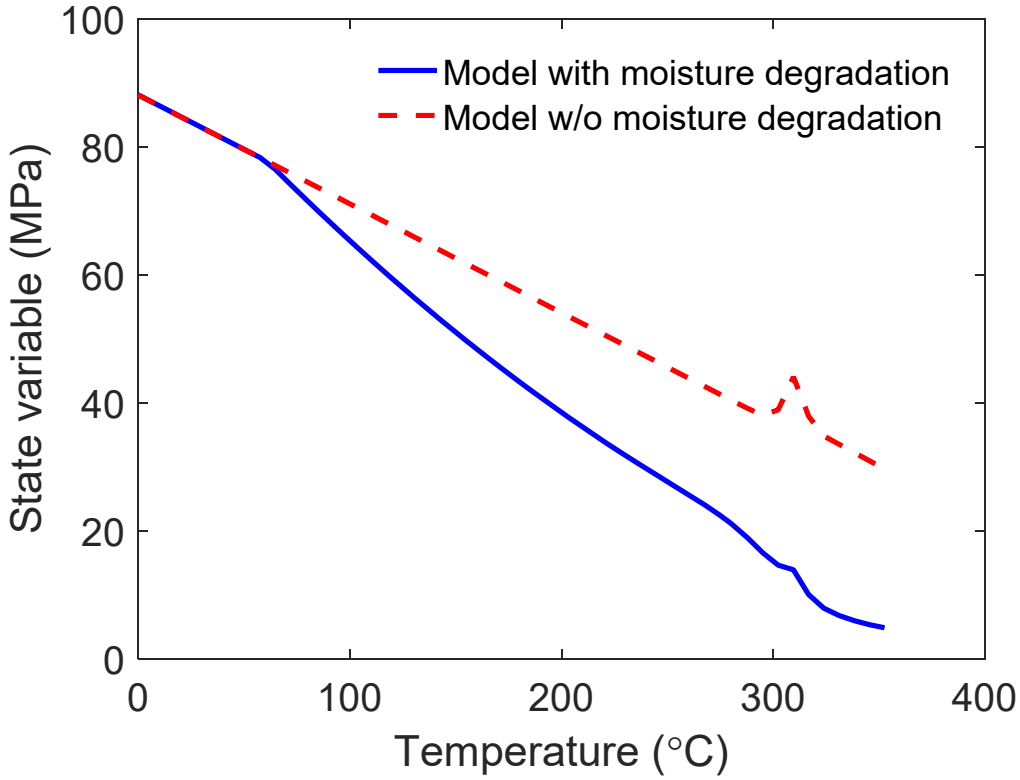

Figure 4.3: Evolution of state variable s^* of material point on the void inner surface, under 1°C/s heating rate (from 0 to 360°C) and 100% moisture concentration

4.4.1 Parametric studies

One of the advantages of the computational approach over the experimental study is the ability to perform parametric studies. Table 4.1 shows the computed blistering temperatures (defined as 10% volume expansion ratio) for different heating rates and material moisture concentrations. As the moisture level decreases, the level of steam pressure drops, and the effects of both hydrolytic degradation and plasticization decrease, thus blistering occurs at higher temperatures. In addition, the results show a delay of blistering with increasing heating rate since viscoelasticity, viscoplasticity and hydrolytic degradation in the material model are all time dependent. Faster heating rates provide less time for these effects to accumulate.

Table 4.1: Critical blistering temperatures for a spherical void under different heating rates and moisture levels

Heating rate (ºC/s)	Moisture level (%)	Temperature (ºC) at 10% volume expansion
1	100	318
1	75	331
1	50	346
1	25	>360
0.1	100	300
0.5	100	313
2	100	322
10	100	332
1.5	95	323

Figure 4.4 plots the evolutions of the material stiffness retention $\lambda^{(1)} \cdot \alpha^{(1)}$ and the yield strength retention $\lambda^{(2)} \cdot \alpha^{(2)}$ due to moisture degradation (combined effects of hydrolysis and plasticization) for selected heating rates and moisture levels. The results show that a higher moisture level increases the degree of degradation. Below 250ºC varying the heating rate does not influence the mechanical property reductions. This is because the dominant degradation mechanism at low temperature is plasticization, which is history independent (instantaneous). At higher temperatures, above 250ºC, the effects of hydrolytic degradation start to become significant, thus lower heating rates result in a faster degradation with respect to temperature.

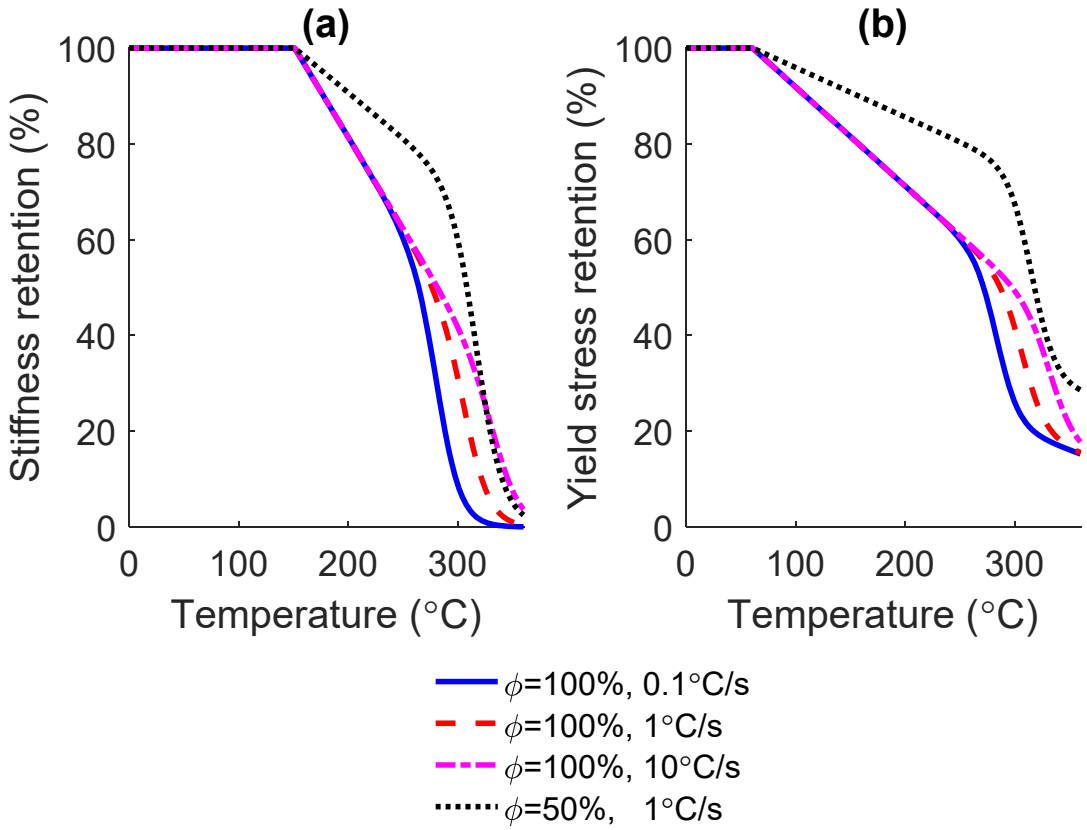

Figure 4.4: Mechanical property retentions due to hydrolytic degradation and plasticization (defined in equations (4.5), (4.8), (4.14) – (4.17)) vs. temperature for different heating rates and moisture levels. (a) Stiffness retention ($\lambda^{(1)} \cdot \alpha^{(1)}$); (b) yield stress retention ($\lambda^{(2)} \cdot \alpha^{(2)}$)

4.4.2 Effects of void shape

In applications, the shape of the void may be ellipsoidal instead of spherical. We present in this section the simulation results with an ellipsoidal void under rapid heating. A common heating rate 1°C/s and normalized moisture level 100% is used. The volume of void is $V = \frac{4}{3}\pi a b^2$, where a and b are in the minor and major radii, shown in Figure 4.1 (b). Table 4.2 summarizes the critical blistering temperatures for different initial ratios of a to b. It is noted that flatter the initial shape

of the void (larger b/a), the earlier blistering occurs.

Table 4.2: Critical blistering temperatures for different initial ratios of a and b (see Figure 4.1 (b)). Simulations were run with 1ºC/s heating rate from 0 to 360ºC, and 100% normalized moisture concentration

$a:b$	Temperature (ºC) at 10% volume expansion
1:1	318
1:4	309
1:10	286

4.5 Discussion

Czabaj et al. [34] performed an experimental study on blistering of HFPE-II-52 polyimide. It is hard to compare directly the simulation results with the experimental ones, because the overall sample expansion was measured in the experiments, while the volume expansion of single void is the focus of the simulation. However, in addition to measuring the overall expansion of the specimen in the experiments, a "ramp-quench" test is conducted, where a specimen was heated linearly until selected temperatures, removed quickly from the heater, and quenched into cold water to, as much as possible, freeze the state of void growth at a certain temperature. The sample was cut in half and was examined under a microscope. With a 1.5ºC/s heating rate and 95% initial moisture level, it was estimated that the rapid growth of a void occurs at temperature between 295ºC and 315ºC. In the simulation under the same heating rate and moisture concentration, the void expands 10% in volume at 323ºC (included in Table 4.1). Thus the modeling approach predicts a somewhat higher blistering temperature than the experiments. This is likely due to the interaction of voids in experiments which is not captured in the models. To a first approximation,

interacting voids can be modeled with decreasing $^{c}/_{a}$ ratio in the single void model (Figure 4.1 (a)). Changing from $^{c}/_{a} \gg 1$ to $^{c}/_{a} = 2$ in the finite element simulation reduces the 10% volume change threshold from 323ºC to 314ºC in line with the experimental results.

The results of the simulation show that the temperature threshold for the onset of blistering increases with decreasing moisture concentration consistent with the data in reference [34]. The model results also show that the temperature threshold increases with increasing heating rate, consistent with the experimental data.

To extend this work beyond a single material point to a structural application, the effects of heat transfer and moisture diffusion should be considered. The moisture diffusion is fast at high temperature, therefore a slow heating rate may significantly dry out the material before blistering could occur. In addition, for a thick/large structure under rapid heating, the temperature field, as well as the moisture concentration, would have a large gradient which would impact where the unstable void growth could occur inside the structure. Thus a full model would need to solve either sequentially, or simultaneously for the temperature, moisture and mechanical fields.

4.6 Summary and Conclusions

Finite element simulations are used to study the blistering of a moisture saturated polyimide under rapid heating. The simulations model a single void in a moisture saturated material under linearly increasing temperature. The model includes effects of the mechanical loading of the water vapor, thermal softening, viscoelastic and viscoplastic behaviors and moisture induced degradation of the mechanical properties of polyimides. The results are consistent with prior experimental observations with respect to trends in the blister onset conditions with moisture concentration and heating rate. The approach described here provides a computational means to predict the onset of

unstable void growth in thermosetting polyimides, but more importantly shows that blistering failure arises from the combined effects of high temperature, steam pressure loading and most critically, moisture degradation with both history dependent hydrolysis and instantaneous plasticization.

Appendix 4A Unit Cell Modeling of Growth of Voids in an Array

In the main text of *Chapter 4*, a finite element model is developed to simulate the growth of a single void (spherical or ellipsoidal) under steam pressure loading. The limitations of the analysis are twofold. First, the single void model assumes the void resides far from the other voids, thus the void interaction is ignored. Second, the model does not allow direct calculations of the overall structural expansions due to the steam pressure induced void growth, which is the quantity measured in the blistering experiments [34]. These limitations motivate the work described in this appendix, where we assume that spherical, equal-sized voids are evenly distributed as an array in a polyimide resin. Two packing mechanisms, simple cubic packing and face-centered cubic packing, are modeled with unit cells, as shown in Figure 4.5. The following symmetric boundary conditions are applied:

$$u_x(x = 0) = 0,\ u_y(y = 0) = 0, u_z(z = 0) = 0, \tag{4.19}$$

where u_x, u_y and u_z are displacements in x, y and z directions, respectively. In addition, periodic boundary conditions are applied with multi-point constraints: uniform u_x at surface $x = d$, and similarly, uniform u_y at surface $y = d$ and uniform u_z at surface $z = d$.

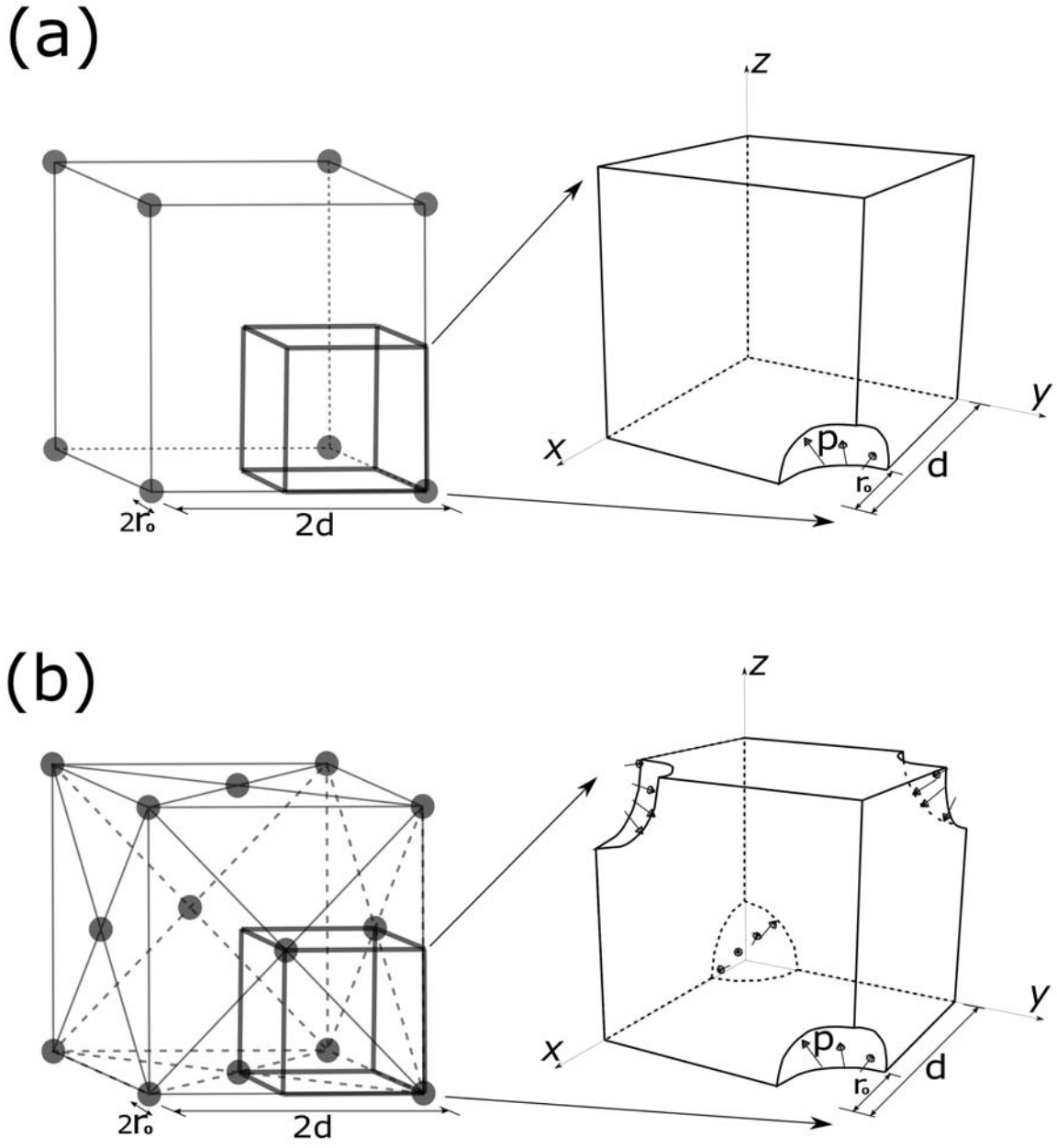

Figure 4.5: Unit cell models of an array of voids in two different packings. (a) simple cubic packing; (b) face-centered cubic packing. 1/8 of the unit cells are used in finite element with symmetric and periodic boundary conditions. The ratio r_0/d depends on the initial volume fraction of voids.

The material is subject to a saturated steam pressure loading on the inner surfaces of the voids and a linear temperature ramp from 0 to 360ºC. The heating rate and the moisture level are kept same as used in the single void model ($\dot{\theta} = 1℃/s$, $\phi = 1$). The average structure expansions, or the average strains (defined as $\frac{u_x}{d} = \frac{u_y}{d} = \frac{u_z}{d}$) are computed and plotted vs. temperature for different initial void densities. Figure 4.6, as an example, plots the overall structure expansions for different initial void volume fractions ($f_V = V_{void}/V_{total}$) and different packing assumptions. It is noted that different packing assumptions make little effect on the critical temperatures of blistering, while the initial void density plays an essential role, with earlier blistering for larger void density. Judging by the maximum amount of water the polyimide would absorb (3-4% by weight or 4-5% by volume), the initial void volume fraction should be close to 5%, where the critical temperature for blistering, estimated from Figure 4.6, is between 320ºC and 335ºC. In the experiments [34], however, rapid blistering was observed to occur at as early as around 265ºC, under the same heating rate. It remains a question then on what the mechanism is to drive the hygrothermal expansion which is not captured in the model.

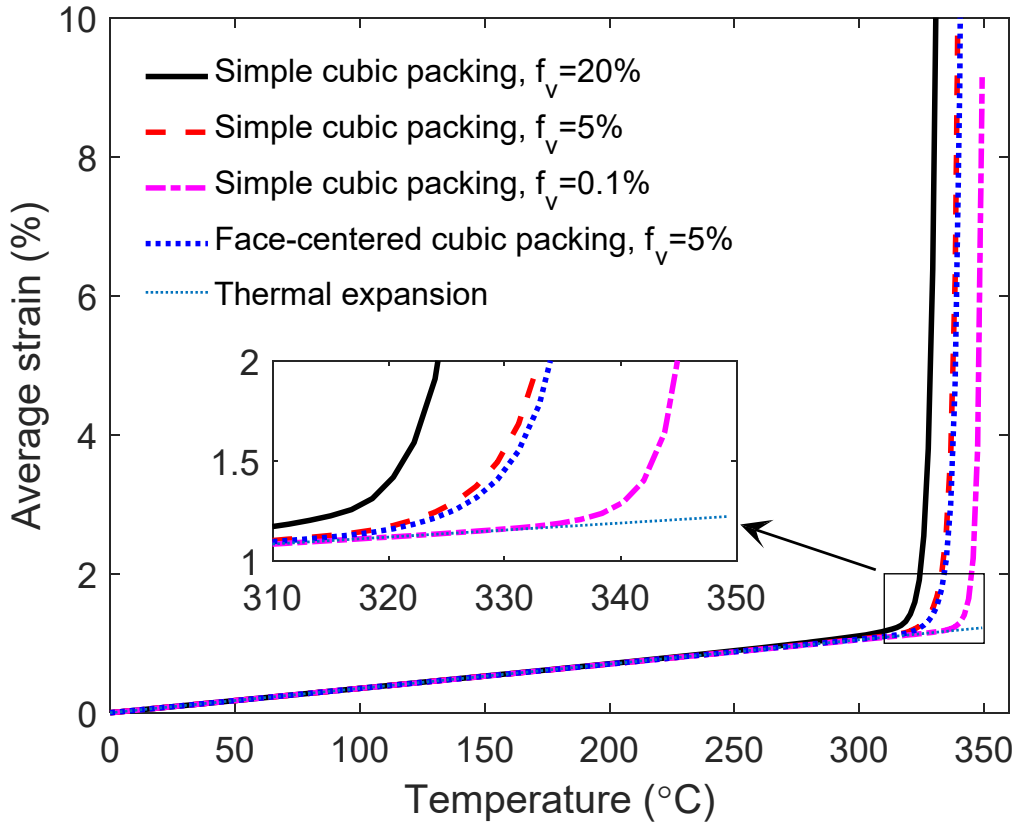

Figure 4.6: Average strain vs. temperature for different packing assumptions and different initial volume fractions of void (with 1°C/s heating rate and 100% moisture concentration)

Appendix 4B Preliminary Results on Delamination Modeling

In the context of polyimide matrix composite laminates, steam pressure induced delamination can occur as well as spherical void growth blistering. Experiments were performed in 2012 [35] by rapidly heating up a moisture saturated fiber reinforced polyimide laminate that contains a pre-implanted circular thin crack. The expansion of the flaw and the subsequent delamination growth was measured by a transverse extensometer. The crack growth and delamination are influenced by many factors including the material properties, thermal and moisture history, size of the pre-existing flaw, and the overall geometry of the structure, thus a computational approach to predict

the onset of delamination would be attractive. In this appendix, some initial efforts on finite element modeling of delamination of polyimide matrix laminates with a pre-existing crack are presented.

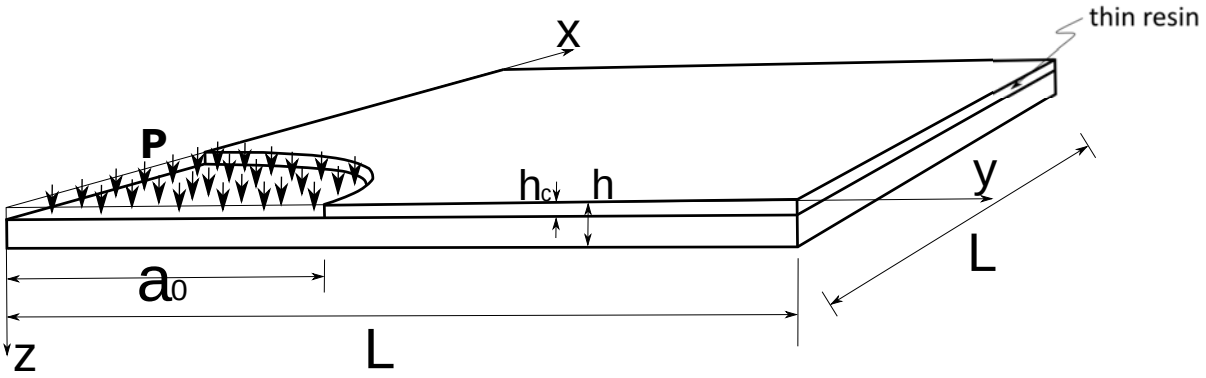

Figure 4.7: 3-D sketch and dimensions (not scaled) of the finite element geometry. 1/8 of the actual sample is modeled.

Figure 4.7 shows a 3-D sketch of the finite element model. The dimensions of the geometry are determined based on the actual laminate samples used in the experiments in reference [35]. The rectangular-shaped laminate has dimensions of $2L\times2L\times2h$ with $2L = 60mm$ and $2h = 1.65mm$. A cylindrical cavity sits in the center of the laminate with radius $a_0 = 10mm$ and height $2h_c = 0.1mm$. A thin resin layer with the same height as the cavity ($2h_c = 0.1mm$) sits in between the upper and lower plies of the laminates. Note that only 1/8 of the actual sample is modeled in finite element with symmetric boundary conditions. Figure 4.8 shows the finite element mesh used in ABAQUS.

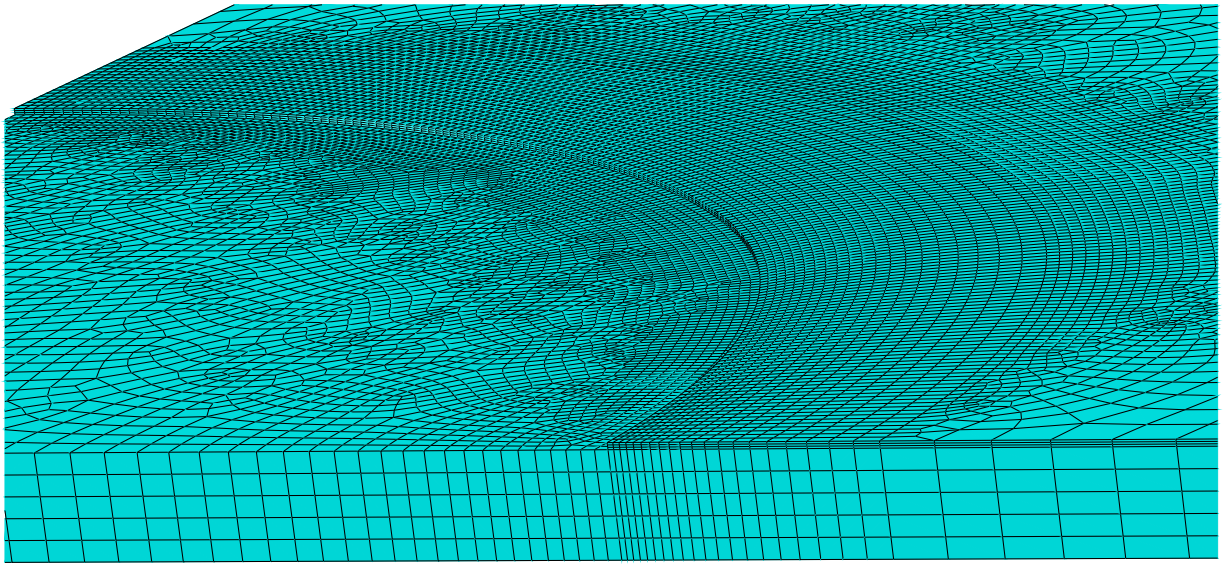

Figure 4.8: Finite element mesh used in ABAQUS

The material used here is graphite fiber reinforced polyimide matrix laminate (T650-35/HFPE-II-52). The thin polyimide resin layer, shown in Figure 4.7, uses the full material model developed in the previous section in this chapter, while the other parts of the laminates are assumed to be linear anisotropic elastic. Due to symmetry, only 6 material parameters are independent. They are listed in Table 4.3. The in-plane modulus $E_{xx} = E_{yy}$ which dominate the structural behavior are taken from reference [35] that were determined experimentally at 250°C. The other parameters are estimated based on the laminate composite theory [75] using the known elastic properties of HFPE-II-52 resin at 250°C [31] and the graphite fibers [63].

Table 4.3: Elastic properties of the laminates at 250°C

$E_{xx} = E_{yy}$ (GPa)	E_{zz} (GPa)	G_{xy} (GPa)	$G_{xz} = G_{yz}$ (GPa)	ν_{xy}	$\nu_{xz} = \nu_{yz}$
49.6	3.70	1.32	1.74	0.226	0.419

The structure is under a temperature ramp from 0 to 320ºC with a heating rate of 1ºC/s. The material moisture level is 95% to match with the experiment. The pressure level inside the cavity is determined with equation (4.18). The maximum deflection at center of the outer surface of the structure (point $(x, y, z) = (0,0, h)$) is measured vs. temperature, and is compared with the experiment, as shown in Figure 4.9. It is stated in the reference [35] that the onset of delamination is detected at around 226ºC. Before temperature 226ºC, the simulation results match well with the experiment. Note that no damage model is implemented in the finite element simulation and the crack would not propagate as it would in the experiments, thus the results of simulation underestimate the cavity growth at temperature above 226ºC. It is also worth noting that since delamination occurs at relatively low temperature, the effect of moisture degradation is not crucial. Future work is recommended to add cohesive zone model in the finite element analysis, allowing crack propagation between lamina plies.

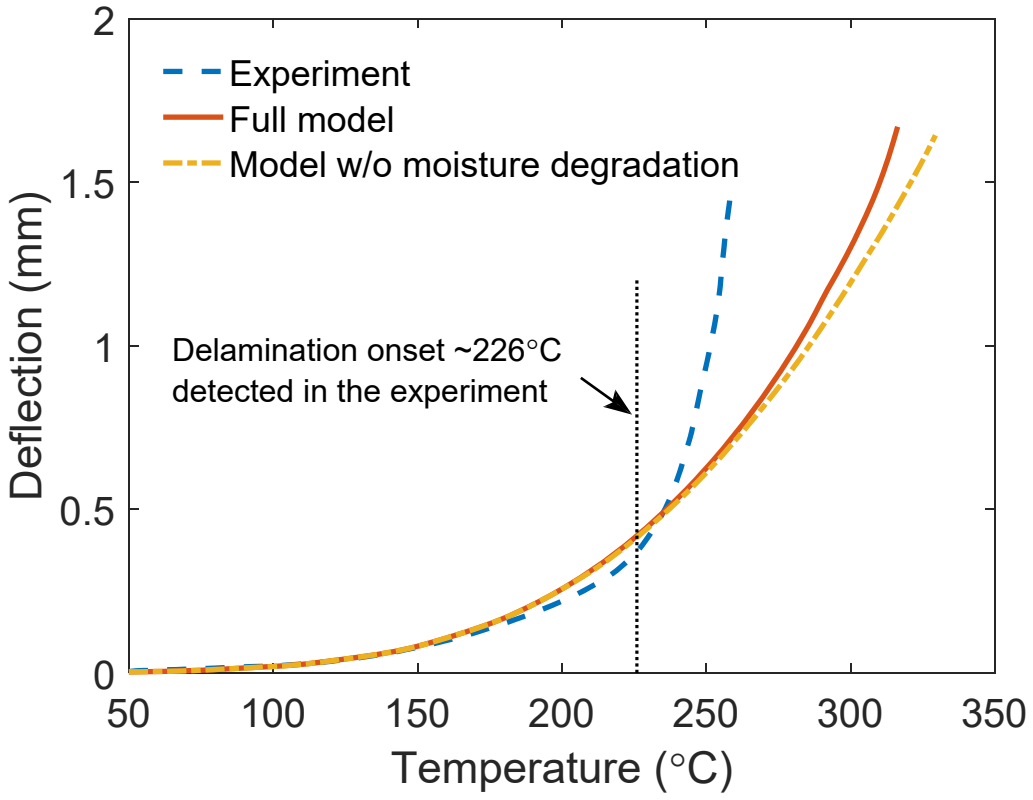

Figure 4.9: Deflections vs. temperature at point $(x, y, z) = (0,0,h)$ for experiment and finite element simulations. The experimental data is digitalized from Figure 7 in reference [35]. A common heating rate (1°C/s) and material moisture level (95%) is used for both the experimental and modeling results.

Appendix 4C List of Material Parameters

Table 4.4: Material model parameters for viscoelasticity (defined in equations (4.2) - (4.4), (4.6) in the main text)

G_1 (MPa)	9.61	τ_1 (s)	3.85	n_G	7
G_2 (MPa)	16.6	τ_2 (s)	3.44×10^{1}	G_0 (MPa)	336
G_3 (MPa)	20.9	τ_3 (s)	1.11×10^{2}	K (GPa)	3.38
G_4 (MPa)	56.2	τ_4 (s)	2.56×10^{3}	C_1	-25.3
G_5 (MPa)	54.8	τ_5 (s)	2.53×10^{4}	C_2 (°C)	-360
G_6 (MPa)	43.7	τ_6 (s)	1.64×10^{5}	θ_{ref} (°C)	285
G_7 (MPa)	67.6	τ_7 (s)	3.57×10^{6}		

Table 4.5: Material model parameters for viscoplasticity (defined in equations (4.7), (4.9) – (4.13) in the main text)

A_v (s^{-1})	5.90×10^{6}	ω	730
Q_v (J)	1.60×10^{-19}	η_{cv}	4.97×10^{-4}
m	11.7	s_0' (MPa)	39.6
h_0 (GPa)	9.07	s_{cv}' (MPa)	41.8
g_0	0.116	β	0.0043

Table 4.6: Material model parameters for hydrolytic degradation and plasticization (defined in equations (4.5), (4.8), (4.14) – (4.17) in the main text)

n	2	$A_h^{(1)}$ (s^{-1})	3.09×10^{19}	$a^{(1)}$ (1/°C)	3.81×10^{-3}
$\lambda_\infty^{(1)}$	0	$A_h^{(2)}$ (s^{-1})	1.14×10^{22}	$a^{(2)}$ (1/°C)	2.07×10^{-3}
$\lambda_\infty^{(2)}$	0.4	$Q_h^{(1)}$ (J)	3.82×10^{-19}	$b^{(1)}$	-0.576
		$Q_h^{(2)}$ (J)	4.23×10^{-19}	$b^{(2)}$	-0.126

Appendix 4D Sample ABAQUS VUMAT Script

```
!*****************************************************************************
! VUMAT Subroutine Written in FORTRAN 77 for Use as ABAQUS Explicit user material
!
!     This script works for cases of plane strain, axisymmetric or 3-D. (the
!     script for plane stress is written separately.)
!
!     To run this script, type "abaqus job=<input file name> user=<vumat file
!     name>" in cmd window. In the input file, define all model material
!     parameters under *User Material.
!
!     The parameters should be provided in the order of (nG, g_i (i=1:nG),
!     tao_i (i=1:nG), G_0, K_0, A_v, Q_v, m, h0, g0, omega, eta_cv, s_cvprime,
!     s_0prime, beta, temp_ref, C1, C2, phi, a1, b1, a2, b2, Ah1, Qh1, Ah2, Qh2)
!     as defined in the above tables. Lines 117-152 of the code below list
!     all material parameters read from ABAQUS.
!
!     Note that viscoelastic parameters g_i=G_i/G_0. The material moisture
!     concentration phi is treated as a material parameter in this vumat, instead
!     of a field variable.
!
!     The code contains 5 main sections:
!     Lines 1-29    : default ABAQUS vumat header;
!     Lines 30-89   : variable declarations;
!     Lines 90-194  : necessary pre-processing including constant definitions
!                     (lines 94-99), dimension allocations (lines 100-115),
!                     material parameter readings (lines 117-152), and solution
!                     dependent variable readings (lines 153-194);
!     Lines 195-319 : main part of vumat, applying constitutive equations to
!                     update stress;
!     Lines 320-412 : utility subroutines.
!
!     The material model is used for thermosetting polyimides at high temperature
!     and/or high humid environments. The model includes linear viscoelasticity,
!     state variable viscoplasticity, hydrolytic degradation and plasticization.
!*****************************************************************************
! Default header and interface link to ABAQUS Explicit (DO NOT CHANGE)
!*****************************************************************************
      subroutine vumat(
C Read only
     +  nblock, ndir, nshr, nstatev, nfieldv, nprops, lanneal,
     +  stepTime, totalTime, dt, cmname, coordMp, charLength,
     +  props, density, strainInc, relSpinInc,
     +  tempOld, stretchOld, defgradOld, fieldOld,
     +  stressOld, stateOld, enerInternOld, enerInelasOld,
     +  tempNew, stretchNew, defgradNew, fieldNew,
C Write only
     +  stressNew, stateNew, enerInternNew, enerInelasNew )
C
      include 'vaba_param.inc'
C
C All arrays dimensioned by (*) are not used in this algorithm
C
      dimension props(nprops), density(nblock),
     +  coordMp(nblock,*),
     +  charLength(*), strainInc(nblock,ndir+nshr),
     +  relSpinInc(*), tempOld(nblock),
     +  stretchOld(*), defgradOld(*),
```

```
     +  fieldOld(*), stressOld(nblock,ndir+nshr),
     +  stateOld(nblock,nstatev), enerInternOld(nblock),
     +  enerInelasOld(nblock), tempNew(nblock),
     +  stretchNew(*), defgradNew(*), fieldNew(*),
     +  stressNew(nblock,ndir+nshr), stateNew(nblock,nstatev),
     +  enerInternNew(nblock), enerInelasNew(nblock)
C
      character*80 cmname
C
************************************************************************************
! VARIABLE DECLARATIONS
************************************************************************************
C     Constants
C
      real*8 zero, one, two, three, third, half, twoThirds
      real*8 ten, threeseconds, nearOne
      real*8 kB, TC2K, RGas
C
C     Material parameters
C
      integer ComN ! Number of stress (strain) components (3D: ComN=6;
                   ! strain or axisymmetric: ComN=4)
      integer ProN ! Number of terms in Prony series (viscoelasticity)
      real G0, K0  ! Shear and bulk moduli
      real, dimension(:) ,allocatable :: gi, taoi ! Normalized Gi and
                                                  ! time constants
C
      real TempRef, C1, C2 ! WLF parameters
      real Av, Qv, mm, hh0, gg0, omega, etacv, scvstar, SS0, beta
                                     ! parameters for viscoplasticity

      real Phi, a1, b1, a2, b2 ! parameters for plasticization
      real Ah1, Qh1, Ah2, Qh2  ! parameters for hydrolysis
C
C     Solution dependent state variables
C
      real*8, dimension(:,:) ,allocatable :: eiOld ! viscoelasticity
      real*8, dimension(:) ,allocatable :: eOld    ! viscoelasticity
      real*8  EQPStrainOld, SSOld, etaOld          ! viscoplasticity
      real*8  hyIntEOld, hyIntpOld                 ! hydrolysis
C
C     Field variables read from last iteration
C
      real*8 TempNewi, TempOldi
      real*8, dimension(:) ,allocatable :: StressOldi, StressNewi
      real*8, dimension(:) ,allocatable :: StrainInci
      real*8 densityi, EnerInternOldi, EnerInternNewi
C
C     Internal variables for viscoplasticity
C
      real*8 VolEStrainInc, EQStress
      real*8, dimension(:) ,allocatable ::  DevStressOld, DevEStrainInc
      real*8 scv, seta, dss, deta, EQPStrainInc, Termdep, Saddon, SSOldF
      integer i,j,k
      real*8, dimension(:) ,allocatable ::  PStrainInc, EStrainInc
C
C     Internal variables for viscoelasticit
C
      real*8 hathOld, hathNew, hathDiff
      real*8 athInvOld, athInvNew, athOld, athNew
```

```
      real*8 dtao
      real*8, dimension(:) ,allocatable ::  DevStressInc
      real*8 Termdei1, Termdei2, dei
C
C     Internal variables for plasticization and hydrolysis
C
      real*8 hE, hp, alphap, alphaE, SSOldS, G0S, K0S
      real*8 lambdaE, lambdap, lambdaInf, kkE, kkp
C
*******************************************************************************
! ALLOCATIONS
*******************************************************************************
C
      parameter( zero = 0.d0, one = 1.d0, two = 2.d0, three = 3.d0,
     +  third = one/three, half = .5d0, twoThirds = two/three,
     +  threeseconds = three/two, ten = 10.d0, kB = 1.3806488e-23,
     +  TC2K = 273.15d0, nearOne = 0.999d0, Rgas = 8.31441d0,
     +  lambdaInf = 0.4d0)
C
C      Dimension allocations
C
      ProN = props(1)    ! Number of Prony terms
      ComN = nshr + ndir ! Number of Components
      allocate(gi(ProN))
      allocate(taoi(ProN))
      allocate(eiOld(ProN,ComN))
      allocate(eOld(ComN))
      allocate(StressOldi(ComN))
      allocate(StressNewi(ComN))
      allocate(StrainInci(ComN))
      allocate(DevStressOld(ComN))
      allocate(DevEStrainInc(ComN))
      allocate(PStrainInc(ComN))
      allocate(EStrainInc(ComN))
      allocate(DevStressInc(ComN))
C
C     Material properties read from Abaqus input file
C
      do j = 1,ProN              ! viscoelasticity
        gi(j) = props(j+1)
        taoi(j) = props(ProN+j+1)
      enddo
      G0 = props(2*ProN+2)
      K0 = props(2*ProN+3)
C
      Av     = props(2*ProN+4)    ! viscoplasticity
      Qv     = props(2*ProN+5)
      mm     = props(2*ProN+6)
      hh0    = props(2*ProN+7)
      gg0    = props(2*ProN+8)
      omega  = props(2*ProN+9)
      etacv  = props(2*ProN+10)
      scvstar= props(2*ProN+11)
      ss0    = props(2*ProN+12)
      beta   = props(2*ProN+13)
C
      TempRef= props(2*ProN+14)    ! WLF
      C1     = props(2*ProN+15)
      C2     = props(2*ProN+16)

```

```
141   C
142         Phi    = props(2*ProN+17)   ! Plasticization
143         a1     = props(2*ProN+18)
144         b1     = props(2*ProN+19)
145         a2     = props(2*ProN+20)
146         b2     = props(2*ProN+21)
147   C
148         Ah1    = props(2*ProN+22)   ! Hydrolytic degradation
149         Qh1    = props(2*ProN+23)
150         Ah2    = props(2*ProN+24)
151         Qh2    = props(2*ProN+25)
152   C
153   ************************************************************************************
154   ! PREPROCESSING
155   ************************************************************************************
156   C
157         do i = 1,nblock ! loop over each Gauss point
158   C
159   C       Temperature
160   C
161           TempOldi = tempOld(i)
162           TempNewi = tempNew(i)
163           Temp = (TempOldi + TempNewi)/two  ! in degree C
164   C
165   C       Solution dependent state variables for viscoelasticity
166   C
167           do k = 1,ComN
168             eOld(k) = StateOld(i,ComN*ProN+k)
169             do j = 1,ProN
170               eiOld(j,k) = StateOld(i,(j-1)*ComN+k)
171             enddo
172           enddo
173   C
174   C       Solution dependent state variables for viscoplasticity
175   C
176           EQPStrainOld = StateOld(i,ComN*ProN+ComN+1)
177           SSOldF = StateOld(i,ComN*ProN+ComN+2)
178           etaOld = StateOld(i,ComN*ProN+ComN+3)
179   C
180   C       Solution dependent state variables for hydrolytic degradation
181   C
182           hyIntEOld = StateOld(i,ComN*ProN+ComN+4)
183           hyIntpOld = StateOld(i,ComN*ProN+ComN+5)
184   C
185   C       Other preprocessings
186   C
187           Saddon = ss0 * (one - beta * (Temp - TempRef))  ! state variables
188                                                           ! start from zero
189           SSOld = SSOldF + Saddon    ! Old state variable s
190           StressOldi = StressOld(i,1:ComN)
191           StrainInci = StrainInc(i,1:ComN)
192           densityi = density(i)
193           EnerInternOldi = EnerInternOld(i)
194   C
195   ************************************************************************************
196   ! VISCOPLASTICITY
197   ************************************************************************************
198   C
199           call DevCal(StressOldi,DevStressOld,ComN) ! obtain deviatoric stress
200           call EQStressCal(DevStressOld,EQStress,ComN)  ! obtain equivalent stress
```

```
201           scv = scvstar * (one - beta * (Temp - TempRef))! temperature dependent "s"
202     C
203     C       Moisture effect on strength
204     C
205           hp = min(max(ap * Temp + bp, zero),nearOne)
206           alphap = one - hp * Phi ! plasticization
207           lambdap = one/(hyIntpOld + one/(one-lambdaInf)) + lambdaInf ! hydrolysis
208           SSOldS = SSOld * alphap * lambdap
209
210           EQPStrainInc = Av * exp(-Qv/(kB*(Temp + TC2K))) *
211         +                (EQStress/SSOldS)**mm*dt ! equivalent strain increment
212           StateNew(i,ComN*ProN+ComN+1) = EQPStrainInc + EQPStrainOld
213     C
214     C       Update state variables ss, eta
215     C
216           seta = scv * (one + omega * (etacv - etaOld))
217           dSS = hh0 * (one - SSOld/seta) * EQPStrainInc
218           deta = gg0 * (SSOld/scv - one) * EQPStrainInc
219           StateNew(i,ComN*ProN+ComN+2) = dSS + SSOld - Saddon
220           StateNew(i,ComN*ProN+ComN+3) = deta + etaOld
221     C
222     C       Update state variables for hydrolytic degradation
223     C
224           kkE = Ah1 * exp(-Qh1/Rgas/(Temp + TC2K)) ! rate constant for
225                                                    ! modulus degradation
226           kkp = Ah2 * exp(-Qh2/Rgas/(Temp + TC2K)) ! rate constant for
227                                                    ! yield degradation
228           StateNew(i,ComN*ProN+ComN+4) = hyIntEOld + Phi * kkE * dt
229           StateNew(i,ComN*ProN+ComN+5) = hyIntpOld + Phi * kkp * dt
230     C
231     C       Zero dividend protection
232     C
233           if (EQStress - zero .le. 1E-10) then
234             Termdep = zero
235           else
236             Termdep = threeseconds/EQStress*EQPStrainInc
237           endif
238     C
239           do j = 1,ComN
240             PStrainInc(j) = Termdep * DevStressOld(j) ! plastic strain increments
241             EStrainInc(j) = StrainInci(j) - PStrainInc(j) ! elastic strain
242                                                           ! increments
243           enddo
244     C
245     ********************************************************************************
246     ! VISCOELASTICITY
247     ********************************************************************************
248     C
249           call DevCal(EStrainInc,DevEStrainInc,ComN) ! obtain deviatoric strain inc.
250           VolEStrainInc = EStrainInc(1) + EStrainInc(2) + EStrainInc(3)
251                                    ! volumetric strain increment
252     C
253     C       Moisture effect on stiffness
254     C
255           hE = min(max(a1 * Temp + b1, zero), nearOne)
256           alphaE = one - hE * Phi ! plasticization
257           lambdaE = one/(hyIntEOld + one) ! hydrolysis
258           G0S = G0 * alphaE * lambdaE ! long term shear moduli
259           K0S = K0 * alphaE * lambdaE ! bulk moduli
260
```

```
          do k = 1,ComN
            DevStressInc(k) = two * G0S * DevEStrainInc(k)
          enddo
C
C       Reduced time
C
          hathOld = C1 * (TempOldi - TempRef)/
     +           (C2 + TempOldi - TempRef) ! -log10(atheta)
          hathNew = C1 * (TempNewi - TempRef)/
     +           (C2 + TempNewi - TempRef) ! -log10(atheta)
          hathDiff = hathNew - hathOld
          athInvOld = ten**(hathOld)
          athInvNew = ten**(hathNew)
          athOld = one/athInvOld
          athNew = one/athInvNew
          if (hathDiff .le.1E-8) then
            dtao = dt/((athOld + athNew)/two)
          else
            ! for highly nonlinearity case
            dtao = (athInvNew - athInvOld)/hathDiff/log(ten)*dt
        endif
C
C     Refer to ABAQUS theory manual for detailed algorithms of computational
C     viscoelasticity
C
        do j = 1,ProN
            Termdei1 = taoi(j)/dtao*
     +              (dtao/taoi(j) + exp(-dtao/taoi(j)) - one)
            Termdei2 = one - exp(-dtao/taoi(j))
            do k = 1,ComN
              dei = Termdei1 * DevEStrainInc(k)
     +          + Termdei2 * (eold(k) - eiold(j,k))
              StateNew(i,(j-1)*ComN+k) = eiOld(j,k) + dei
              DevStressInc(k) = DevStressInc(k) - two * G0S * gi(j) * dei
            enddo
        enddo
C
C       Update stress and state variables
          do k = 1,ComN
            StateNew(i,ComN*ProN+k)  = eOld(k) + DevEStrainInc(k)
            StressNewi(k) = StressOldi(k) + DevStressInc(k)
          enddo
C
          do k = 1,3
            StressNewi(k) = StressNewi(k) + K0S * VolEStrainInc
        enddo
C
C       Energy calculation
C
          call EnergyCal(StressOldi,StressNewi,
     +           StrainInci,densityi,EnerInternOldi,
     +           EnerInternNewi,ComN)
C
          StressNew(i,1:ComN) = StressNewi
          EnerInternNew(i) = EnerInternNewi
        enddo
        return
        end subroutine vumat
C
********************************************************************************
```

```
321   ************************************************************************
322   ! The following subroutine is used to calculate the strain energy
323   C
324         subroutine EnergyCal(StressOld,StressNew,StrainInc,
325        +                     density,EnerInternOld,EnerInternNew,N)
326
327         implicit none
328   C
329         integer N
330         real*8 Half, two
331         real*8 StressOld(N),StressNew(N),StrainInc(N)
332         real*8 density, EnerInternOld, EnerInternNew
333         real*8 stressPower
334         parameter(Half = .5, two = 2.0)
335   C
336            stressPower = half * (
337        1     ( stressOld(1)+stressNew(1) )*strainInc(1)
338        1    +( stressOld(2)+stressNew(2) )*strainInc(2)
339        1    +( stressOld(3)+stressNew(3) )*strainInc(3)
340        1    + two*( stressOld(4)+stressNew(4) )*strainInc(4))
341         if (N .gt. 4) then
342            stressPower = stressPower + half * (
343        1    + two*( stressOld(5)+stressNew(5) )*strainInc(5)
344        1    + two*( stressOld(6)+stressNew(6) )*strainInc(6))
345         endif
346
347             enerInternNew = enerInternOld
348        1    + stressPower / density
349   C
350         end subroutine EnergyCal
351
352   ************************************************************************
353   ************************************************************************
354   ! The following subroutine is used to calculate the deviatoric matrix from
355   ! a 3*3 or 2*2 symmetric matrices
356   !
357   ! For 3D, 6 independent components are stored as the following way:
358   ! Ma(1;3) are the diagonal terms.
359   ! Ma(4:6) are the off-diagonal terms.
360   C
361         subroutine DevCal(Ma,DevMa,N)
362         implicit none
363   C
364         real*8 one, three, onethird
365         integer i, N
366         real*8 Ma(N), DevMa(N)
367
368         real*8 trace, pressure
369         parameter(one = 1.d0, three = 3.d0, onethird = one/three)
370   C
371   C For 3d, plane strain, axisymmetric
372   C
373         trace  = Ma(1) + Ma(2) + Ma(3)
374         pressure = onethird * trace
375         do i = 1,3
376           DevMa(i) = Ma(i) - pressure
377         enddo
378         DevMa(4) = Ma(4)
379         if (N .gt. 4) then
380           DevMa(5) = Ma(5)
```

```
381           DevMa(6) = Ma(6)
382         endif
383
384         end subroutine DevCal
385   ***************************************************************************
386   ***************************************************************************
387   ! The following subroutine is used to calculate the equivalent stress.
388   ! Ma has to be symmetric.
389         subroutine EQStressCal(Ma,EQ,N)
390         implicit none
391   C
392         real*8 zero, two, threeseconds
393         integer i, N
394         real*8 Ma(N), Mag, EQ
395         parameter(zero = 0.d0, two = 2.d0, threeseconds = 1.5d0)
396   C
397         Mag = zero
398   C
399         do i = 1,3
400           Mag = Mag + Ma(i) * Ma(i)
401         enddo
402   C
403         Mag = Mag + two * Ma(4) * Ma(4)
404         if (N .gt. 4) then
405           Mag = Mag + two * Ma(5) * Ma(5)
406           Mag = Mag + two * Ma(6) * Ma(6)
407         endif
408
409   C
410         EQ = sqrt(threeseconds * Mag)
411         end subroutine EQStressCal
412   ***************************************************************************
```

BIBLIOGRAPHY

[1] M. A. Meador, "Recent advances in the development of processable high-temperature polymers 1," *Annu. Rev. Mater. Sci.*, vol. 28, no. 1, pp. 599–630, 1998.

[2] D. L. McDanels, T. T. Serafini, and J. A. DiCarlo, "Polymer, metal, and ceramic matrix composites for advanced aircraft engine applications," *J. Mater. energy Syst.*, vol. 8, no. 1, pp. 80–91, 1986.

[3] D.-J. Liaw, K.-L. Wang, Y.-C. Huang, K.-R. Lee, J.-Y. Lai, and C.-S. Ha, "Advanced polyimide materials: syntheses, physical properties and applications," *Prog. Polym. Sci.*, vol. 37, no. 7, pp. 907–974, 2012.

[4] K. Vanherck, G. Koeckelberghs, and I. F. J. Vankelecom, "Crosslinking polyimides for membrane applications: a review," *Prog. Polym. Sci.*, vol. 38, no. 6, pp. 874–896, 2013.

[5] C. E. Sroog, "History of the invention and development of the polyimides," *Plast. Eng. YORK-*, vol. 36, pp. 1–6, 1996.

[6] C. L. Bowman, J. K. Sutter, J. C. Thesken, and B. P. Rice, "Characterization of graphite fiber/polyimide composites for RLV applications," *2001 A Mater. Process. odyssey*, pp. 1515–1529, 2001.

[7] M. Ivosevic, R. Knight, S. R. Kalidindi, G. R. Palmese, and J. K. Sutter, "Microstructure and properties of thermally sprayed functionally graded coatings for polymeric substrates," *NASA TM report, 212119*, 2003.

[8] K. J. Bowles and G. Nowak, "Thermo-oxidative stability studies of Celion 6000/PMR-15 unidirectional composites, PMR-15, and Celion 6000 fiber," *J. Compos. Mater.*, vol. 22, no. 10, pp. 966–985, 1988.

[9] X. Jin, L. Huang, Y. Shi, S. Yang, and A. Hu, "Thermosetting process and thermal degradation mechanism of high-performance polyimide," *J. Anal. Appl. Pyrolysis*, vol. 64, no. 2, pp. 395–406, 2002.

[10] K. C. Chuang, R. D. Vannucci, I. Ansari, L. L. Cerny, and D. A. Scheiman, "High flow addition curing polyimides," *J. Polym. Sci. Part A Polym. Chem.*, vol. 32, no. 7, pp. 1341–1350, 1994.

[11] W. Xie, R. Heltsley, H. Li, C. Lee, and W. Pan, "Study of the processing chemistry of polyimides with thermogravimetry/Fourier transform infrared/mass spectrometry techniques," *J. Appl. Polym. Sci.*, vol. 83, no. 10, pp. 2213–2224, 2002.

[12] J. D. Russell and J. L. Kardos, "Crosslinking characterization of a polyimide: AFR700B," *Polym. Compos.*, vol. 18, no. 5, pp. 595–612, 1997.

[13] D. Wilson, “PMR-15 processing, properties and problems—a review,” *Br. Polym. J.*, vol. 20, no. 5, pp. 405–416, 1988.

[14] J. Antonakakis, “Linear viscoelastic properties of HFPE-II-52 polyimide,” M.S. Thesis, Cornell University, 2005.

[15] A. I. Wozniak, A. S. Yegorov, V. S. Ivanov, S. M. Igumnov, and K. V Tcarkova, “Recent progress in synthesis of fluorine containing monomers for polyimides,” *J. Fluor. Chem.*, vol. 180, pp. 45–54, 2015.

[16] T. Kurosawa, T. Higashihara, and M. Ueda, “Polyimide memory: a pithy guideline for future applications,” *Polym. Chem.*, vol. 4, no. 1, pp. 16–30, 2013.

[17] C. Marais and G. Villoutreix, “Analysis and modeling of the creep behavior of the thermostable PMR-15 polyimide,” *J. Appl. Polym. Sci.*, vol. 69, no. 10, pp. 1983–1991, 1998.

[18] A. J. W. McClung and M. B. Ruggles-Wrenn, “The rate (time)-dependent mechanical behavior of the PMR-15 thermoset polymer at elevated temperature,” *Polym. Test.*, vol. 27, no. 7, pp. 908–914, 2008.

[19] R. Chen, Y. C. Lu, F. Yang, G. P. Tandon, and G. A. Schoeppner, “Impression creep of PMR-15 resin at elevated temperatures,” *Polym. Eng. Sci.*, vol. 50, no. 1, pp. 209–213, 2010.

[20] S. Karra and K. R. Rajagopal, “Modeling the non-linear viscoelastic response of high temperature polyimides,” *Mech. Mater.*, vol. 43, no. 1, pp. 54–61, 2011.

[21] M. B. Ruggles-Wrenn and O. Ozmen, “The Rate (Time)-Dependent Mechanical Behavior of the PMR-15 Thermoset Polymer at 316 C: Experiments and Modeling,” *J. Press. Vessel Technol.*, vol. 132, no. 4, p. 41403, 2010.

[22] P. Bhargava, “High temperature properties of HFPE-II-52 polyimide resin and composites,” Ph.D. Dissertation, Cornell University, 2007.

[23] Y. Xu, P. Bhargava, and A. Zehnder, “Time and temperature dependent mechanical behavior of HFPE-II-52 polyimide at high temperature,” *Mech. Mater.*, vol. 100, pp. 86–95, 2016.

[24] R. DeIasi and J. Russell, “Aqueous degradation of polyimides,” *J. Appl. Polym. Sci.*, vol. 15, no. 12, pp. 2965–2974, 1971.

[25] S. Murray, C. Hillman, and M. Pecht, “Environmental Aging and Deadhesion of Polyimide Dielectric Films,” *J. Electron. Packag.*, vol. 126, no. 3, p. 390, 2004.

[26] B. D. Harper, J. M. Rao, V. H. Kenner, and C. H. Popelar, “Hygrothermal Effects upon Stress-Relaxation in a Polyimide Film,” *J. Electron. mater.*, vol. 26, no. 7, pp. 798–804, 1997.

[27] G. Meyer, C. Perrot, G. Gebel, L. Gonon, S. Morlat, and J.-L. Gardette, “Ex situ hydrolytic degradation of sulfonated polyimide membranes for fuel cells,” *Polymer (Guildf).*, vol. 47, no. 14, pp. 5003–5011, 2006.

[28] D. R. Askins, “Hydrolytic degradation of kapton film,” *J. Plast. Film Sheeting*, vol. 1, no. 1, pp. 50–59, 1985.

[29] E. E. Shin, R. J. Morgan, and J. Zhou, “Hydrolytic degradation mechanisms and kinetics of polyimides for advanced composites,” *Int. SAMPE Symp. Exhib.*, vol. 45, p. /, 2000.

[30] R. J. Morgan, E. E. Shin, J. Zhou, and J. Zhou, “High temperature polymer matrix-carbon fiber composites--performance issues and future needs,” *Soc. Adv. Mater. Process Eng. Evol. Revolut. Technol. New Millenium*, vol. 44, pp. 1098–1110, 1999.

[31] J. N. Antonakakis, P. Bhargava, K. C. Chuang, and A. T. Zehnder, “Linear viscoelastic properties of HFPE-II-52 polyimide,” *J. Appl. Polym. Sci.*, vol. 100, no. 4, pp. 3255–3263, 2006.

[32] Y. Xu and A. T. Zehnder, “Moisture Degradation Effects on the Mechanical Properties of HFPE-II-52 Polyimide: Experiments and Modeling,” *Exp. Mech.*, vol. (in press), 2017. DOI: 10.1007/s11340-017-0281-3

[33] A. D. Adamczak, A. A. Spriggs, D. M. Fitch, C. Burke, E. E. Shin, and J. C. Grunlan, “Blistering in carbon-fiber-filled fluorinated polyimide,” *Polym. Compos.*, vol. 32, no. 2, pp. 185–192, 2011.

[34] M. W. Czabaj, A. T. Zehnder, and K. C. Chuang, “Blistering of Moisture Saturated Graphite/Polyimide Composites Due to Rapid Heating,” *J. Compos. Mater.*, vol. 43, no. 2, pp. 153–174, 2008.

[35] M. W. Czabaj, A. T. Zehnder, and C.-Y. Hui, “Delamination of moisture saturated graphite/polyimide composites due to rapid heating,” *Compos. Part B Eng.*, vol. 41, no. 7, pp. 568–577, 2010.

[36] B. P. Rice and C. W. Lee, “Study of blister initiation and growth in a high-temperature polyimide,” *Compos. Real World*, pp. 675–685, 1997.

[37] Y. Xu and A. Zehnder, “Pressure, hydrolytic degradation and plasticization drive high temperature blistering failure in wet polyimides,” Submitted to *Extrem. Mech. Lett.*, 2017.

[38] C. E. Sroog, A. L. Endrey, S. V Abramo, C. E. Berr, W. M. Edwards, and K. L. Olivier, “Aromatic polypyromellitimides from aromatic polyamic acids,” *J. Polym. Sci. Part A*

Gen. Pap., vol. 3, no. 4, pp. 1373–1390, 1965.

[39] C. E. Sroog, "Polyimides," *Prog. Polym. Sci.*, vol. 16, no. 4, pp. 561–694, 1991.

[40] K. C. Chuang, C. L. Bowman, T. K. Tsotsis, and C. P. Arendt, "6F-polyimides with phenylethynyl endcap for 315-370 C applications," *High Perform. Polym.*, vol. 15, no. 4, pp. 459–472, 2003.

[41] E. Ripberger, G. P. Tandon, and G. A. Schoeppner, "Characterizing oxidative layer development in AFR-PE-4 resin," in *Proc. of SAMPE 2004 Symp./Exhibition*, 2004.

[42] R. A. Schapery, "On the characterization of nonlinear viscoelastic materials," *Polym. Eng. Sci.*, vol. 9, no. 4, pp. 295–310, 1969.

[43] H. F. Brinson and L. C. Brinson, *Polymer engineering science and viscoelasticity: an introduction*. Springer Science & Business Media, 2007.

[44] C. M. Falcone and M. B. Ruggles-Wrenn, "Rate dependence and short-term creep behavior of a thermoset polymer at elevated temperature," *J. Press. Vessel Technol.*, vol. 131, no. 1, p. 11403, 2009.

[45] A. Wineman, "Nonlinear Viscoelastic Solids--A Review," *Math. Mech. Solids*, vol. 14, no. 3, pp. 300–366, 2009.

[46] C. S. Drapaca, S. Sivaloganathan, and G. Tenti, "Nonlinear Constitutive Laws in Viscoelasticity," *Math. Mech. Solids*, vol. 12, no. 5, pp. 475–501, 2007.

[47] M. C. Boyce, D. M. Parks, and A. S. Argon, "Large inelastic deformation of glassy polymers. Part I: rate dependent constitutive model," *Mech. Mater.*, vol. 7, no. 1, pp. 15–33, 1988.

[48] O. A. Hasan and M. C. Boyce, "A constitutive model for the nonlinear viscoelastic viscoplastic behavior of glassy polymers," *Polym. Eng. Sci.*, vol. 35, no. 4, pp. 331–344, 1995.

[49] G. J. Frank and R. A. Brockman, "A viscoelastic–viscoplastic constitutive model for glassy polymers," *Int. J. Solids Struct.*, vol. 38, no. 30, pp. 5149–5164, 2001.

[50] O. U. Colak, "Modeling deformation behavior of polymers with viscoplasticity theory based on overstress," *Int. J. Plast.*, vol. 21, no. 1, pp. 145–160, 2005.

[51] E. Ghorbel, "A viscoplastic constitutive model for polymeric materials," *Int. J. Plast.*, vol. 24, no. 11, pp. 2032–2058, 2008.

[52] L. Anand, N. M. Ames, V. Srivastava, and S. A. Chester, "A thermo-mechanically coupled theory for large deformations of amorphous polymers. Part I: Formulation," *Int. J.*

Plast., vol. 25, no. 8, pp. 1474–1494, 2009.

[53] N. M. Ames, V. Srivastava, S. A. Chester, and L. Anand, "A thermo-mechanically coupled theory for large deformations of amorphous polymers. Part II: Applications," *Int. J. Plast.*, vol. 25, no. 8, pp. 1495–1539, 2009.

[54] A. J. W. McClung and M. B. Ruggles-Wrenn, "Strain rate dependence and short-term relaxation behavior of a thermoset polymer at elevated temperature: experiment and modeling," *J. Press. Vessel Technol.*, vol. 131, no. 3, p. 31405, 2009.

[55] A. C. Pipkin, *Lectures on viscoelasticity theory*. Springer, 1986.

[56] L. Anand and M. E. Gurtin, "A theory of amorphous solids undergoing large deformations, with application to polymeric glasses," *Int. J. Solids Struct.*, vol. 40, no. 6, pp. 1465–1487, 2003.

[57] M. A. Branch, T. F. Coleman, and Y. Li, "A subspace, interior, and conjugate gradient method for large-scale bound-constrained minimization problems," *SIAM J. Sci. Comput.*, vol. 21, no. 1, pp. 1–23, 1999.

[58] R. D. Bradshaw and L. C. Brinson, "A sign control method for fitting and interconverting material functions for linearly viscoelastic solids," *Mech. Time-Dependent Mater.*, vol. 1, no. 1, pp. 85–108, 1997.

[59] J. C. Lagarias, J. A. Reeds, M. H. Wright, and P. E. Wright, "Convergence properties of the Nelder--Mead simplex method in low dimensions," *SIAM J. Optim.*, vol. 9, no. 1, pp. 112–147, 1998.

[60] J. A. Nelder and R. Mead, "A simplex method for function minimization," *Comput. J.*, vol. 7, no. 4, pp. 308–313, 1965.

[61] C. T. Sun and R. S. Vaidya, "Prediction of composite properties from a representative volume element," *Compos. Sci. Technol.*, vol. 56, no. 2, pp. 171–179, 1996.

[62] M. R. Nedele and M. R. Wisnom, "Finite element micromechanical modelling of a unidirectional composite subjected to axial shear loading," *Composites*, vol. 25, no. 4, pp. 263–272, 1994.

[63] P. Rupnowski, M. Gentz, J. K. Sutter, and M. Kumosa, "Mechanical response of a woven graphite/polyimide composite to in-plane shear dominated loads at room and elevated temperatures," *Acta Mater.*, vol. 52, no. 19, pp. 5603–5613, 2004.

[64] P. Bhargava and A. T. Zehnder, "High temperature shear strength of T650-35/HFPE-II-52 polyimide matrix unidirectional composite," *Exp. Mech.*, vol. 46, no. 2, pp. 245–255, 2006.

[65] K. V Pochiraju, G. Tandon, and G. A. Schoeppner, *Long-term durability of polymeric matrix composites*. Springer Science & Business Media, 2011.

[66] B. P. Rice, "Hygrothermal studies on fluorinated polyimides - a physical characterization," in *Proceedings of the 1996 28th International SAMPE Technical Conference, November 4, 1996 - November 7*, 1996, vol. 28, pp. 778–789.

[67] R. J. Morgan *et al.*, "Durability characterization of bismaleimide and polyimide-carbon fiber composites," *Mater. Process affordability- Keys to Futur.*, pp. 106–119, 1998.

[68] T. Shimokawa, Y. Hamaguchi, and H. Katoh, "Effect of Moisture Absorption on Hot/Wet Compressive Strength of T800HIPMR-15 Carbon/Polyimide," *J. Compos. Mater.*, vol. 33, no. 18, pp. 1685–1698, 1999.

[69] L. J. Burcham, M. R. Vanlandingham, R. F. Eduljee, and J. W. Gillespie, "Moisture effects on the behavior of graphite/polyimide composites," *Polym. Compos.*, vol. 17, no. 5, pp. 682–690, 1996.

[70] P. Bhargava, K. C. Chuang, K. Chen, and A. Zehnder, "Moisture diffusion properties of HFPE-II-52 polyimide," *J. Appl. Polym. Sci.*, vol. 102, no. 4, pp. 3471–3479, 2006.

[71] V. Muralidharan and C.-Y. Hui, "Steam pressure generated in a spherical cavity in a moisture saturated polymer matrix composite during rapid heating," *J. Eng. Mater. Technol.*, vol. 128, no. 1, pp. 50–54, 2006.

[72] V. Muralidharan, C.-Y. Hui, V. R. Krishnan, and K. D. Papoulia, "A flow through porous media model for pore pressure during heating of polymer–matrix composites," *Compos. Sci. Technol.*, vol. 66, no. 10, pp. 1409–1417, 2006.

[73] C.-Y. Hui, V. Muralidharan, and M. O. Thompson, "Steam pressure induced in crack-like cavities in moisture saturated polymer matrix composites during rapid heating," *Int. J. Solids Struct.*, vol. 42, no. 3, pp. 1055–1072, 2005.

[74] V. Muralidharan and C.-Y. Hui, "Effect of heating rate on steam pressure induced in crack-like cavities in moisture saturated polymer matrix composites," *Int. J. Solids Struct.*, vol. 43, no. 20, pp. 6085–6099, 2006.

[75] R. F. Gibson, *Principles of Composite Material Mechanics*, no. 205. McGraw-Hill, Inc., 1994.